Title
Energy-Resolved Probing and Rectification Spectroscopy of Single Molecules

Author
Chen, Siyu

Publication Date
2022

Peer reviewed|Thesis/dissertation

UNIVERSITY OF CALIFORNIA,
IRVINE

Energy-Resolved Probing and Rectification Spectroscopy of Single Molecules

DISSERTATION

submitted in partial satisfaction of the requirements
for the degree of

DOCTOR OF PHILOSOPHY

in Physics

by

Siyu Chen

Dissertation Committee:
Professor Wilson Ho, Chair
Professor Ilya Krivorotov
Professor Ruqian Wu

2022

DEDICATION

To

My Family

TABLE OF CONTENTS

LIST OF FIGURES

ACKNOWLEDGEMENTS

First, I would like to express my sincere gratitude to my thesis advisor and committee chair, Professor Wilson Ho, for his guidance and support in my 7-year-long PhD life. He has inspired me with his dedication to scientific research and consistent hard-working attitude. Besides, he provided a supportive environment for problem solving and creative thinking, which greatly encouraged me to make adaptions to instrumentation designs for better performance. His high standards for quality and integrity in both lab work and research have made a great example for me to follow in my future careers.

I would also like to thank Professor Ilya Krivorotov and Professor Ruqian Wu for serving both my advancement and dissertation defense committees. I appreciate the valuable discussions and advice from them. DFT calculations done by Professor Wu's group have been very helpful in helping me gain deeper insights on my research subject.

Special thanks to Wenlu Shi and Jiang Yao, who have run experiments with me. Wenlu has worked with me on every project presented in this dissertation and we had lots of fun troubleshooting and renovating the STM IV system. His strong sense of ownership and management skills have impressed and inspired me a lot. Jiang Yao, as a good husband and co-worker, has provided me tremendous support throughout my PhD career. His passion for research and engineering has brought this lab a great amount of innovations in instrumentation and experimental techniques. Many control electronics used in my experiments were designed and built by Jiang. I am happy to have collaborated with him on our last two experiments.

I am grateful for all other lab members that I have worked with. Dr. Shaowei Li was my mentor during the first two years and has taught me important lab skills and set up a great example as a successful PhD student. Likun Wang and I collaborated on the early-stage THz-STM project in

STM II and I’m impressed by his perseverance and dedication to his research project. Yunpeng Xia has been a sharp mind to our lab and I appreciate his educational spirit in sharing frontier sciences to the lab members. As new bloods to this lab, Dan bai and Jiawei Zeng have both shown great potentials and strong dedication in pursuing this adventurous path. I wish them the best luck with their PhD career.

Lastly, I would also like to thank Office of Naval Research under Grant No. N00014-20-1-2475, and Eddleman Quantum Institute Fellowship for the funding supports in carrying out my research projects.

VITA

Siyu Chen

4129 Frederick Reines Hall, University of California, Irvine, CA, 92697

(949)232-2016 | chens13@uci.edu

Education

6.2015 -6.2022, Ph.D. in Physics (Chemical and Material Physics)

- University of California, Irvine, USA
- Thesis Advisor: Professor Wilson Ho
- GPA:3.907 (out of 4)

9.2011-6.2015, BSc in Physics (Optics track)

- Nankai University, China
- GPA:89.81 (out of 100)

Experience

9.2015– 6.2022

Graduate Student Researcher, UC Irvine, Department of physics and Astronomy

Research projects on single molecule chemistry studied with an 8K-Optical Scanning tunneling microscope:

- Frequency domain study of overtone-assisted isomerization of single Pyrrolidine molecules.
- CW-THz rectification spectroscopy for single molecules of various type.
- Frequency domain spectroscopy (FDS) in few-THz range, for both ambient environment and single molecule at STM junction.
- Optical rectification line shape study of single pyrrolidine molecules.

Electronics/hardware projects:

- Rebuilt multiple UHV instruments for home-made STM system, including the ion source, sample heater, ion gauge, etc.
- Rebuilt a STM scanner assembly, including wiring and vibrational damping structure for superior performance in UHV and low temperature condition.
- Troubleshooting and test of electronics, including both digital and analog circuits.

Instrumental and mechanical design using CAD software (Autodesk Inventor):

- Compact portable multi-functional vacuum pump station.
- UHV (Ultra High Vacuum) compatible wobble stick pincer head with improved performance.
- Multi-axis vacuum-compatible optical assembly for coupling NIR and THz to UHV STM junction.
- UHV Molecular load-lock system with compact linear translator.
- Precision part design of accessories to existing instrument assembly.

Developed LabVIEW programs for lab-level applications:

- Automatic sample annealing with PID temperature regulation
- Automatic data acquisition, instrumental control, and data processing for experiments.
- Automatic PCB board testing (DAC board, ADC board, etc.)

10.2015 – 6.2017

Teaching Assistant, UC Irvine, Department of physics and Astronomy

- Lead discussion and lab sessions for classic physics courses including Mechanics, Kinematics, Electromagnetics, Optics. Created quiz problems for discussions.
- Lead advanced physics labs and assisted in instrument troubleshooting.

Skills

Software and tools: Autodesk Inventor, NI LabVIEW (CLAD certified), Microsoft Office suite, MATLAB, Origin Lab, RStudio, Mathematica, Adobe Illustrator, AutoCAD.
Programming language: Python, R, MATLAB.
Laboratory skills:

- Scanning Tunneling Microscopy (STM).
- UHV (Ultra High Vacuum) and cryogenics-related instrument operation.
- Tools including digital multimeter, oscilloscope, function generator, Lock-in amplifier, etc.
- Ultrafast laser operation and general optics, including optical path design, free-space alignment, and beam characterization.
- Surface treatment technique such as electrochemical-plating and electrochemical-etching.

Other skills:

- Machining using milling tree and lathe.
- Knowledge of analog and digital circuits for instrument control and communication.

- Industrial techniques such SEM imaging, E-beam deposition, sputter coating, E-beam Lithography, optical lithography, UHV-CVD, PVD.
- Statistical analysis including multiple variable linear regression, ANOVA, A/B testing.

Organization and Activities

3.2022 APS March Meeting:

- CW THz rectification spectroscopy of single molecules in STM tunneling junction

8.2020 – 6.2022: EQI (Eddleman Quantum Institute) Graduate Council Member:

- Invited talk at William Evans group meeting on STM research (9.2020).
- Collaborated with other research groups on instrument leaks detection.

3.2018 APS March Meeting:

- Single Molecule Dynamics with Joint Angstrom-Femtosecond Resolution

9.2017- 6.2019: CaSTL Center (Chemistry at the Space-Time Limit) scholar:

- Organized multiple outreach lab tours for middle school scholars.
- Served as volunteer in multiple scientific outreach events.
- Gave report talk at CASTL seminar (5.2019).

Reward/Certificate

12.2021 -12.2023: Certified Associate LabVIEW Developer (National Instrument)
6.2015: Outstanding graduate of Nankai University

Publication

1. **Siyu Chen**, Wenlu Shi, Wilson Ho, In preparation, (2022).
2. Shaowei Li, Gregory Czap, Hui Wang, Likun Wang, **Siyu Chen**, Arthur Yu and Ruqian Wu, Phys. Rev. Lett., 112, 077401 (2019).
3. Arthur Yu, Shaowei Li, Hui Wang, **Siyu Chen**, and Ruqian Wu, Nano Lett., 18, 5 3076-3080 (2018).
4. Shaowei Li, **Siyu Chen**, Jie Li, and Ruqian Wu, Phys. Rev. Lett., 119, 176002 (2017).

ABSTRACT OF THE DISSERTATION

Energy-Resolved Probing and Rectification Spectroscopy of Single Molecules

by

Siyu Chen
Doctor of Philosophy in Physics
University of California, Irvine, 2022
Professor Wilson Ho, Chair

The main goal of the studies presented in this dissertation is to continue the endeavor in improving of energy-probing capability of STM for single molecule spectroscopy. Here, we extend energy spectrum into THz region for STM vibrational spectroscopy by combining an 8-Kelvin scanning tunneling STM with a continuous wave THz source. Development of THz rectification technique allowed probing of vibrational excitations with simultaneous chemical sensitivity, THz field sensitivity and <10 MHz energy resolution.

On the other hand, by incorporating tunable NIR lasers into an STM junction, we demonstrate the energy-resolved probing of vibrational overtone resonant excitation through the vibration-mediated conformational transition of single pyrrolidine molecules. Photon equilibrium action spectroscopy was performed to observe wavelength dependent resonance excitation features with sub-meV energy resolution. These features were shown to be sensitive to the molecular local adsorption environment while being insensitive to the junction near field profile induced by junction plasmon excitation or the optical setup.

Moreover, the light induced equilibrium change in the reversible conformational transition of pyrrolidine leads to generation of photocurrent. Using optical rectification spectroscopy, we investigated the influence of laser power and tunneling setpoint on the photocurrent. The photocurrent was shown to be governed by the competition between photon and electron contribution to the molecular reversible transition, which can be tuned through laser power, bias and tip-molecular interaction. Through the optical rectification study of pyrrolidine, we demonstrate its potential application as a tunable single-molecule photo-rectifier device when trapped between two electrodes.

Chapter 1

Introduction

1.1 Background

Scanning tunneling microscopy (STM) is a Nobel-winning technique first developed by Binnig and Rohrer in 1981 [1,2]. Since its invention, it has been widely used for imaging surfaces and molecular clusters at the atomic level. Combined with STM, inelastic tunneling spectroscopy (IETS) became one of the most used techniques for studying the vibrational and electronic excitations of surfaces and molecular adsorbates with atomic scale spatial resolution and strong chemical sensitivity [3–10].

While the sub-angstrom spatial resolution relies on the spatially confined tunneling current between the probe tip and surface, the energy resolution of STM is mostly determined by the tunneling electrons. However, due to thermal broadening and modulation broadening [11], IETS cannot achieve good sub-meV energy resolution and cannot probe energy modes in the sub-meV range. Therefore, there are two directions in which researchers have put their efforts in: one is to expand the probing range into the sub-meV region by coupling a radio frequency or THz source into a tunneling junction; the other is to enhance the probing energy resolution in general by combining STM with different types of optical spectroscopy techniques. This thesis presents the studies as efforts in both directions by demonstrating CW THz Rectification Spectroscopy and laser action spectroscopy performed at single molecule levels.

1.2 Motivation for CW THz Rectification Spectroscopy

STM electron spin resonance (STM-ESR) was developed to study spin excitation and exchange interactions of atomic spin centers, with the assistance of a spin-polarized probe tip and RF radiation coupled to an STM junction [12–18]. Although this has largely expanded the energy probing capability of STM into the RF range, there's still a small gap in the energy spectrum not covered by either electron or RF radiation, which is referred to as the "THz gap" [19]. This leads to efforts in closing the energy gap by introducing THz radiation to an STM junction.

The early-stage advances in THz-STM are mostly focused on ultrafast THz-STM. The first ultrafast THz-STM work was reported by Cocker et al. in 2013 [20] demonstrating ultrafast pump-probe measurement using the transient voltage induced by THz pulses at a tunneling junction. Then there follows many other ultrafast THz-STM studies, mostly with an emphasis on the characterization and carrier envelope phase control of THz-induced transient nearfield and their application as an ultrafast probing voltage source [21–36]. However, less attention is paid to the photon characteristics of THz radiation and its resonance probing of single molecules. A recent study by Wang et al. has reported the coherence excitation in hydrogen molecules trapped in a tunneling junction, through time domain spectroscopy (TDS) using ultrafast THz pulses [37]. This study demonstrated the feasibility of THz-induced resonant excitation at tunneling junction. It is therefore desired to combine a CW THz source to the tunneling junction for direct frequency domain spectroscopy (FDS), which can provide much higher energy resolution without having to obtain large delay time range measurement in TDS. CW THz Rectification measurement is introduced in this thesis to provide an alternative to IETS with good chemical sensitivity while being sensitive to THz field, which can be potentially used for FDS measurement in hydrogen molecules and other systems with low energy vibrational/spin excitation modes in the THz range.

1.3 Electron Action Spectroscopy and Laser Action Spectroscopy

Probing and controlling of chemical reaction at atomic level has been a very popular research topic in the field of chemistry, due to its importance in understanding and controlling the chemical reactions at macroscopic level. Action spectroscopy has been widely used to study single molecule reactions on metal substrates[38,39]. The term action spectroscopy commonly refer to electron action spectroscopy, where inelastic tunneling electrons can assist chemical reaction in a single molecule through excitation of molecular vibrations and their overtones and combinational modes through inelastic scattering, such as bond dissociation and rotation in O_2 on Pt(111) substrate [40,41], desorption of NH_3 from Cu(100) substrate [42] , and CO hopping on Ag(110) substrate [43]. Under the presence of an electronic state, reactions can also be induced through charge injection that forms a transient negative ion (TNI) state, which then relaxes into vibrationally excited states, leading to the actual reaction [44].

With electron action spectroscopy alone, we still lack high energy resolution due to the thermal broadening in electron energy as well as the non-resonance nature of inelastic tunneling process. Therefore, borrowing the same idea, people have also developed laser action spectroscopy, where reaction rate is measured as a function of photon energy. A common measurement performed in laser action spectroscopy is photon yield, which describes the contribution to reaction per photon. However, due to the surface plasmon excitation at junction, the photon yield is usually a combined result of junction nearfield intensity and molecular electronic structure, therefore the spectra obtained often cannot reflects pure photon-energy dependence regarding the molecular electronic/ vibrational excitation [45–47]. In the context of a photo-induced reversible reaction, the photon-induced reaction equilibrium in fact reflects the photon contribution to a reaction kinetics with less influence from junction nearfield. In this thesis we demonstrate the example of laser action

spectroscopy for a pyrrolidine molecule by comparing both photon yield and photon equilibrium measurement in its reversible conformational transition process. And through the measurement of photocurrent generated from a pyrrolidine molecule, we further demonstrate the potential application of a single molecule optical transistor and photo-mixer with such photo-switching systems and the possibility of tuning photocurrent with different parameters.

1.4 Chapter Summary

This dissertation summarizes my PhD work in instrumental and methodology development of energy-resolved probing and rectification spectroscopy using a low-temperature STM coupled to a CW THz source or tunable optical lasers.

Chapter 2 introduces the method of CW THz rectification spectroscopy. THz rectification spectra of various molecules are obtained and compared to traditional IETS measurement. Rectification spectra were obtained with different THz field strength to investigate the effect of THz field on spectra line shape and signal intensity.

Chapter 3 discusses the energy-resolved detection of overtone assisted isomerization process of a single Pyrrolidine molecule on Cu(001). We investigated the electron and photon contribution respectively in the vibration-mediated conformation transition process. Photon equilibrium action spectroscopy was introduced to probe photoexcitation of vibrational overtones through measurement of photo-induced reaction equilibrium shift, which is immune to tunneling electron energy and power variation among different wavelengths due to localized surface plasmons, optical interference and alignment inconsistency.

Chapter 4 demonstrates the measurement of photocurrent from a single Pyrrolidine molecule through optical rectification spectroscopy with a 1550nm laser. We introduce the different

mechanism for tuning of photocurrent for this molecule and investigate how electron and photon play different roles in this process. The optical rectification spectra measured under different laser power and tunneling setpoint was examined and simulated to assist deeper understanding of the nature of optical rectification signal from pyrrolidine.

The appendices include more detailed information on the instrumental designs, technical difficulties and solutions, manuals, etc. MATLAB scripts for data fitting to obtain THz field calibration at STM junction and python scripts for optical rectification simulation are also included.

Bibliography

[1] G. Binnig, H. Rohrer, Ch. Gerber, and E. Weibel, Applied Physics Letters, **40**, 178–180 (1982).

[2] G. Binnig, H. Rohrer, Ch. Gerber, and E. Weibel, Physical Review Letters, **49**, 57–61 (1982).

[3] B.C. Stipe, M.A. Rezaei, and W. Ho, Physical Review Letters, **82**, 1724–1727 (1999).

[4] N. Lorente, M. Persson, L.J. Lauhon, and W. Ho, Physical Review Letters, **86**, 2593–2596 (2001).

[5] J. Gaudioso, L.J. Lauhon, and W. Ho, Physical Review Letters, **85**, 1918–1921 (2000).

[6] B.C. Stipe, M.A. Rezaei, and W. Ho,Science, **280**, 1732–1735 (1998).

[7] B.C. Stipe, M.A. Rezaei, and W. Ho, Review of Scientific Instruments, **70**, 137–143 (1999).

[8] B.C. Stipe, M.A. Rezaei, and W. Ho, Physical Review Letters, **82**, 1724–1727 (1999).

[9] L.J. Lauhon and W. Ho, Surface Science, **451**, 219–225 (2000).

[10] G. Czap, Z. Han, P.J. Wagner, and W. Ho, Physical Review Letters, **122**, 1–5 (2019).

[11] J. Klein, A. Léger, M. Belin, D. Défourneau, and M.J.L. Sangster, Physical Review B, **7**, 2336–2348 (1973).

[12] W. Paul, S. Baumann, C.P. Lutz, and A.J. Heinrich, Review of Scientific Instruments, **87**, 074703 (2016).

[13] S. Müllegger, S. Tebi, A.K. Das, W. Schöfberger, F. Faschinger, and R. Koch, Physical Review Letters, **113**, 1–5 (2014).

[14] S. Baumann, W. Paul, T. Choi, C.P. Lutz, A. Ardavan, and A.J. Heinrich,Science, **350**, 417–420 (2015).

[15] J.L. Lado, A. Ferrón, and J. Fernández-Rossier, Physical Review B, **96**, 1–6 (2017).

[16] F.D. Natterer, K. Yang, W. Paul, P. Willke, T. Choi, T. Greber, A.J. Heinrich, and C.P. Lutz, Nature, **543**, 226–228 (2017).

[17] K. Yang, P. Willke, Y. Bae, A. Ferrón, J.L. Lado, A. Ardavan, J. Fernández-Rossier, A.J. Heinrich, and C.P. Lutz, Nature Nanotechnology, **13**, 1120–1125 (2018).

[18] T. Choi, W. Paul, S. Rolf-Pissarczyk, A.J. MacDonald, F.D. Natterer, K. Yang, P. Willke, C.P. Lutz, and A.J. Heinrich, Nature Nanotechnology, **12**, 420–424 (2017).

[19] K. Yang, W. Paul, F.D. Natterer, J.L. Lado, Y. Bae, P. Willke, T. Choi, A. Ferrón, J. Fernández-Rossier, A.J. Heinrich, and C.P. Lutz, Physical Review Letters, **122**, 227203 (2019).

[20] T.L. Cocker, V. Jelic, M. Gupta, S.J. Molesky, J.A.J. Burgess, G.D.L. Reyes, L. v. Titova, Y.Y. Tsui, M.R. Freeman, and F.A. Hegmann, Nature Photonics, **7**, 620–625 (2013).

[21] M. Eisele, T.L. Cocker, M.A. Huber, M. Plankl, L. Viti, D. Ercolani, L. Sorba, M.S. Vitiello, and R. Huber, Nature Photonics, **8**, 841–845 (2014).

[22] H. Shigekawa, S. Yoshida, and O. Takeuchi, Nature Photonics, **8**, 815–817 (2014).

[23] L. Wimmer, G. Herink, D.R. Solli, S. v. Yalunin, K.E. Echternkamp, and C. Ropers, Nature Physics, **10**, 432–436 (2014).

[24] Y. Luo, V. Jelic, G. Chen, P.H. Nguyen, Y.J.R. Liu, J.A.M. Calzada, D.J. Mildenberger, and F.A. Hegmann, Physical Review B, **102**, 205417 (2020).

[25] V. Jelic, K. Iwaszczuk, P.H. Nguyen, C. Rathje, G.J. Hornig, H.M. Sharum, J.R. Hoffman, M.R. Freeman, and F.A. Hegmann, Nature Physics, **13**, 591–597 (2017).

[26] S. Yoshida, Y. Arashida, H. Hirori, T. Tachizaki, A. Taninaka, H. Ueno, O. Takeuchi, and H. Shigekawa, ACS Photonics, **8**, 315–323 (2021).

[27] K. Kimura, Y. Morinaga, H. Imada, I. Katayama, K. Asakawa, K. Yoshioka, Y. Kim, and J. Takeda, ACS Photonics, **8**, 982–987 (2021).

[28] T.L. Cocker, V. Jelic, R. Hillenbrand, and F.A. Hegmann, Nature Photonics, **15**, 558–569 (2021).

[29] S. Yoshida, H. Hirori, T. Tachizaki, K. Yoshioka, Y. Arashida, Z.H. Wang, Y. Sanari, O. Takeuchi, Y. Kanemitsu, and H. Shigekawa, ACS Photonics, **6**, 1356–1364 (2019).

[30] T.L. Cocker, D. Peller, P. Yu, J. Repp, and R. Huber, Nature, **539**, 263–267 (2016).

[31] P.H. Nguyen, C. Rathje, G.J. Hornig, V. Jelic, C. Ropers, and F.A. Hegmann, Physics in Canada, **71**, 157–160 (2015).

[32] T. Tachizaki, K. Hayashi, Y. Kanemitsu, and H. Hirori, APL Materials, **9**, 060903 (2021).

[33] K. Yoshioka, I. Katayama, Y. Arashida, A. Ban, Y. Kawada, K. Konishi, H. Takahashi, and J. Takeda, Nano Letters, **18**, 5198–5204 (2018).

[34] K. Yoshioka, I. Katayama, Y. Minami, M. Kitajima, S. Yoshida, H. Shigekawa, and J. Takeda, Nature Photonics, **10**, 762–765 (2016).

[35] K. Moon, H. Park, J. Kim, Y. Do, S. Lee, G. Lee, H. Kang, and H. Han, Nano Letters, **15**, 549–552 (2015).

[36] M. Abdo, S. Sheng, S. Rolf-Pissarczyk, L. Arnhold, J.A.J. Burgess, M. Isobe, L. Malavolti, and S. Loth, ACS Photonics, **8**, 702–708 (2021).

[37] W. Likun, X. Yunpeng, and H. W., Science, **376**, 401–405 (2022).

[38] Y. Kim, K. Motobayashi, T. Frederiksen, H. Ueba, and M. Kawai, Progress in Surface Science, **90**, 85–143 (2015).

[39] K. Motobayashi, Y. Kim, H. Ueba, and M. Kawai, Physical Review Letters, **105**, 076101 (2010).

[40] B.C. Stipe, M. a. Rezaei, and W. Ho, Journal of Chemical Physics, **107**, 6443–6447 (1997).

[41] B.C. Stipe, M.A. Rezaei, and W. Ho, Science, **279**, 1907–1909 (1998).

[42] J.I. Pascual, N. Lorente, Z. Song, H. Conrad, and H.P. Rust, Nature, **423**, 525–528 (2003).

[43] J. Oh, H. Lim, R. Arafune, J. Jung, M. Kawai, and Y. Kim, Physical Review Letters, **116**, 56101 (2016).

[44] L.J. Lauhon and W. Ho, Physical Review Letters, **84**, 1527–1530 (2000).

[45] E. Kazuma, J. Jung, H. Ueba, M. Trenary, and Y. Kim, Science, **360**, 521–526 (2018).

[46] E. Kazuma, M. Lee, J. Jung, M. Trenary, and Y. Kim, Angewandte Chemie - International Edition, **59**, 7960–7966 (2020).

[47] K.G. Nakamura, K. Ohya, H. Takahashi, T. Tsuruta, H. Sasaki, S.I. Uozumi, K. Norimatsu, M. Kitajima, Y. Shikano, and Y. Kayanuma, Physical Review B, **94**, 144304 (2016).

Chapter 2

Single-Molecule CW THz Rectification Spectroscopy[†]

2.1 Abstract

We report rectification spectra (RS) of single molecules in a scanning tunneling microscope (STM) junction with continuous-wave terahertz (CW THz) radiation at the tip-substrate junction of an 8K-STM. The THz RS over a single molecule exhibit line shapes closely related to those obtained by the inelastic electron tunneling spectroscopy (IETS) and therefore serves as an alternative technique in single-molecule vibrational spectroscopy. By quantitatively studying THz RS peak broadening and IETS peak splitting obtained with different THz radiation intensities, we show that THz induced voltage can be viewed as a sinusoidal wave bias modulation with an amplitude linearly dependent on the THz far field amplitude but insensitive to tunnelling gap when the gap is far smaller than the THz wavelength.

[†] This chapter by Siyu Chen, Wenlu Shi and Wilson Ho is prepared for submission.

2.2 Article

Rectifiers such as semiconductor diodes and vacuum tube diodes are widely used in power electronics for signal conversion from AC into DC. The essential property that leads to signal rectification is the nonlinear response of a device. In the context of a single molecule at a tunneling junction, inelastic tunneling induced nonlinearity in I(V) curve give rise to rectification current under an AC bias modulation. Atomic-scale rectification was first demonstrated by Tu et al. with microwave induced bias modulation at a tunneling junction for a single Mn atom and a single MnCO molecule [1]. This was later used for detecting magnetic domain of a Chromium substrate [2] and isotope shift in acetylene molecules [3]. The great spin sensitivity and chemical sensitivity demonstrated in microwave rectification measurement suggests an alternative to traditional inelastic electron tunneling spectroscopy (IETS) [4,5] for single molecule spectroscopy.

Recent years, emerging technologies in ultra-fast broadband THz pulse generation [6–9] have facilitated implementation of ultrafast THz pulses as a probing voltage source in STM measurement with atomic spatial resolution [10–17]. THz induced rectification current were used to characterize the THz transient near field at a tip-substrate junction [18,19] and probe the nanoscale ultrafast dynamics [15,20]. However, in these studies, the extreme voltage induced through THz nearfield at junction makes it difficult to perform low-energy vibrational spectroscopy for a single molecule. Until recently, a study by Wang et al. demonstrated that a moderate rectification current induced by THz pulses not only reveals the low-energy vibrational and rotational modes in a hydrogen molecule, but can also be used to probe its coherent excitation with time domain spectroscopy (TDS) [21]. To achieve high frequency resolution through TDS measurement, large range of time delay scan is required, which is often time-consuming. While the frequency domain spectroscopy (FDS) can provide high frequency resolution within a specific

frequency range, it is therefore beneficial to incorporate FDS as a complemental approach for single molecule THz spectroscopy by combining a tunable broadband CW THz source [22–24] with STM. In fact, studies in ambient conditions with bulk materials have shown great feasibility of using a photoconductive antenna (PCA) to generate broadband CW THz and perform frequency domain measurement [24–27].

In this paper, we demonstrate measurement of CW THz rectification measurement from different single molecules using THz radiation generated from a PCA through photo-mixing process. We perform quantitative analysis on its line shape and signal intensity for CW THz rectification spectra (RS) and compare the line shape of THz RS to that of regular IETS to demonstrate the physical connection between the two types of measurements. THz induced peak splitting in IETS measurement were also quantitively studied with different THz far field intensities. Estimated THz induced voltage across tunneling junction was shown to be constant for the tunneling gap range of our measurement. Our study implies the potential application of THz rectification measurement in THz field sensing and frequency domain spectroscopy with atomic spatial resolution.

The experimental setup for CW-THz STM is shown schematically in Figure 2.1a. The continuous-wave THz is generated through optical heterodyning process with an InGaAs PCA emitter (Toptica TeraScan1550). Two tunable DFB diode lasers around 1550nm formed an optical beating at their difference frequency to pump the PCA emitter through optical fiber and drive the THz radiation. The THz beam is collimated by a TPX lens (BaTOP GmbH) and then focused by a Tsurupica lens (Broadband Inc.) into the STM tip-substrate junction at 45-degree

angle from the tip axis. The PCA emitter and lenses are contained in a lens tube assembly and mounted on a 3-axis optical mount and enclosed in a specially designed purge box in air.

The THz radiation intensity is controlled by the voltage applied to the PCA emitter, where THz emission is suppressed at +0.3 V and near saturation at -1.3 V. Chopping of THz beam is implemented by applying a square wave to PCA emitter, the high and low level of which equal +0.3 V and -1.3 V respectively. The low level of PCA voltage is tunable from -1.3 V to +0.3 V, corresponding to strong to weak THz field intensity. For simplicity, we refer to the low-level voltage as PCA voltage (V_{PCA}) for the remaining paragraphs and high level is always fixed at +0.3 V in the case of chopping. Figure 2.1b shows the time traces of the chopping voltage ($V_{Chopping}$) applied to PCA emitter, the THz far field intensity (E_{THz}), and the simulated THz rectification current at STM junction (I_{THz}). With a chopped THz beam focused at the tunneling junction, the THz current is measured by extracting the first-harmonic component from the STM tunneling current using a lock-in amplifier. Recording the rectification current while sweeping sample bias with tip height fixed over a single molecule generates a THz rectification spectrum (RS).

Figure 2.1 Experimental setup and method for CW THz rectification spectroscopy. (a) Schematic diagram of the experimental setup for CW-THz STM. (b) Chopping voltage applied to PCA emitter ($V_{chopping}$), the generated THz field (E_{THz}), and corresponding THz induced rectification current from STM junction (I_{THz}) are shown as a function of time. Both E_{THz} and I_{THz} are simulated and a white noise is added to I_{THz} to simulate high-frequency instrumental noises. The phase differences among the three signals due to electrical and THz transmission are not displayed here for simplicity.

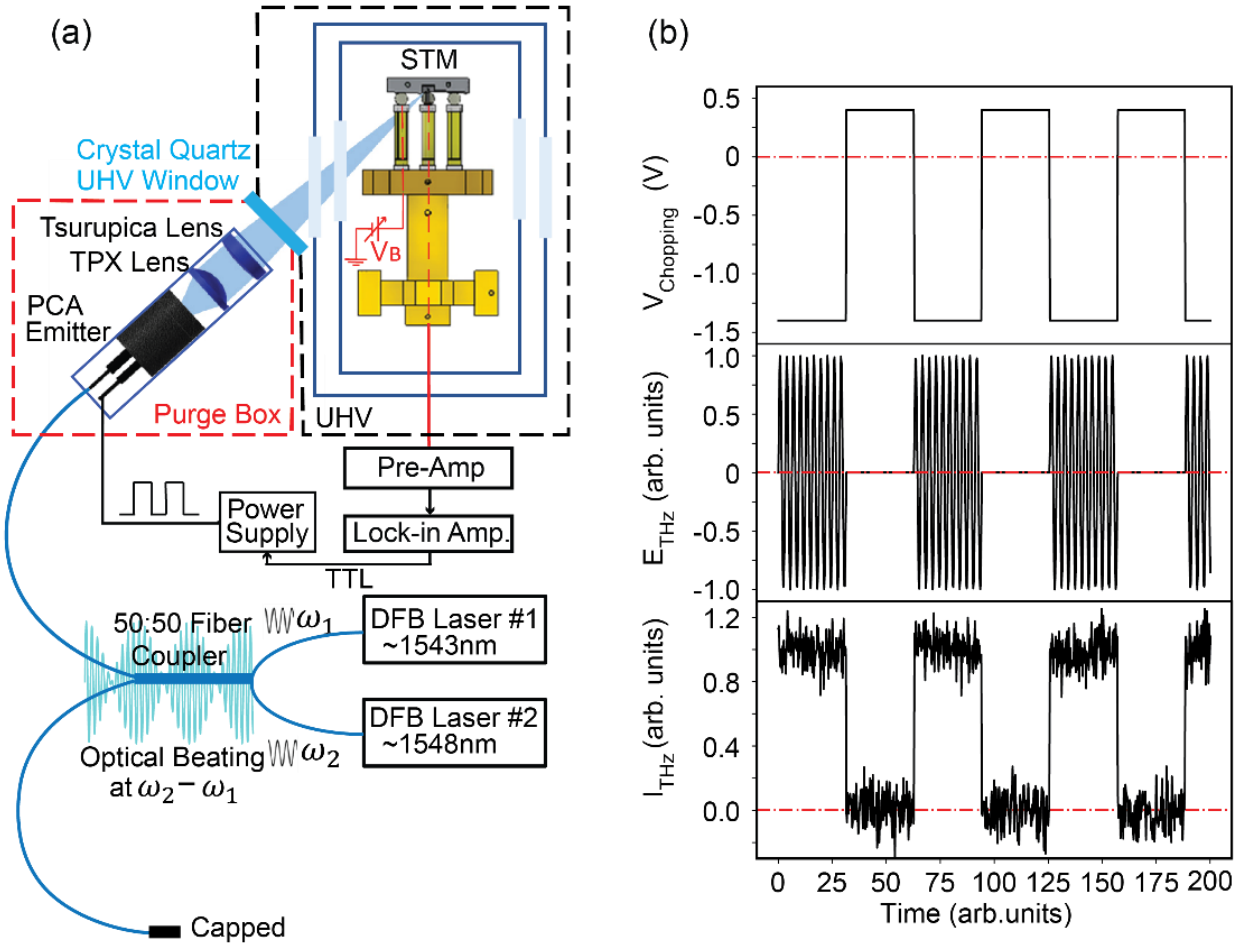
(a)
STM
Crystal Quartz
UHV Window
Tsurupica Lens
TPX Lens
PCA
Emitter
V_B
Purge Box
UHV
Pre-Amp
Power
Supply
Lock-in Amp.
TTL
50:50 Fiber
Coupler
ω_1
DFB Laser #1
~1543nm
DFB Laser #2
~1548nm
Optical Beating
at $\omega_2 - \omega_1$
ω_2
Capped
(b)
$V_{Chopping}$ (V)
E_{THz} (arb. units)
I_{THz} (arb. units)
Time (arb.units)

To demonstrate the chemical sensitivity of THz RS, we measured THz RS for various molecule species and compared them to the corresponding regular IETS obtained at the same set point (Figure 2.2). Measurement conditions used for topography imaging, THz RS, and IETS are listed in Table 2.1.). For carbon monoxide (CO) molecules with different tip-substrate configuration (Figure 2.2a-d), the THz RS (Figure 2.2i-l) obtained at 400GHz exhibit almost identical line shapes and peak positions for CO hindered rotation (HR) and hindered translation (HT) modes as those of the IETS measurements (Figure 2.2q-t). For a nickelocene ($NiCp_2$) adsorbed on Cu(100) substrate (Figure 2.2e), the magnetic anisotropy peak is resolved at $4\ meV$ in the IETS (Figure 2.2u) but blue-shifted to $4.5\ meV$ in the THz RS (Figure 2.2m). This is potentially due to the bigger peak broadening from the THz nearfield induced bias modulation at the tunneling junction compared to the IETS bias modulation. For CO and Nickelocene, the similar line shapes between THz RS and IETS indicate that both measurements reflects the same information on the molecular I(V) curve nonlinearity induced by inelastic tunneling process. However, the line shapes of THz RS sometimes deviate those of the IETS. For pyrrolidine (C_4H_9N) and hydrogen (H_2), we have observed very different line shapes between THz RS and IETS as shown in Figure 2.2n-p and v-x. The major difference lies in the peak shapes, where THz RS shows a symmetric Lorentzian profile while IETS shows an asymmetric Fano profile for all the peaks. By collecting RS using chopped AC bias modulation at frequency from 10kHz to a few MHz, we show that the line shape evolves gradually with increasing modulation frequency from 10kHz to 1MHz and then seems to saturate, while no significant change in line shapes is observed between 10kHz RS and the IETS, and between MHz RS and THz RS (see details in Supporting Information 2.3.4 and Figure 2.7) This result indicates such line shape difference is mostly due to the line shape transition that occurs in mainly in the sub-MHz range, therefore the possibility of THz resonant excitation is

excluded. As pyrrolidine and hydrogen in a tunneling junction both exhibit conductance switching [28,29], the potential energy along their reaction coordinate can be modeled as an asymmetric double well potential. With increasing modulation frequency, the probabilities of switching in two directions are suppressed asymmetrically due to the asymmetry of the double well potential. This leads to a gradual shift in the 2-level population distribution of the molecule, which causes a gradual change in the total conductance of the junction reflected by the rectification current. This process will achieve an equilibrium when modulation far exceeds the switching rates in both directions, which explains the similar line shapes between THz RS and the MHz RS. Despite the modulation frequency response-induced line shape variation, THz RS reflect similar information on vibrational or rotational modes as IETS does, therefore, the chemical sensitivity of THz RS can still be justified.

Figure 2.2 Comparison between THz rectification spectra (RS) and inelastic electron tunneling spectra (IETS) for various molecule species. (a)-(h) Constant-current topography of each probed system. Red stars indicate the tip position for taking spectra. (i)-(p) Corresponding THz RS with THz radiation chopped at 273 Hz (except for (o)(p), where 255.11 Hz chopping is used), and 100 ms lock-in time constant. (q)-(x) Corresponding IETS with the same bias modulation frequency as each THz RS. Measurement conditions used for topography imaging, THz RS, and IETS are listed in Table 2.1.

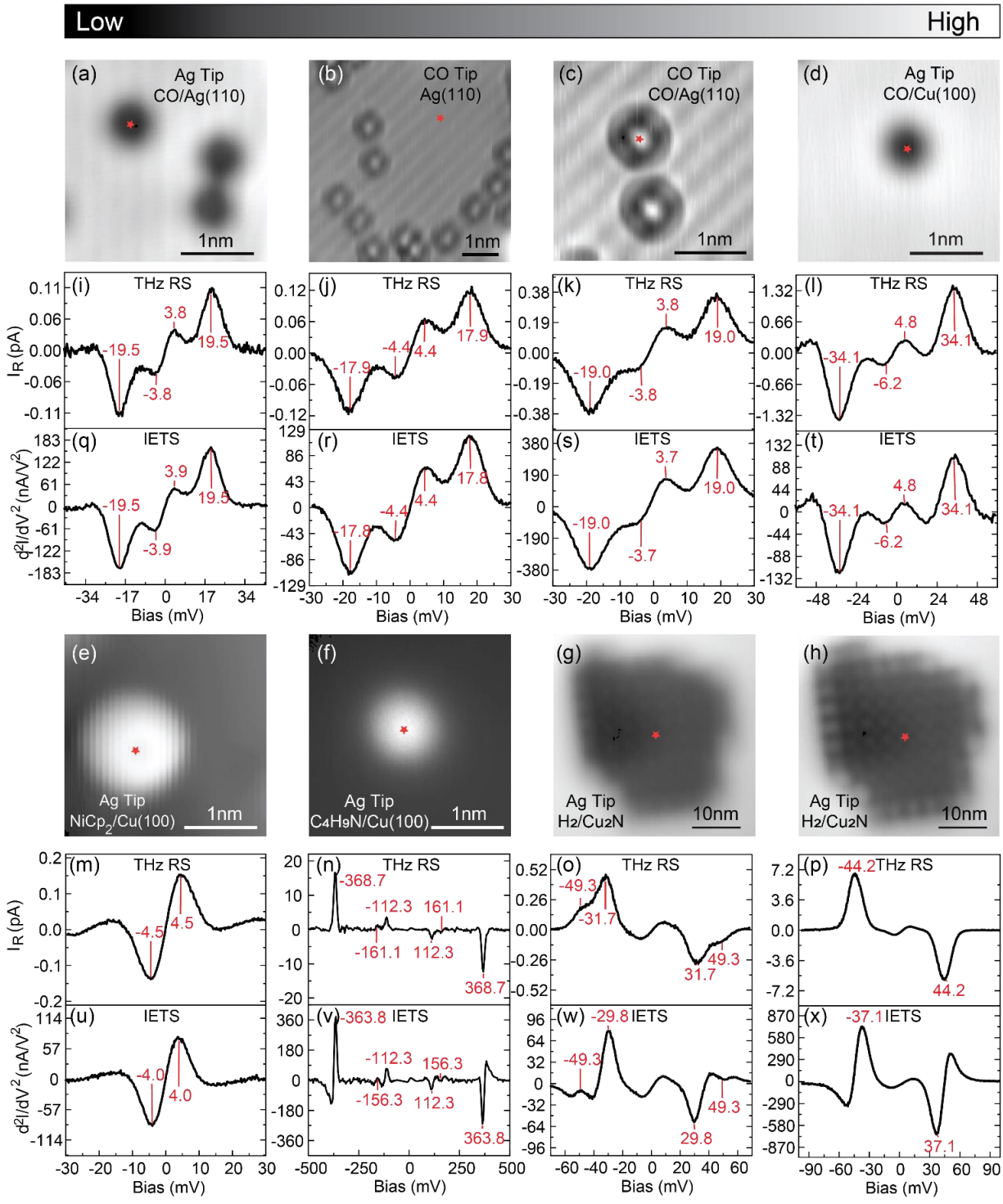
Low
High
(a) Ag Tip CO/Ag(110) 1nm
(b) CO Tip Ag(110) 1nm
(c) CO Tip CO/Ag(110) 1nm
(d) Ag Tip CO/Cu(100) 1nm
(i) THz RS
(j) THz RS
(k) THz RS
(l) THz RS
(q) IETS
(r) IETS
(s) IETS
(t) IETS
I_R (pA)
d²I/dV² (nA/V²)
Bias (mV)
(e) Ag Tip NiCp2/Cu(100) 1nm
(f) Ag Tip C4H9N/Cu(100) 1nm
(g) Ag Tip H2/Cu2N 10nm
(h) Ag Tip H2/Cu2N 10nm
(m) THz RS
(n) THz RS
(o) THz RS
(p) THz RS
(u) IETS
(v) IETS
(w) IETS
(x) IETS

Table 2.1 Measurement conditions used for topography, IETS and THz RS on various molecules in Figure 2.2

Topography in Figure 2.2	(a)	(b)	(c)	(d)	(e)	(f)	(g)	(h)
Setpoint for Topography	40 mV 0.8 nA	10 mV 0.2 nA	10 mV 0.2 nA	-60 mV 0.1 nA	70 mV 40 pA	-500 mV 0.1 nA	-20 mV 40 pA	-20 mV 0.2 nA
Setpoint for IETS and THz RS	40 mV 0.8 nA	10 mV 0.2 nA	10 mV 0.2 nA	-60 mV 1 nA	20 mV 40 pA	-500 mV 1.5 nA	-20 mV 40 pA	-20 mV 0.2 nA
IETS RMS Bias Modulation	3 mV	3 mV	3 mV	3 mV	3 mV	7 mV	3 mV	5 mV
THz Frequency for THz RS	400 GHz	400 GHz	400 GHz	400 GHz	400 GHz	300 GHz	400 GHz	400 GHz

To better understand the relation between THz far field intensity and THz rectification current, a series of THz RS at 150GHz is measured over CO adsorbed on Ag(110) with different THz powers controlled by V_{PCA} (Figure 2.3a). A significant peak broadening is observed with increasing THz power. By fitting each THz RS from a reference IETS with known bias modulation amplitude (see details of fitting process in Supporting Information 2.3.5), we obtain the THz induced voltage at STM junction (V_{THz}) for each value of V_{PCA}. The fitted THz RS curves exhibit good consistency with measured data in both line shape and signal intensity and fitted V_{THz} is displayed as a function of V_{PCA} in Figure 2.3b, together with the THz photocurrent detected by PCA receiver in ambient setup with coherent detection (see Supporting Information 2.3.3). Since the photocurrent measured by THz receiver is proportional to THz far field intensity, the linear relation between the fitted V_{THz} and the THz photocurrent (Figure 2.3b inset) therefore indicates a linear dependence of V_{THz} on THz far field intensity, whose slope indicates the relative nearfield enhancement at STM junction.

By fitting the THz RS directly with 2 pairs of symmetric Lorentzian peaks, the peak heights and peak $FWHM^2$ of the CO HR peak on the positive bias side are extracted and displayed against V_{THz} and V_{THz}^2 respectively in Figure 2.3c and 3d. In Figure 2.3c, a linear relation between peak height and V_{THz} in the probed range of THz intensity can be resolved with a negative intercept. Simulation of HR peak height as a function of V_{THz} indicates that for small values of V_{THz} (i.e., < 5mV), a non-linear quadratic dependence that follows the Taylor expansion under small-modulation approximation [30] can be expected, which explains the negative intercept (see Supporting Information 2.3.6).

On the other hand, the linear relation between $FWHM^2$ and V_{THz}^2 agrees well with the theoretical expression of FWHM [4,30]:

$$\mathrm{FWHM} = \sqrt{{W_{\mathrm{intrinsic}}}^2 + \mathrm{K}\,(\mathrm{V_m})^2 + \left(\frac{5.4\mathrm{k_B T}}{\mathrm{e}}\right)^2} \qquad (2.1)$$

Here $W_{\mathrm{intrinsic}}$ represents the intrinsic broadening, $\sqrt{K}\,V_m$ is the finite modulation broadening with a bias modulation amplitude V_m, and $\frac{5.4k_BT}{e}$ is the thermal broadening at temperature T. The Finite modulation broadening $\sqrt{K}\,V_m$ can be computed as the FWHM of the instrumental function for the type of modulation. In the case of THz rectification, $V_m = V_{THz}$ and K =0.52. The slope of 0.61 obtained from Figure 2.3d agrees well with the theory, which validates fitted values of V_{THz}. The fitting has also revealed small blueshift in HR and HT peak energies for THz RS obtained with large THz field intensity, and this is explained by THz induced nearfield streaking effect of tunneling electrons when effective junction bias is steered opposite to the DC bias under THz near field (see discussion in Supporting Information 2.3.6).

Beside the broadening effect in THz RS from THz field modulation, we have also observed peak splitting in IETS obtained with a constant amplitude THz field radiation. As shown in Figure 2.4a, a series of IETS of CO adsorbed on Ag(110) were taken under 150GHz radiation with different THz far field intensities and compared to a reference IETS taken at the same set point and the same $3mV_{rms}$ sinusoidal bias modulation but no THz illumination. A gradually increased peak splitting in the IETS line shape is observed with increasing THz field. The waveform of IETS with THz illumination can be mathematically expressed as a convolution between the reference IETS (no THz illumination) and a probability weight function of the THz induced bias modulation [1,31]:

$$S_{on}(V_0, V_{THz}) = \int_{V_0 - V_{THz}}^{V_0 + V_{THz}} S_{off}(V) w(V, V_0, V_{THz}) dV \qquad (2.2)$$

Here, $S_{on}(V_0, V_{THz})$ is the IETS signal at bias V_0 with V_{THz} being the THz induced voltage drop at junction. $S_{off}(V)$ is the reference IETS and $w(V, V_0, V_{THz})$ is the weight function representing the normalized probability distribution of sinusoidal bias modulation induced by THz field. The weight function for a sine wave THz induced bias modulation is written as:

$$w(V, V_0, V_{THz}) = \frac{1}{\pi \sqrt{V_{THz}^2 - (V - V_0)^2}}, \qquad |V - V_0| < V_{THz} \tag{2.3}$$

By fitting the IETS with THz radiation to Eq. (2.2) and (2.3), V_{THz} was extracted for each value of V_{PCA} used and showed good consistency to the THz photocurrent measured by PCA receiver (Figure 2.4b). The linear fit of V_{THz} against THz photocurrent yields a slope smaller than that presented in Figure 2.3b inset, indicating a smaller nearfield field enhancement of THz at STM junction due to different THz beam alignment at the time IETS were taken with THz illumination. Using this method, V_{THz} was measured at different tip-substrate distances (Figure 2.4d) and found to be constant within the range of tunneling gap measured. Previous study has shown that when tip-substrate distance is far smaller than THz wavelength, field retardation is negligible and the THz nearfield at junction can be viewed as a quasistatic field between the tip and substrate, which leads to a constant THz voltage at junction as a function of tip-substrate distance [32]. Here, the measured tip-substrate gap range is estimated to be from 3.23 Angstrom to 4.25 Angstrom (see details for estimation of tunneling gap in Supporting Information 2.3.7), therefore the quasi-static approximation is expected to be valid for the full range of THz frequency (50 to 1290 GHz) provided by our experimental setup, which validates our observation at 150 GHz.

Figure 2.3 THz rectification spectra (RS) with various THz field intensity. (a) THz RS taken with Ag tip over CO adsorbed on Ag(110) substrate (set point 40 mV, 0.8 nA) with 150 GHz field at various field intensity. A 273 Hz square wave with high level fixed at 0.3V and variable low level as indicated in (a) is supplied to PCA emitter. Colored data are experimental measurements and solid curves are fitted data. Spectra are scaled up and offset for clarity. (b) Comparison between fitted THz-induced voltage drop across tip-substrate junction (V_{THz}) and the THz photocurrent measured by PCA receiver with ambient coherent detection as a function of voltage applied to PCA (V_{PCA}). Inset shows fitted V_{THz} as a function of THz photocurrent measured by PCA receiver (red circles) and the linear fit between the two variables (black line). (c) (d) Peak height and $FWHM^2$ of HR mode at 19.5meV as a function of the fitted V_{THz} and V_{THz}^2 respectively. Both Peak Height and FWHM (red circles) are obtained through Lorentzian fitting of the spectra and the linear fit results are displayed as black lines.

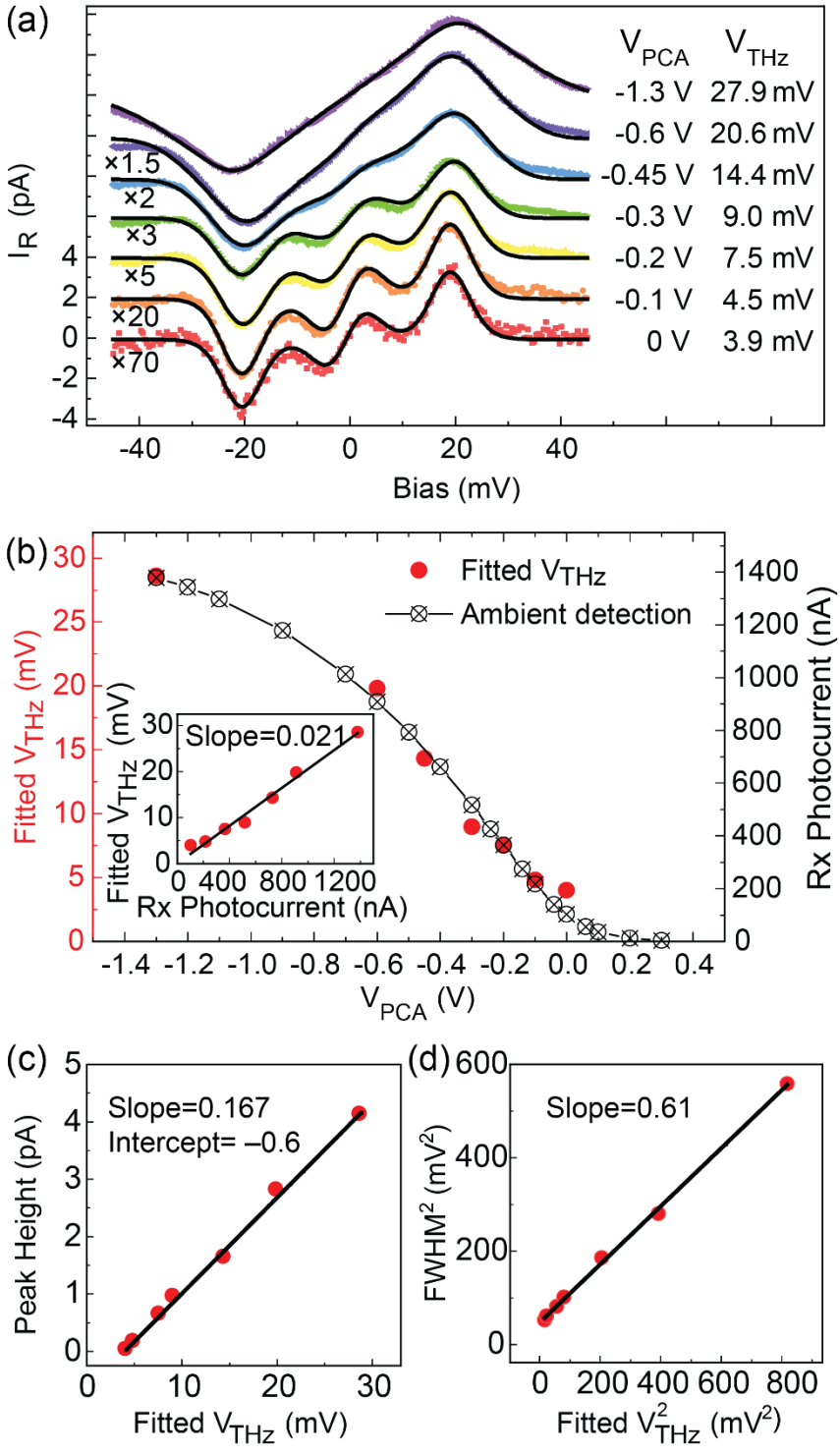
(a)
V_{PCA} V_{THz}
-1.3 V 27.9 mV
-0.6 V 20.6 mV
-0.45 V 14.4 mV
-0.3 V 9.0 mV
-0.2 V 7.5 mV
-0.1 V 4.5 mV
0 V 3.9 mV
×1.5
×2
×3
×5
×20
×70
I_R (pA)
Bias (mV)
(b)
Fitted V_{THz}
Ambient detection
Fitted V_{THz} (mV)
Rx Photocurrent (nA)
Slope=0.021
Fitted V_{THz} (mV)
Rx Photocurrent (nA)
V_{PCA} (V)
(c)
Slope=0.167
Intercept= –0.6
Peak Height (pA)
Fitted V_{THz} (mV)
(d)
Slope=0.61
FWHM^2 (mV^2)
Fitted V^2_{THz} (mV^2)

Figure 2.4 THz-field-induced IETS line shape change and set point dependence of THz-induced voltage drop (V_{THz}) across STM junction. (a) IETS of Ag tip over CO adsorbed on Ag(110) substrate taken without THz and with 150GHz radiation at various THz far field intensities controlled by the voltage supplied to PCA emitter (V_{PCA}). The colored dots are experimental data and solid curves are fitted data. All spectra here are taken with gap set point 40 mV, 0.8 nA and an RMS bias modulation of 3 mV. Spectra are offset for clarity. (b) Comparison between fitted V_{THz} and the THz photocurrent detected by PCA receiver with ambient coherent detection as a function of V_{PCA}. Inset shows V_{THz} as a function of PCA receiver photocurrent and the linear fit between the two variables (black line). (c) Schematic diagram showing the increasing direction of change in tip-substrate gap, ΔZ. (d) Computed V_{THz} as a function of ΔZ, with $\Delta Z = 0$ defined as gap with set point 40 mV/2 nA. V_{THz} is computed by fitting IETS with non-chopped THz at 150GHz and V_{PCA} =-0.35V. Error bars indicate 95% confidence interval for fitting result. No significant variation in V_{THz} is observed within the range of tunneling gap used.

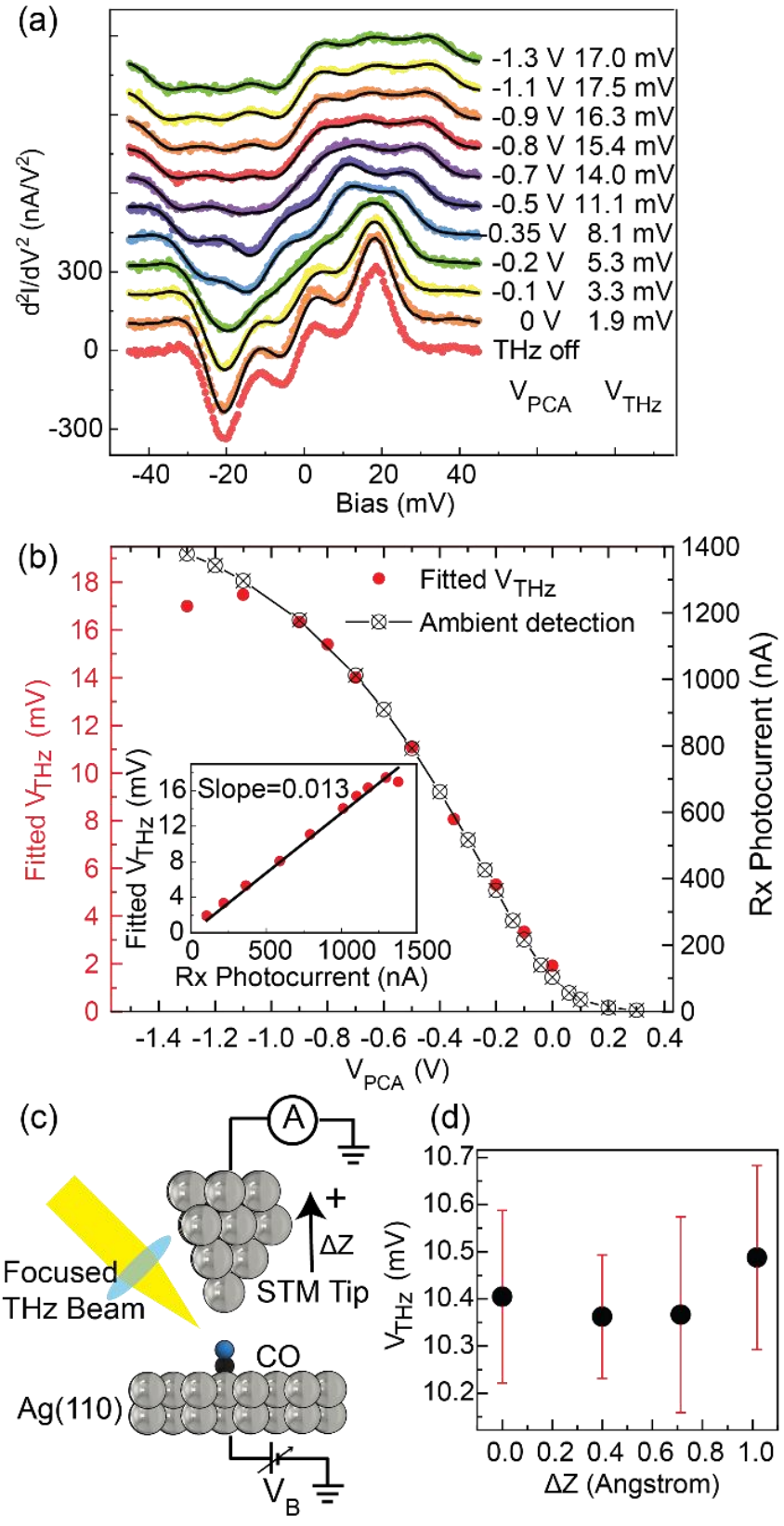
(a)
-1.3 V 17.0 mV
-1.1 V 17.5 mV
-0.9 V 16.3 mV
-0.8 V 15.4 mV
-0.7 V 14.0 mV
-0.5 V 11.1 mV
0.35 V 8.1 mV
-0.2 V 5.3 mV
-0.1 V 3.3 mV
0 V 1.9 mV
THz off
V_PCA V_THz
d²I/dV² (nA/V²)
300
0
-300
-40 -20 0 20 40
Bias (mV)
(b)
Fitted V_THz
Ambient detection
Fitted V_THz (mV)
Rx Photocurrent (nA)
Slope=0.013
Fitted V_THz (mV)
Rx Photocurrent (nA)
V_PCA (V)
(c)
A
+
ΔZ
Focused
THz Beam
STM Tip
CO
Ag(110)
V_B
(d)
V_THz (mV)
ΔZ (Angstrom)

In summary, we successfully coupled CW THz radiation to a LT-STM junction and measured the THz rectification current over different single molecules at STM junction. The THz induced voltage drop at STM junction was shown to be linearly proportional to far-field THz field intensity, but independent of tip-substrate gap within the regime of quasistatic approximation. The THz RS taken over different single molecules was shown to reflect the same information on vibrational, rotational and spin excitation as the traditional IETS measurement. With the frequency response-induced line shape change in RS for pyrrolidine and hydrogen, we show that THz-induced fast oscillating nearfield at tunneling junction can be potentially used to study the frequency response in molecules that exhibit conductance switching at a sub-THz level switching rate. The THz far field sensitivity in rectification current at the CO HR peak also suggests the great potential in using a single molecule as a THz sensor with atomic spatial resolution. Lastly, with the high energy resolution provided by the CW THz source and atomic scale spatial resolution provided by STM, CW THz rectification current measurement in frequency domain spectroscopy could be performed to probe coherent excitation in single molecules and atoms.

2.3 Supporting Information

2.3.1 Tip and Sample Preparation

All measurements presented are done with an atomic-sharp silver tip. The tip is prepared by repeated cycles of Neon bombardment at up to 1.5 keV and annealing. After sample is approached to tunneling distance, tip is further sharpened by gentle poking at surface. Substrate Ag(110) and Cu(100) are prepared in UHV chamber with repeated cycles of Neon bombardment at 1 keV energy and annealing at 500 ℃ and 650 ℃ respectively. Copper nitride islands are formed by bombarding clean Cu(100) surface at room temperature with 1keV nitrogen gas at 6E-6 torr pressure for 45 s, then followed by 4 min heating at 365 ℃.

2.3.2 Focusing and Aligning THz Beam into STM Junction

As THz radiation is invisible to human eye and long-distance transmission loss is high due to imperfect collimation, it is not feasible to align THz beam by detecting the STM-sample-reflected THz beam at the exiting optical port. Therefore, a 635nm diode laser (Thorlabs, Inc. CPS535R) is used as a guide laser (Figure 2.5) for pre-alignment. The laser diode is mounted in a 3-inch-long lens tube segment that replaces a lens tube of the same length containing PCA emitter and TPX collimating lens. The same Tsurupica lens is used for the focusing of 635nm laser beam and THz beam. The entire lens tube assembly is mounted on a 3-axis piezo-actuated optical mount that allows for fine tuning in both X, Y tilt and Z focus. The image of tip-substrate junction with reflected light from STM sample is collimated by a second lens near the exiting viewport, redirected by 2 mirrors and eventually focused into a CMOS camera (Thorlabs DCC1545M). An example camera view when laser beam is aligned at tip-substrate junction is shown in Figure 2.5

inset. After the laser beam is aligned, the lens tube assembly is resumed with the PCA emitter and TPX lens segment. The THz beam is ideally coaxial with the guide laser beam and therefore is roughly aligned to tip-substrate junction. The possible alignment offset due to switching optical assembly is small compared to the THz beam size, which was experimentally determined to be ~3 mm for THz power FWHM at 500 GHz. To further optimize THz alignment at junction, use the THz rectification signal over a molecule as indicator and maximize the signal by fine tuning the alignment.

Figure 2.5 Schematic diagram of the setup for THz pre-alignment with 635 nm diode laser. The laser beam is dimmed by a ND filter and then focused by a Tsurupica lens. The laser power exiting the Tsurupica lens is 11 μW. After the focused beam is aligned to STM junction with a CMOS camera, the 635 nm diode laser and ND filter assembly is replaced with PCA emitter assembly (including PCA emitter and a TPX lens for THz beam collimating) for further alignment optimization by maximizing THz-induced rectification current from a single molecule such as CO. Inset shows a camera view of beam aligned to junction, revealing a faint shadow of the tip apex and the mirrored tip image due to substrate reflection, as indicated by red dashed lines.

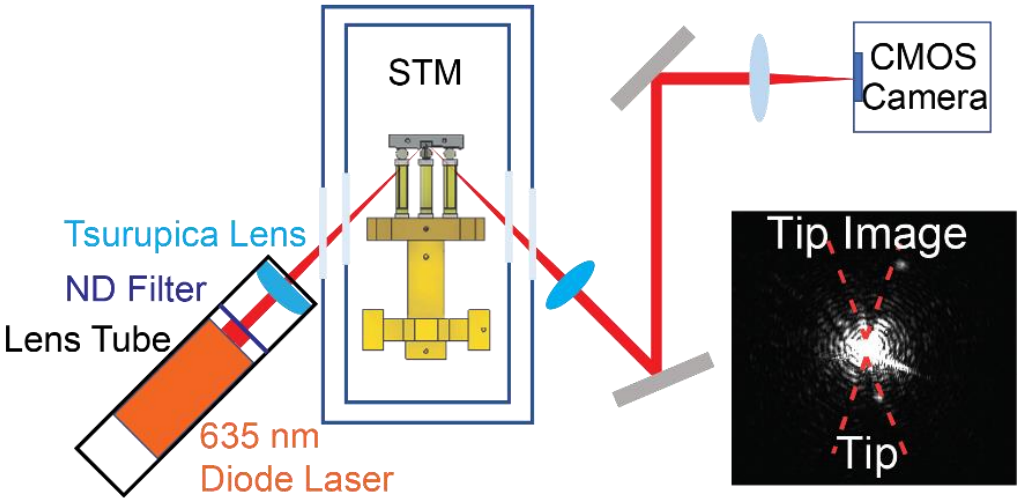

2.3.3 Coherent Detection of THz in ambient environment

For ambient detection of free-space THz radiation, the PCA receiver, a semiconductor photo mixer, is used to capture the electric field from THz wave as shown in Figure 2.6a. When the optical beatings at frequency f excite carriers in PCA emitter, THz radiation is driven and accelerated forward with a field $E_{THz} = A\cos(2\pi ft)$. With the same optical beatings irradiated on the PCA receiver, carriers are excited and then driven by the THz electric field. The photocurrent generated in the PCA receiver I_{Rx} is proportional to the momentary THz field intensity E_{THz}', which is delayed by a phase $\Delta\varphi$ relative to the optical beatings due to THz propagation:

$$I_{Rx} \propto E_{THz}' = E_{THz}\cos(\Delta\varphi) \tag{2.4}$$

$$\Delta\varphi = 2\pi f \Delta L/c$$

Here, ΔL is the optical path in air. For other medium/samples in the path, $\Delta L = \sum n\Delta l$, where n is the refractive index of each medium/sample and Δl is the corresponding propagation length. When scanning the THz frequency, $\Delta\varphi$ will change linearly with f and result in periodic oscillation in the receiver photocurrent I_{THz}, as shown in Figure 2.6b. The fringe caused by the interference between the coherent THz radiation and the optical beatings. The envelop of the fringes, which scales linearly with the actual THz field amplitude E_{THz}, is extracted from a FDS measurement of the photocurrent and displayed in Figure 2.6c and d to show the THz far field intensity as a function of frequency and PCA emitter voltage. The receiver photocurrent is also measured with lock-in detection, with a square wave chopping voltage applied to PCA emitter.

Figure 2.6 Ambient THz field detection with coherent measurement. (a) The experimental setup for coherent detection of THz field. The same lens tube assembly is used for coupling THz radiation to STM junction in Figure 2.1a. (b) Examplary measurement of PCA receiver photocurrent fringes (black curve) from coherent detection and calculated field amplitude (red curve) based on measured data. The dip in field amplitude at 1163GHz is due to THz absorption by water vapor in air. (c) The frequency domain spectra (FDS) obtained using setup in (a) with and without nitrogen gas purging in the path to achieve low and high humidity levels. Transmittance is computed as $\left|\frac{\text{Photocurrent}_{40\%\text{ Humidity}}}{\text{Photocurrent}_{10\%\text{ Humidity}}}\right|^2$ to reveal strong water vapor absorption at multiple frequencies. (d) PCA emitter voltage (V_{PCA}) dependence of THz-induced PCA receiver photocurrent sampled at different THz frequencies using coherent detection setup in (a).

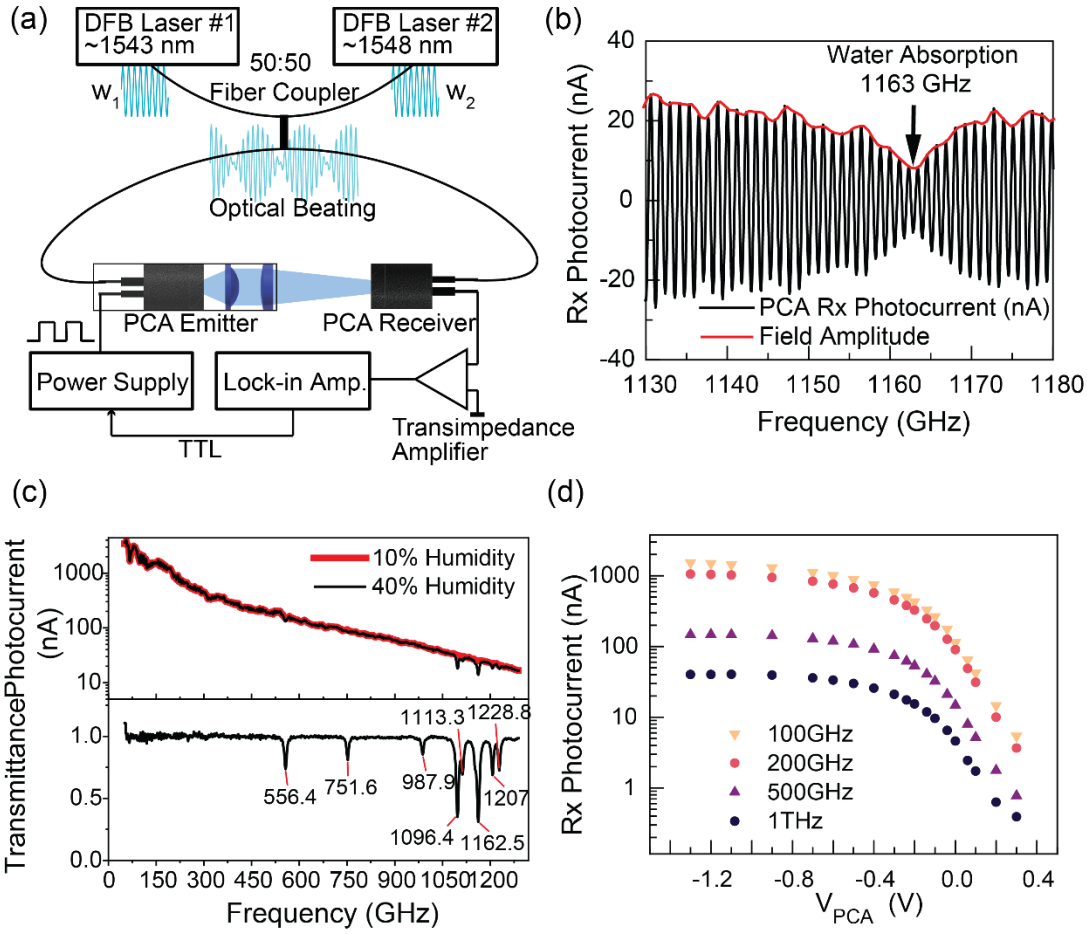
(a)
DFB Laser #1
~1543 nm
DFB Laser #2
~1548 nm
50:50
Fiber Coupler
w1
w2
Optical Beating
PCA Emitter
PCA Receiver
Power Supply
Lock-in Amp.
TTL
Transimpedance
Amplifier
(b)
Water Absorption
1163 GHz
Rx Photocurrent (nA)
PCA Rx Photocurrent (nA)
Field Amplitude
Frequency (GHz)
(c)
10% Humidity
40% Humidity
TransmittancePhotocurrent (nA)
1113.3
1228.8
556.4
751.6
987.9
1207
1096.4
1162.5
Frequency (GHz)
(d)
Rx Photocurrent (nA)
100GHz
200GHz
500GHz
1THz
V_PCA (V)

2.3.4 AC RS at Various Modulation Frequency for Hydrogen and Pyrrolidine

To study the relation between RS line shape and modulation frequency, we measured a series of RS with sinusoidal bias modulation (setup shown in Figure 2.7a). The modulation is chopped at fixed low frequency (273 Hz or 255.11 Hz) for each spectra set, with the sine wave modulation frequency varied from 10kHz up to 12.5MHz. The line shape changes drastically between 10kHz to 100kHz and stabilizes above 1MHz for all 3 sets of AC RS displayed in Figure 2.7 (Figure 2.7b, c for hydrogen on copper nitride and Figure 2.7d for pyrrolidine on Cu(100). The AC RS at 10kHz modulation exhibit similar line shapes with IETS displayed in Figure 2.2. A THz RS is also displayed for each AC RS set as a comparison. The similar line shapes between the THz RS and AC RS with modulation above 1MHz indicate there is no further line shape change induced by change in modulation frequency from radio frequency into the THz range. This overall modulation frequency induced line shape change proves that the observed line shape difference between IETS and THz RS is not due to resonance excitation with THz radiation but related with the molecular response to bias modulation in the range of lower frequencies.

Figure 2.7 Line shape change in AC bias induced rectification spectra (RS) of Hydrogen and Pyrrolidine with increasing modulation frequency. (a) Schematic diagram of experimental setup for AC-RS. A chopped sine wave modulation is generated from a function generator (Tektronix AFG31022) and combined with the DC bias from STM interface electronics using a bias tee (Tektronix PSPL5530B). The combined signal is fed to STM sample through electrical connection. The rectification signal is extracted from tunneling current with a lock-in amplifier. (b) AC RS of H_2 on Cu_2N at set point -20 mV/0.2 nA, taken with modulation frequency from 10 kHz to 12.5 MHz, chopped at 255.11 Hz. A THz RS taken at 500 GHz (black curve) is displayed on top for line shape comparison. (c) AC RS of H_2 on Cu_2N at set point -20mV/40pA, taken with modulation frequency from 10kHz to 10MHz, chopped at 255.11 Hz. A THz RS taken at 415 GHz (black curve) is displayed on top for line shape comparison. (d) AC RS of Pyrrolidine (only C-H stretch mode) over $Cu(100)$ substrate, taken with modulation frequency from 10kHz to 2.56MHz, chopped at 273 Hz. A THz RS taken at 300GHz (black curve) is displayed on top for line shape comparison. All spectra in (b) - (d) are offset for clarity.

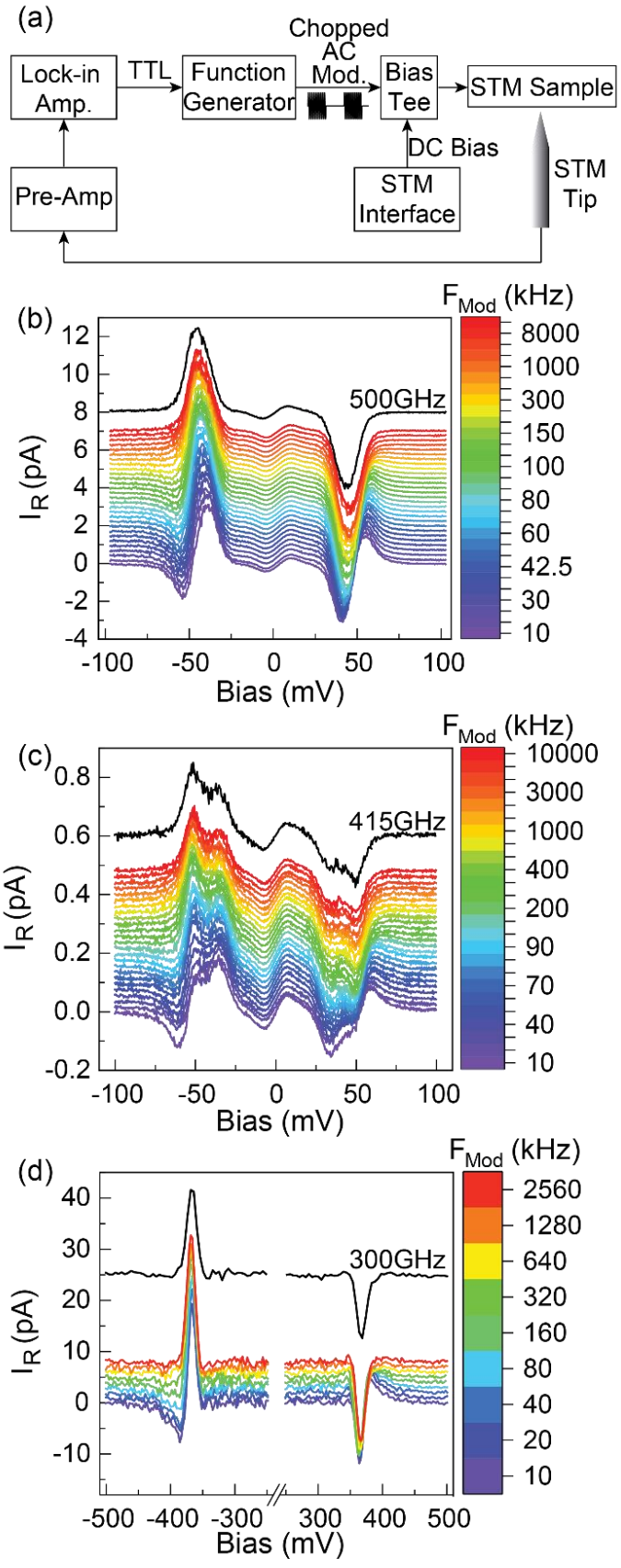
(a)
Lock-in Amp.
TTL
Function Generator
Chopped AC Mod.
Bias Tee
STM Sample
DC Bias
STM Interface
STM Tip
Pre-Amp
(b)
F_Mod (kHz)
8000
1000
300
150
100
80
60
42.5
30
10
500GHz
I_R (pA)
Bias (mV)
(c)
F_Mod (kHz)
10000
3000
1000
400
200
90
70
40
10
415GHz
I_R (pA)
Bias (mV)
(d)
F_Mod (kHz)
2560
1280
640
320
160
80
40
20
10
300GHz
I_R (pA)
Bias (mV)

2.3.5 Fitting of THz RS from IETS

The idea of fitting THz RS from a reference IETS with known bias modulation amplitude is based on the mathematical connection between the two types of spectroscopies. Both IETS and THz RS signals can be written as a convolution between $\frac{\mathbf{d^2I}}{\mathbf{dV^2}}(\mathbf{v})$ and an instrumental function that's dependent on the modulation waveform type and amplitude V_m [4]:

$$I_s(v) = \int_{-V_m}^{+V_m} \frac{d^2I}{dV^2}(v + v') \cdot \phi(V_m, v')\, dv' \tag{2.5}$$

The mathematical forms of instrumental function for IETS measurement ($\phi_{2\omega}(V_m, v)$) and rectification measurement ($\phi_R(V_m, v)$) are different and can be found in references [4,30] respectively. V_m is replaced with V_{THz} in the case of THz Rectification spectra fitting.

The fitting process of the THz RS contains 2 steps. The first step is to obtain the waveform of $\frac{d^2I}{dV^2}(v)$ by fitting an IETS with known bias modulation amplitude V_m to Eq. (2.5), and the second step is to fit THz RS to Eq. (2.5) according to the obtained $\frac{d^2I}{dV^2}(v)$ waveform. To do so, we need to first have an explicit waveform of $\frac{d^2I}{dV^2}(v)$.

The symmetric tunneling current term based on the non-equilibrium Green's function formalism and lowest order expansion approximation[33] is used to derive the waveform of $\frac{d^2I}{dv^2}(v)$:

$$I_{Symmetric}(v) = \frac{e}{\pi\hbar}\left(2evn + \frac{\hbar\Omega - ev}{e^{(\hbar\Omega - ev)/k_BT} - 1} - \frac{\hbar\Omega + ev}{e^{(\hbar\Omega + ev)/k_BT} - 1}\right) \tag{2.6}$$

Here $\hbar\Omega$ represents the excitation energy of a vibrational/rotational mode, T is the temperature of tunneling junction, v is the sample bias, n is the steady state occupation of electrons.

$\frac{d^2I}{dV^2}(v)$ is derived as below from Eq. (2.6):

$$\frac{d^2I}{dV^2}(v,b,A,w) = A * \left[\frac{e^{\frac{2(b-v)}{w}}(b-v) + e^{\frac{b-v}{w}}(b-v) - 2we^{\frac{b-v}{w}}\left(e^{\frac{b-v}{w}} - 1\right)}{\left(e^{\frac{b-v}{w}} - 1\right)^3 w^2} - \frac{e^{\frac{2(b+v)}{w}}(b+v) + e^{\left(\frac{b+v}{w}\right)}(b+v) - 2e^{\left(\frac{b+v}{w}\right)}\left(e^{\left(\frac{b+v}{w}\right)} - 1\right)w}{\left(e^{\frac{b+v}{w}} - 1\right)^3 w^2} \right] \quad (2.7)$$

Here, $b = \frac{\hbar\Omega}{e}$ is the center bias of the peak measured in IETS or THz RS; $A = \frac{e^2}{\pi\hbar}$ is a peak height factor; $w = \frac{k_B T}{e}$ is a peak width factor associated with the thermal broadening at temperature T. This equation can be viewed as 2 independent parts, the first of which represents the positive bias side peak, whereas the second part represents the symmetric negative bias side peak.

For CO on Ag(110), we observe both hindered translation (HT) mode and hindered rotation (HR) mode within the measured bias range. therefore $\frac{d^2I}{dV^2}(v)$ is the sum of two modes:

$$\frac{d^2I}{dV^2}(v) = \frac{d^2I}{dV^2}(v, b_1, A_1, w) + \frac{d^2I}{dV^2}(v, b_2, A_2, w) \quad (2.8)$$

Where b_1, A_1 are the peak center and peak height factor for HR mode and b_2, A_2 the peak center and peak height factor for HT mode of CO on Ag(110). w is a shared peak width parameter for both modes. In the actual fitting process, an extra parameter V_{off} is introduced to compensate instrumental bias offset at the STM junction, resulting in the final $\frac{d^2I}{dV^2}$ form:

$$\frac{d^2I}{dV^2}(v) = \frac{d^2I}{dV^2}(v + V_{off}, b_1, A_1, w) + \frac{d^2I}{dV^2}(v + V_{off}, b_2, A_2, w) \quad (2.9)$$

Combining Eq. (2.5) and (2.9), parameters $\mathrm{b}_1, \mathrm{A}_1, \mathrm{b}_2, \mathrm{A}_2, \omega, \mathrm{V}_{\mathrm{off}}$ can be obtained from fitting a measured IETS with known value of modulation amplitude $V_{2\omega}$. These parameters can then be used in step two for fitting the THz RS and obtaining value of V_{THz}. Note that the IETS data used for fitting is background subtracted to maintain a good line shape that's consistent with the $\frac{d^2I}{dV^2}(v)$ waveform used, and each THz RS is also background subtracted for the same purpose.

By fitting THz RS with all 6 parameters $b_1, A_1, b_2, A_2, \omega, V_{off}$ obtained from IETS, we have observed poor fitting result for larger THz field intensities as shown in Figure 2.8a. A significant blueshift of HR peaks can be visualized at high THz powers compared to the fitted curves with fixed peak position. This can be potentially induced by the THz field streaking of tunneling electrons when the junction nearfield is steered opposite to the DC bias field due to large THz field intensities, which cause the rectification current to reduce on the lower bias side of the peak, resulting in a blue shift in peak positions. Such peak shift has resulted in poor fitting and overestimated V_{THz} values under large THz intensity as shown in Figure 2.8a and b. To compensate this effect for more accurate fitting of V_{THz}, an improved fitting is done by fixing only the parameters $w, A_1 \; and \; A_2$ from IETS fitting and loosening the parameters b_1, b_2, V_{off} to be fitted from THz RS (result displayed in Figure 2.3). As shown in Figure 2.8c, the improved fitting with the values of b_1, b_2, V_{off} obtained from THZ RS fitting (scattered data) shows an increased deviation for both HT and HR peak positions from the IETS fitted values (dashed lines) with increasing THz field, where HT peak blueshift occurs with a smaller onset value of THz intensity compared to the HR peak due to the lower bias of its peak position.

Figure 2.8 Comparison between parametric fittings of THz RS. (a) Fitted curves (black curves) for THz RS obtained with fixed parameters $b_1, A_1, b_2, A_2, \omega, V_{off}$ obtained from IETS fitting. Colored data are THz RS measurements with different PCA emitter voltage. (b) Comparison of the V_{THz} estimated by 2 different parametric fittings of THz RS, plotted as a function of THz induced photocurrent in PCA Receiver. Fitting 1 is done by fixing all 6 parameters $A_1, A_2, \omega, b_1, b_2$ *and* V_{off}. And Fitting 2 is the improved THz RS fitting done by only fixing A_1, A_2, ω obtained from IETS fitting while setting b_1, b_2 *and* V_{off} as parameters to be fit. (c) b_1, b_2 *and* V_{off} obtained from improved THz RS fitting (fitting 2) (scatter plots) compared with the values used for fitting 1 (dashed lines), as a function of THz induced photocurrent in PCA receiver, the fitted parameters correspond to fitting curves displayed in Figure 2.3a.

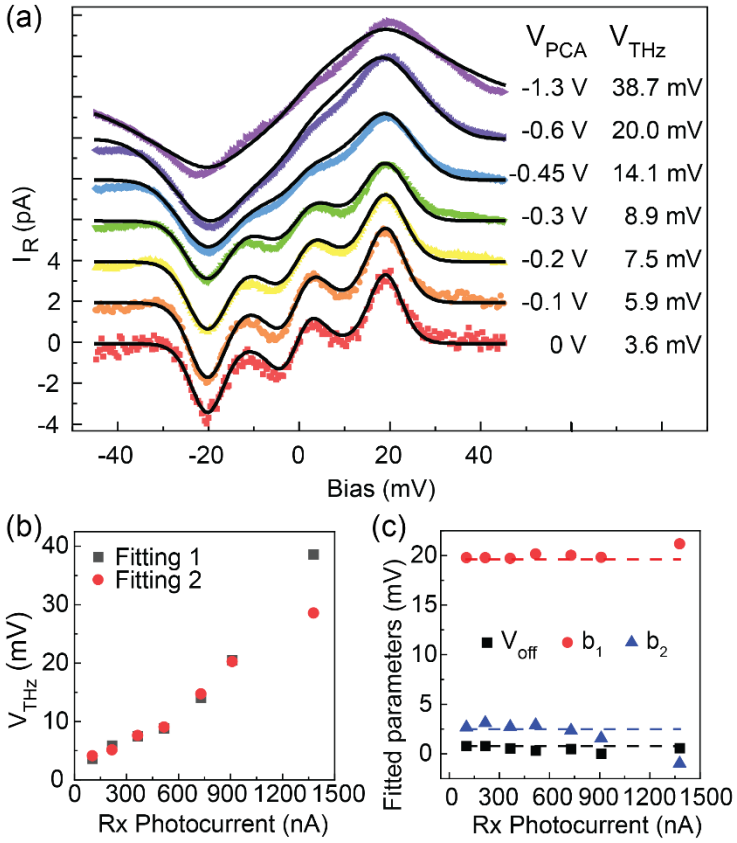

2.3.6 Simulation of THz RS Peak Height as a Function of V_{THz}

To better understand how THz RS peak signal scales with the V_{THz}, we calculate the THz RS signal at HR peak position V_{peak} using the equation below rewritten from Eq. (2.5):

$$I_R(b_1, V_{THz}) = \int_{-V_{THz}}^{+V_{THz}} \frac{d^2I}{dV^2}(b_1 + v) \cdot \phi_R(V_{THz}, v)\, dv \tag{2.10}$$

Here, three different models of $\frac{d^2I}{dV^2}(v)$ are used to investigate the influence of nearby peaks on the peak height calculated (Figure 2.9b). For the first model $\frac{d^2I}{dV^2}(v) = \frac{d^2I}{dV^2}(v + V_{off}, b_1, A_1, w) + \frac{d^2I}{dV^2}(v + V_{off}, b_2, A_2, w)$ is used. For the second model, $\frac{d^2I}{dV^2}(v) = \frac{d^2I}{dV^2}(v + V_{off}, b_1, A_1, w)$ is used to include only the two symmetric peaks of HR mode. For the third model, only the positive peak term in $\frac{d^2I}{dV^2}(v + V_{off}, b_1, A_1, w)$ is included to simulate the case when there's only one isolated peak.

The parameters $A_1, b_1, A_2, b_2, w, V_{off}$ are first obtained by fitting an IETS with known bias modulation to Eq. (2.5) and then applied to the different $\frac{d^2I}{dV^2}(v)$ models above. It is worth noting that although $\frac{d^2I}{dV^2}(v, b, A, w)$ has singularities at $v = \pm b$, $\lim_{v \to \pm b} \frac{d^2I}{dV^2}(v)$ does exist, therefore the numerical integration is still valid.

The calculation of HR peak height (at +19.6 mV) is plotted against V_{THz} for all three models of $\frac{d^2I}{dV^2}(v)$ as shown in Figure 2.9b. For $V_{THz} < 18\, mV$, peak heights calculated for all three models align well with each other and for $V_{THz} < 5\, mV$ they all fit to $I_R(b_1) = 0.235\, V_{THz}^2 \frac{d^2I}{dV^2}\Big|_{b_1}$, which is very close to the rectification term $\frac{V_{THz}^2}{4} \frac{d^2I}{dV^2}\Big|_{b_1}$ from second order Taylor expansion of $I(V_{peak} + V_{THz} cos\omega t)$ under small modulation amplitude assumption[30]. For $V_{THz} > 15mV$,

the behavior of three curves becomes very different. Peak height increases linearly with V_{THz} for the single peak model and fits to $I_R(b_1) = 2.71\ V_{THz} \frac{d^2I}{dV^2}\Big|_{b_1} - 2.865$. Whereas for the model that contains only symmetric HR peaks, peak height starts to bend down from the single peak model curve at above 40mV as the influence from negative HR peak comes into play. Similarly, for the regular $\frac{d^2I}{dV^2}(v)$ that contains both HR and HT peaks, the upward bending in HR peak height occurs at around 18 mV due to contribution from the HT peak that's 18.3 meV away. With increasing V_{THz} extending the integration range to negative bias range, the negative peaks contribution starts to dominate and lead to downward bending in the curve. For the range of V_{THz} presented in Figure 2.3, only the range between the small amplitude nonlinear region and downward bending is displayed and therefore no significant nonlinearity is visually observed. In a word, we can expect a nonlinear rectification current response to small values of V_{THz} and a linear rectification current response to V_{THz} in the range that doesn't couple adjacent peaks into the probed peak.

Figure 2.9 HR peak height vs THz induced voltage drop across STM junction (V_{THz}). (a) A THz RS (red curve) simulated for $V_{THz} = 5$ mV with Eq. (2.10). The waveform $\frac{d^2I}{dV^2}$ (black curve) is obtained by fitting a reference IETS (3 mV_{rms} bias modulation, blue dots) with Eq. (2.5). (b) Height of the HR peak on positive bias side as a function of V_{THz}. Three different types of $\frac{d^2I}{dV^2}$ models are used for simulation to compare the regular CO THz RS which have 2 pairs of symmetric peaks (green dashed curve) to the special cases when the HT peaks are missing (red dashed curve) and when there is only one positive HR peak (black solid curve). The latter two cases use the same peak position and peak width parameters as the regular $\frac{d^2I}{dV^2}$ model. Inset shows the zoomed-in simulation results for V_{THz}<5 mV.

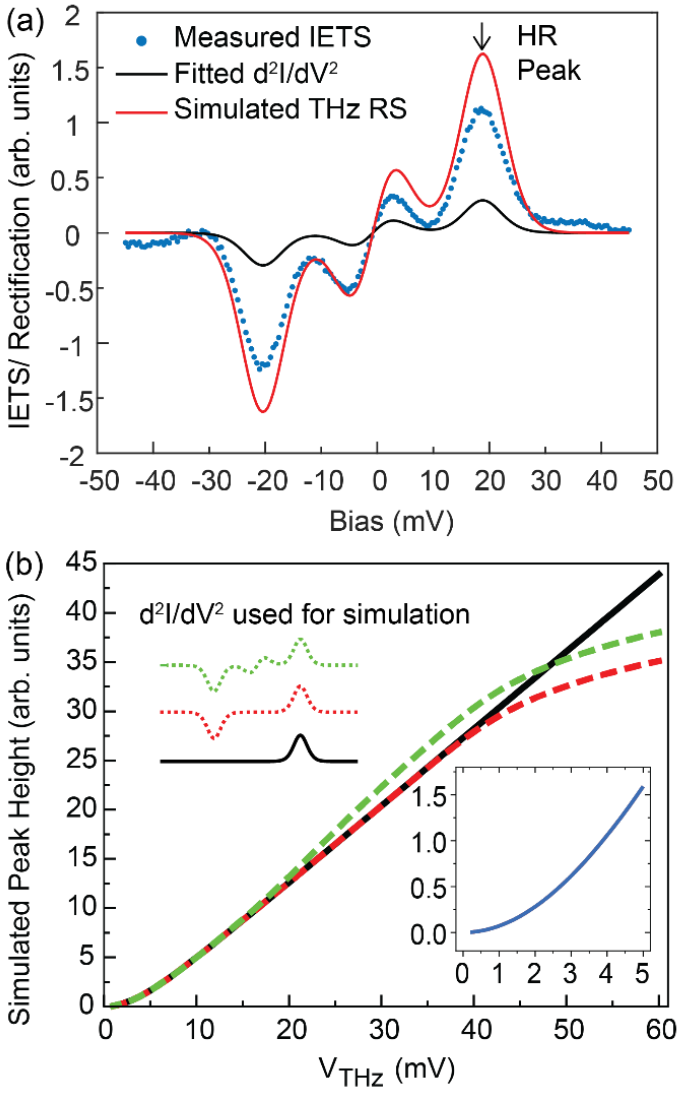
(a)
Measured IETS
Fitted d²I/dV²
Simulated THz RS
HR
Peak
IETS/ Rectification (arb. units)
Bias (mV)
(b)
d²I/dV² used for simulation
Simulated Peak Height (arb. units)
V_THz (mV)

2.3.7 Estimation of Tip-substrate gap

The Tip-substrate gap with tip over a CO molecule for a specific tunneling setpoint can be written as:

$$Z = Z_{Substrate} + \Delta Z_{CO} \tag{2.11}$$

Where $Z_{Substrate}$ is the tip-substrate gap when tip is over substrate, and ΔZ_{CO} represent the relative tip height change when tip goes from substrate to the center of a CO molecule.

On Ag(110) substrate, ΔZ_{CO} was experimentally determined to be -0.02 Angstrom. And $Z_{Substrate}$ is estimated by linear extrapolation of $Log(\frac{G}{G_0})$ as a function of relative gap change ΔZ, where G is the junction conductance, G_0 is the quantum conductance, and ΔZ is relative tip height variation measured at different setpoint current. As shown in Figure 2.10, $Log(\frac{G}{G_0})$ is plotted as a function of ΔZ where $\Delta Z = 0$ is determined by a reference tunneling gap at 40 mV/2 nA. The ΔZ value that correspond to $Log\left(\frac{G}{G_0}\right) = 0$ can be obtained by linear extrapolation, which gives the relative tip height change from the reference tip height to the point-contact position. This tip height change is obtained to be 3.25 Angstrom as indicated in Figure 2.10. Therefore, we can write $Z_{Substrate}$ as:

$$Z_{Substrate} = 3.25 + \Delta Z \tag{2.12}$$

As a result, we obtain an estimated tip-substrate gap distance from 3.23 Angstrom to 4.25 Angstrom for tip over CO with tunneling setpoint between 40 mV/2 nA and 40 mV/0.2 nA.

Figure 2.10 Tip-substrate gap calibration. (a) Extrapolation of relative conductance $\mathrm{Log}(\frac{G}{G_0})$ measured over Ag(110) substrate as a function of relative tip height change ΔZ.(b) Schematic showing the definition for different tip height.

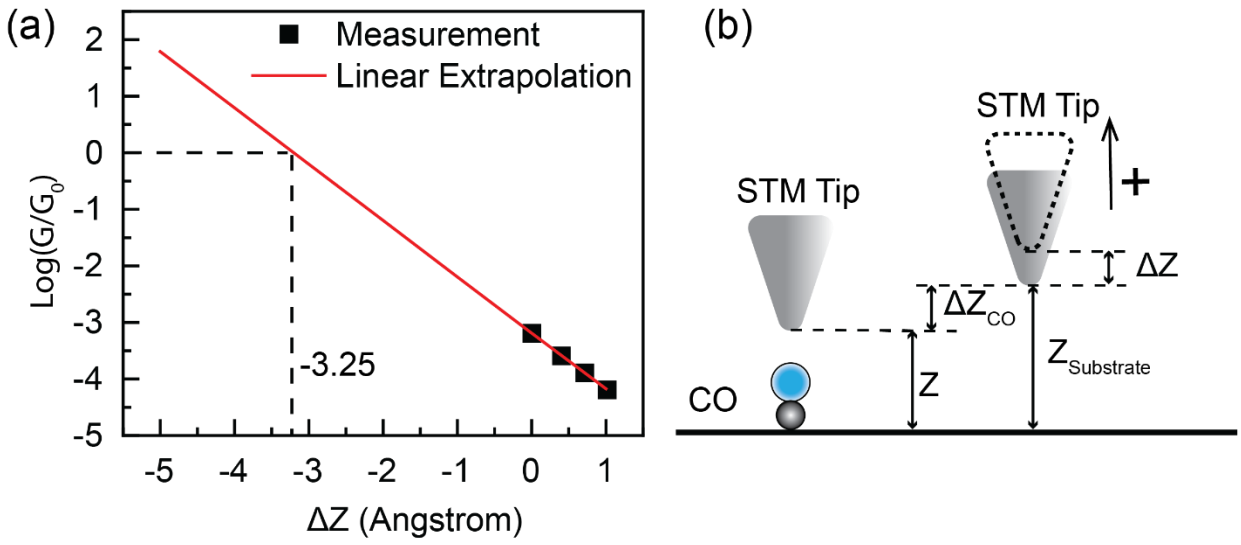

Bibliography

[1] X.W. Tu, J.H. Lee, and W. Ho, *Journal of Chemical Physics*, **124**, 021105 (2006).

[2] J. Lee, X. Tu, and W. Ho, *Nano*, **5**, 2613–2617 (2005).

[3] J. Lee, Characterization of Nanoscale Systems with Microwave Rectification Current, Ph.D. Dissertation, Yonsei University, 2005.

[4] J. Klein, A. Léger, M. Belin, D. Défourneau, and M.J.L. Sangster, *Physical Review B*, **7**, 2336–2348 (1973).

[5] J. Lambe and R.C. Jaklevic, *Physical Review*, **165**, 821–832 (1968).

[6] C.W. Siders, J.L.W. Siders, A.J. Taylor, S.-G. Park, M.R. Melloch, and A.M. Weiner, *Optics Letters*, **24**, 241 (1999).

[7] I. Wilke and S. Sengupta, *Terahertz Spectroscopy: Principles and Applications*, 41–72 (2017).

[8] Y.C. Shen, P.C. Upadhya, H.E. Beere, E.H. Linfield, A.G. Davies, I.S. Gregory, C. Baker, W.R. Tribe, and M.J. Evans, *Applied Physics Letters*, **85**, 164–166 (2004).

[9] R.N. Kini, A.J. Kent, N.M. Stanton, and M. Henini, *Applied Physics Letters*, **88**, 36–38 (2006).

[10] T.L. Cocker, D. Peller, P. Yu, J. Repp, and R. Huber, *Nature*, **539**, 263–267 (2016).

[11] S.L. Lange, N.K. Noori, T.M.B. Kristensen, K. Steenberg, and P.U. Jepsen, *Journal of Applied Physics*, **128**, 070901 (2020).

[12] M. Abdo, S. Sheng, S. Rolf-Pissarczyk, L. Arnhold, J.A.J. Burgess, M. Isobe, L. Malavolti, and S. Loth, *ACS Photonics*, **8**, 702–708 (2021).

[13] T. Tachizaki, K. Hayashi, Y. Kanemitsu, and H. Hirori, *APL Materials*, **9**, 060903 (2021).

[14] M. Eisele, T.L. Cocker, M.A. Huber, M. Plankl, L. Viti, D. Ercolani, L. Sorba, M.S. Vitiello, and R. Huber, *Nature Photonics*, **8**, 841–845 (2014).

[15] Y. Luo, V. Jelic, G. Chen, P.H. Nguyen, Y.J.R. Liu, J.A.M. Calzada, D.J. Mildenberger, and F.A. Hegmann, *Physical Review B*, **102**, 205417 (2020).

[16] T.L. Cocker, V. Jelic, R. Hillenbrand, and F.A. Hegmann, *Nature Photonics*, **15**, 558–569 (2021).

[17] S. Yoshida, Y. Arashida, H. Hirori, T. Tachizaki, A. Taninaka, H. Ueno, O. Takeuchi, and H. Shigekawa, *ACS Photonics*, **8**, 315–323 (2021).

[18] T.L. Cocker, V. Jelic, M. Gupta, S.J. Molesky, J.A.J. Burgess, G.D.L. Reyes, L. v. Titova, Y.Y. Tsui, M.R. Freeman, and F.A. Hegmann, *Nature Photonics*, **7**, 620–625 (2013).

[19] S.E. Ammerman, Y. Wei, N. Everett, V. Jelic, and T.L. Cocker, *Physical Review B*, **105**, 115427 (2022).

[20] V. Jelic, K. Iwaszczuk, P.H. Nguyen, C. Rathje, G.J. Hornig, H.M. Sharum, J.R. Hoffman, M.R. Freeman, and F.A. Hegmann, *Nature Physics*, **13**, 591–597 (2017).

[21] W. Likun, X. Yunpeng, and H. W., *Science*, **376**, 401–405 (2022).

[22] S. Matsuura, M. Tani, and K. Sakai, *Applied Physics Letters*, **70**, 559–561 (1997).

[23] I. Moumane, J. Zbitou, M. Latrach, A. Errkik, O. Chakkor, and A. Fouad, *International Journal of Electrical and Computer Engineering*, **8**, 3801–3808 (2018).

[24] L. Liebermeister, S. Nellen, R. Kohlhaas, S. Breuer, M. Schell, and B. Globisch, *Journal of Infrared, Millimeter, and Terahertz Waves*, **40**, 288–296 (2019).

[25] A. Roggenbuck, H. Schmitz, A. Deninger, I.C. Cámara Mayorga, J. Hemberger, R. Güsten, and M. Grüninger, *New Journal of Physics*, **12**, 1–13 (2010).

[26] C. Kim and T. Ji, *Applied Spectroscopy*, **73**, 1388–1393 (2019).

[27] E. Ohmichi, T. Fujimoto, K. Minato, and H. Ohta, *Applied Physics Letters*, **116**, 051101 (2020).

[28] A. Halbritter, P. Makk, S. Csonka, and G. Mihály, *Physical Review B - Condensed Matter and Materials Physics*, **77**, 075402 (2008).

[29] J. Gaudioso, L.J. Lauhon, and W. Ho, *Physical Review Letters*, **85**, 1918–1921 (2000).

[30] J. Yao, P.J. Wagner, Y. Xia, G. Czap, and W. Ho, *In Preparation*.

[31] W. Paul, S. Baumann, C.P. Lutz, and A.J. Heinrich, *Review of Scientific Instruments*, **87**, 074703 (2016).

[32] M. Müller, N. Martín Sabanés, T. Kampfrath, and M. Wolf, *ACS Photonics*, **7**, 2046–2055 (2020).

[33] M. Paulsson, T. Frederiksen, and M. Brandbyge, *Physical Review B*, **72**, 201101 (2005).

Chapter 3

Single Molecule Photon Equilibrium Action Spectroscopy

3.1 Abstract

We couple tunable lasers to a scanning tunneling microscope (STM) to study the reaction dynamics of vibration-mediated reversible conformational transitions of a single pyrrolidine molecule adsorbed on Cu(001). By introducing the concept of photon reaction equilibrium (K_S), we demonstrate photon equilibrium action spectroscopy (PEAS) for a single pyrrolidine molecule to detect resonant excitation of C-H stretch third overtone and fine features in N-H stretch first overtone region with sub-meV energy resolution. The PEAS measurements are shown to be insensitive to the broad local surface plasmon (LSP) modes and frequency-dependent laser power variation induced by optical setup, which tackles one of the biggest challenges in conventional single molecule laser action spectroscopy and provides a new approach to mode-selective control of a single molecule photo-switch.

3.2 Introduction

Laser combined STM has been widely used to study photo-induced chemical reactions in single molecules. Within tunneling regime, the nano cavity formed by the STM tip and substrate creates localized surface plasmons (LSP) under laser illumination, which greatly confine and enhance the electric field of light near the tip apex. Such field enhancement and confinement have created unique advantage for probing and controlling photoinduced chemical reaction with bond selectivity[1–3]. However, LSP excitation usually create strong and intricate power spectra for junction nearfield. In conventional molecular laser action spectroscopy, photon yield or cross section is measured as a function of photon energy, the results often consist strong features dominated by the LSP induced junction nearfield intensity, and information regarding photon-molecular interaction is blurred [4,5]. On the other hand, for wavelength dependent study, the electric nearfield strength at tunneling junction is also sensitive to optical alignment change induced by transmissive optical elements due to their transmission profile or refractive dispersion. These factors are hard to avoid for different types of optical setups and may lead to spurious features in laser action spectra of a single molecule.

To tackle the above-mentioned challenges, we introduce photon equilibrium action spectroscopy (PEAS) for energy-resolved probing of photo-induced vibrational excitation in the context of a reversible photo-switching molecules. This technique applies to all photo-active systems that exhibits reversible conductance switching when adsorbed on a substrate, such as porphycene[4], azobenzene and its functionalized derivatives[6–8]. Here we demonstrate PEAS over a single pyrrolidine molecule adsorbed on Cu(001) using a scanning tunneling microscope (STM) coupled with wavelength-tunable lasers. Features indicating resonant photoexcitation of vibrational overtones are resolved from such measurements and was shown to be insensitive to junction LSP

mode or optical transmission/alignment variation at different laser frequency. We also demonstrate its application as a sensitive chemical probe by studying the local environment effect of the photon reaction equilibrium.

3.3 Experimental Methods

We couple a wavelength tunable laser into the tunneling junction of a home-built low temperature STM in a UHV chamber (Figure 3.1a). Detailed optical setups for different laser sources are described in Supporting Information 3.6.1. A Cu(001) substrate is prepared in the UHV chamber with repeated cycles of Neon bombardment at 1.5 keV energy and annealing at 650 ℃. All measurements are done with an atomic-sharp silver tip. The tip is prepared by repeated cycles of Neon bombardment at up to 1.5 keV and annealing. After sample is approached to tunneling distance, tip apex is further sharpened by gentle poking on the substrate. Pyrrolidine (>99.5%, Sigma Aldrich) is purified with repeated freeze-pump-thaw procedures and evaporated to a clean Cu(001) substrate cooled to 8K.

When adsorbed on Cu(001) substrate, pyrrolidine has 2 meta-stable envelop forms [9] as shown in Figure 3.1b. We refer the two states as low (L) and high (H), with state H corresponding to a higher tunneling current with constant height probing, or a higher feedback Z with constant current probing. Figure 3.1c shows a constant-current topography of a single pyrrolidine adsorbed on Cu(001). The streaks along the vertical scanning direction reflect reversible transitions between the 2 states during the scan. To quantitively investigate the conformational transition kinetics of a single pyrrolidine molecule, we measure the H → L and L → H transition rates by obtaining the state residence time t_H and t_L from tunneling current traces recorded at constant height mode over center of a pyrrolidine (Figure 3.1d). After sampling t_H and t_L of many consecutive transition cycles, the transition rate for H → L (or L → H) process can be calculated as:

$$R_{H\to L\,(L\to H)} = \frac{1}{T_{H(L)}} \tag{3.1}$$

Here $T_{H(L)} = \overline{t_{H(L)}}$ is the mean value of all sampled state residence times. Note that although we measure only from one molecule, each of the transition events occurs with completely random intervals without inheriting any memory from previous events, therefore, the statistics of a single molecule measurement is equivalent to that of an ensemble measurement.

As a unimolecular reversible chemical reaction, we also define the reaction equilibrium constant as:

$$K = \frac{R_{L\to H}}{R_{H\to L}} \tag{3.2}$$

An increase in K indicates the equilibrium is shifted towards the H state, and vice versa. By this definition, it's intuitive to expect a shift in equilibrium when the $R_{L\to H}$ and $R_{H\to L}$ are not changed by the same proportion. In another word, when there's photoexcitation of certain vibration mode that favors transition in one direction to the other, an equilibrium shift would occur.

With STM probing, we always observe a combined effect from both tunneling electrons and photons, therefore it's important to extract the pure photon contribution from the measurements. It has been experimentally proved that photon-induced switching rate at fixed wavelength and power is a constant add-on to the electron induced switch rate as a function of sample bias [10], therefore we here assume photon induced switching rate to be only dependent of laser frequency and power, given a fixed optical setup.

When junction is illuminated with light, we observe significant increase in transition rate. The linear relation between transition rates and power indicates a single photon process (Figure 3.2a), which has been observed for different laser frequencies. The slope of linear regression from a set of power dependent transition rate measurements is defined as photon rate coefficient m, which is

increase in transition rate per unit power. The photon yield at frequency ν, describing contributions to reaction rate induced per photon, is defined as:

$$Y_{L\to H\ (H\to L)}(\nu) = \frac{m_{L\to H\ (H\to L)}(\nu)}{h\nu} \tag{3.3}$$

Due to the competition between electron and photon in the transition enhancement, we find that the reaction equilibrium constants K computed from $\frac{R_{L\to H}}{R_{H\to L}}$ measured at different biases approach the same level as power increases, which implies that as light power increases, the inelastic tunneling electron induced equilibrium-steering effect gets overridden (Figure 3.2b). Here, we define photon equilibrium constant K_S to be the asymptotic value for K at infinitely high laser power and use it to describe the purely photon-induced reaction equilibrium. K_S at laser frequency ν is written as:

$$K_S(\nu) = \lim_{power\to\infty} K(power, \nu) = \frac{m_{L\to H}(\nu)}{m_{H\to L}(\nu)} \tag{3.4}$$

As $K_S(\nu)$ is only dependent of laser frequency, it's expected to be insensitive to sample bias, the local surface plasma enhancement, and frequency-dependent junction field variation induced by optical setup. Therefore, $K_S(\nu)$ spectra (also known as PEAS) is expected to reveal resonant photoexcitation of vibrational modes that trigger an equilibrium shift in the reversible transition process.

Figure 3.1 The reversible conformational transition of a pyrrolidine adsorbed on Cu(001). (a) A schematic diagram showing a silver STM tip probing the current from a switching pyrrolidine molecule, with tunable laser focused into STM junction at 45-degree incident angle. (b) A schematic diagram of two interchangeable conformational states L and H. State H is defined by either higher Z feedback signal with feedback on, or a higher tunneling current with feedback off. An asymmetric double-well model is used to depict the potential energy (PE) along the reaction coordinate. The bigger potential well depth for state H in this case correspond to a bigger transition rate from state L to H. (c) Constant current topography of a pyrrolidine taken at set point +50 mV, 0.1 nA. Streaks in image indicate frequent switching between two states during the image scanning. (d) Tunneling current time trace measured with constant height probing over center of pyrrolidine (indicated by red star in (c)), taken at bias +50 mV with a tunneling gap set by -500 mV, 1 nA.

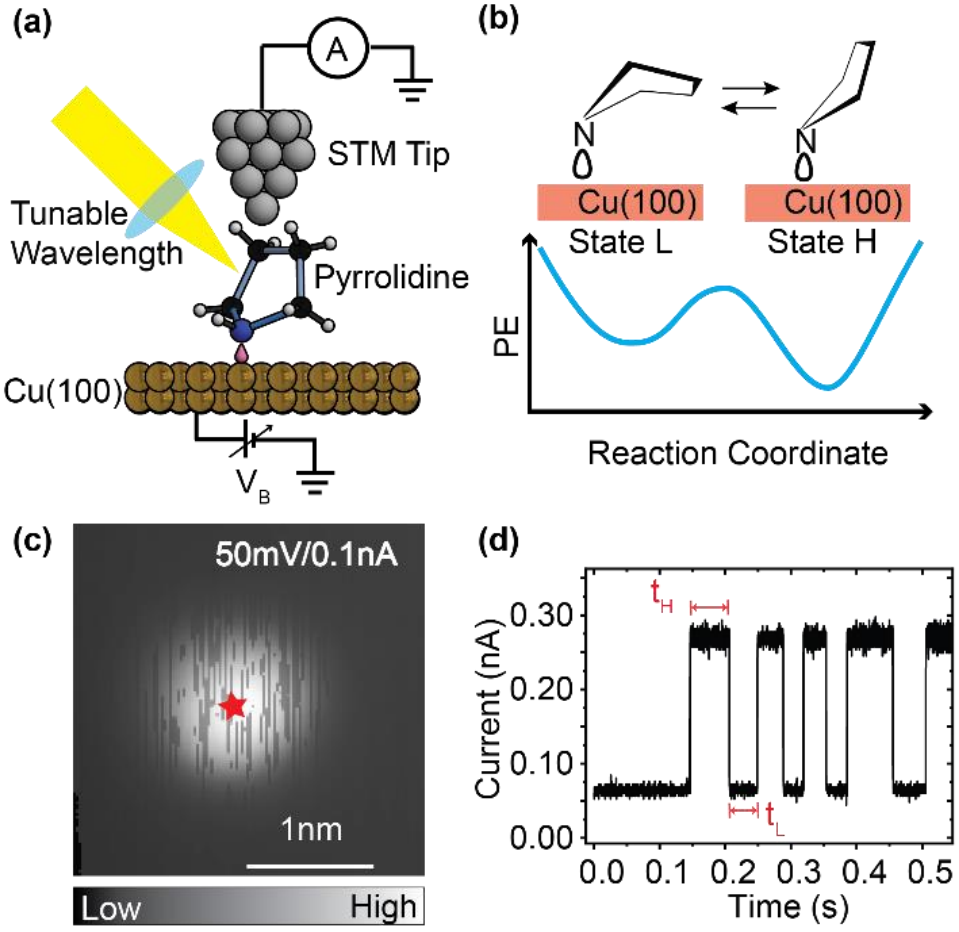
(a)
A
STM Tip
Tunable
Wavelength
Pyrrolidine
Cu(100)
V_B
(b)
N
O
Cu(100)
State L
N
O
Cu(100)
State H
PE
Reaction Coordinate
(c)
50mV/0.1nA
1nm
Low
High
(d)
t_H
t_L
Current (nA)
0.00
0.10
0.20
0.30
0.0
0.1
0.2
0.3
0.4
0.5
Time (s)

Figure 3.2 Laser power dependence of pyrrolidine conformational switching. (a) $R_{L\rightarrow H}$ and $R_{H\rightarrow L}$ as a function of power for 1543.6 nm light, measured at +50 mV with feedback off at set point -500 mV, 1 nA. Black lines are linear fit of the measurement. (b) Reaction equilibrium constant K as a function of power for 1543.6 nm light, measured at -30 mV, -50 mV and +50 mV respectively with feedback off at set point -500 mV, 1 nA. With increasing power, the reaction equilibrium constants measured at different biases approach the same value K_S.

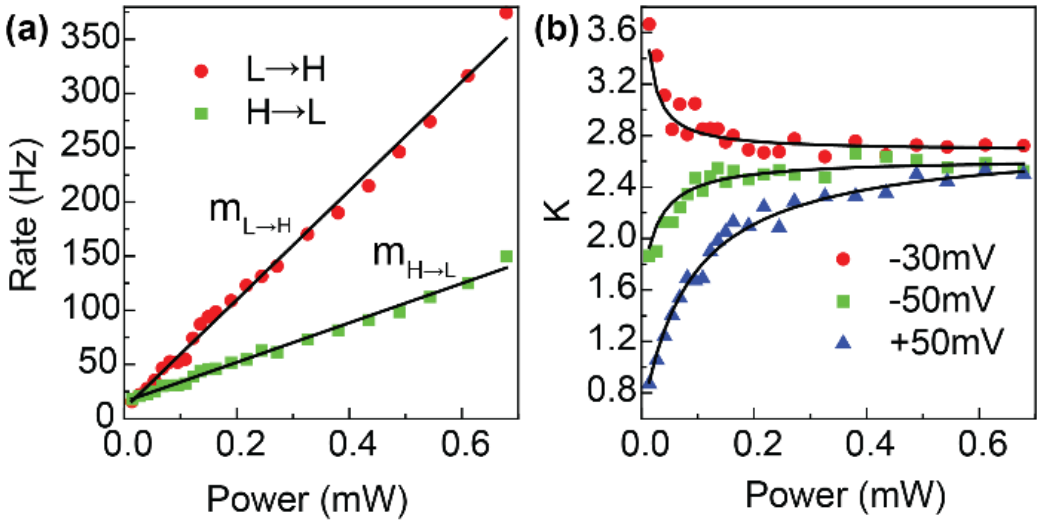

3.4 Results and Discussion

As shown in Figure 3.3a and b, photon transition yields $Y_{L\rightarrow H}$, $Y_{H\rightarrow L}$ and photon equilibrium K_S of a single pyrrolidine on Cu(001) is measured as a function of laser wavelength range 725 ~985 nm, the alignment is optimized at each wavelength by maximizing the light induced transition rate. A broad baseline feature can be observed in the photon transition yields for transitions in both directions, with $Y_{L\rightarrow H}$ being approximately 4 times the values of $Y_{H\rightarrow L}$. The broad baseline shape matches well with the simulated LSP mode for silver tip on Cu(111) reported by Kazuma et. al.[11], which has a leading peak around 670 nm and local minimum around 880 nm. Therefore, we attribute the baseline feature to be the cumulative excitation of all vibrational modes within the energy distribution of LSP generated hot electrons, which spans the gap from the substrate Fermi level up to the LSP energy. With this excitation mechanism, the photon transition yield is dominated by the LSP excitation efficiency at different incident photon energies. On the other hand, for the K_s spectra, we observe an overall flat baseline with a significant dip-peak feature near 915 nm, where photon transition yields only exhibit a very weak and broad feature. This equilibrium shift is attributed to the resonant excitation of the C-H stretch third overtone (as compared to liquid phase absorption spectra shown in Figure 3.3c) with the LSP nearfield at tunneling junction. This dip-peak feature can be explained by the mode softening of proximally located C-H groups at L state due to their interaction with the metal substrate. A larger cross section for C-H stretch excitation at H state leads to a H to L equilibrium shift near 915 nm, and the C-H stretch excitation of the 2 proximal C-H bonds at L state leads to a L to H equilibrium shift at the red-shifted wavelength. Different line shapes for photon transition yield and K_S spectra provide strong evidence that the latter is insensitive to influence of LSP and makes a good indicator for mode-selective reaction equilibrium control with tunable wavelength.

Figure 3.3 Wavelength dependence of pyrrolidine conformational transition in the 725~985 nm range. (a) Photon yield is plotted as a function of wavelength for L → H and H → L transition respectively. For each wavelength, current traces are measured at different laser power values (including zero power), and transition yield is computed. Three data sets are displayed with each set repeated with manually optimized laser alignment at each wavelength. All three data sets were measured at +30 mV bias with feedback off at state H with set point +30 mV, 0.1 nA. (b) Computed K_S for all three data sets shown in (a). Error bars indicate propagated uncertainty from standard error of reaction rate measurement. (c) NIR absorption spectra obtained with bulk liquid sample of pyrrolidine.

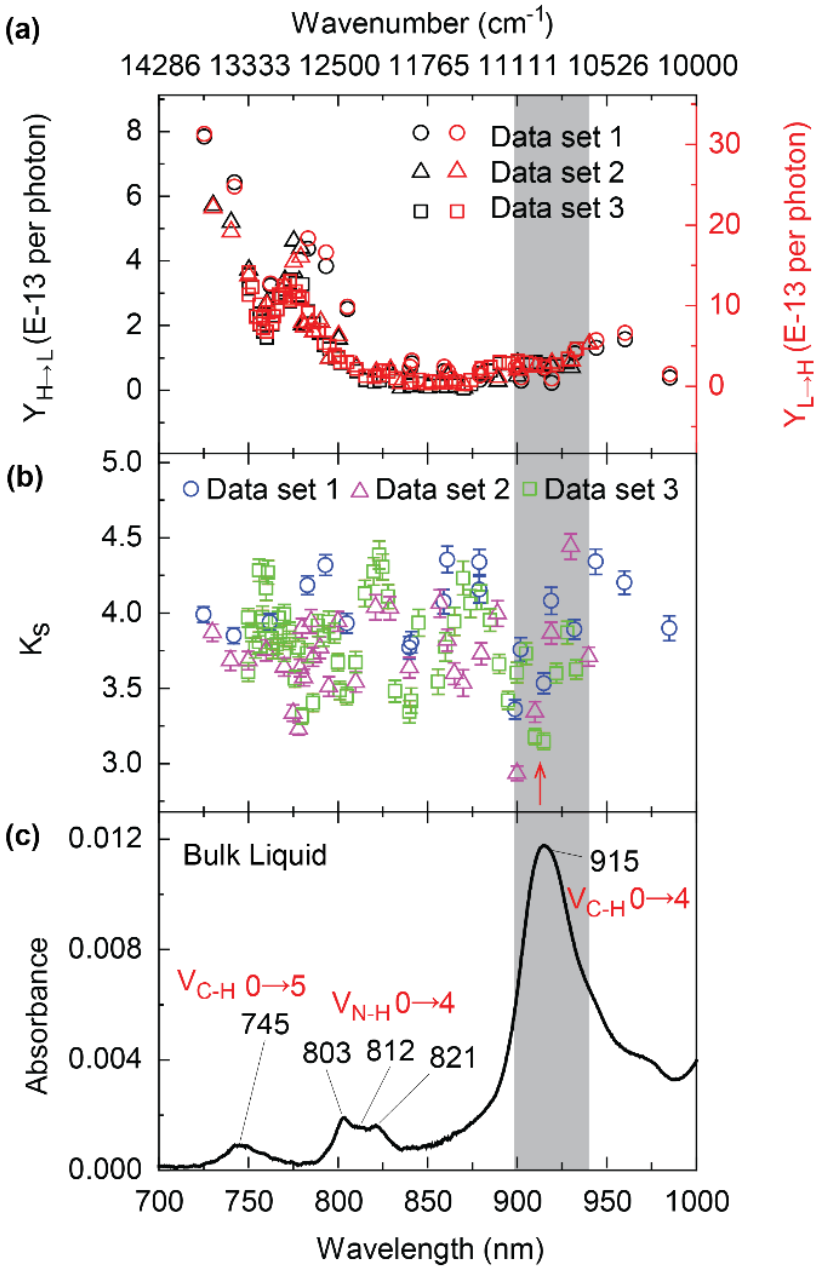
(a)
Wavenumber (cm-1)
14286 13333 12500 11765 11111 10526 10000
Data set 1
Data set 2
Data set 3
YH→L (E-13 per photon)
YL→H (E-13 per photon)
(b)
Data set 1 Data set 2 Data set 3
KS
(c)
Bulk Liquid
915
VC-H 0→4
VC-H 0→5
VN-H 0→4
745
803 812 821
Absorbance
Wavelength (nm)

To confirm the effectiveness of PEAS, we further use a set of fiber coupled tunable diode lasers to perform the same measurements with finer frequency steps (< 50 GHz) over the range of 1544 to 1554 nm, which falls right on one of the N-H stretch first overtone peaks (Figure 3.4c). To simplify data taking process, we measure the transition rates with light off and with light on at a fixed power for each wavelength and compute the photon transition yield based on the two-point data sets. Despite the strong fluctuation in photon transition yields (see Figure 3.4a), which in this case is dominated by the power variation at different wavelength due to transmission loss of the optical fiber setup, we can observe a very different line shape in the K_S spectra. The K_S spectra resolve 2 peaks on a broad baseline with fitted FWHM to be of 0.48 meV and 0.82 meV respectively (Figure 3.4b). These 2 peaks are possibly related to rotational-vibrational excitation of pyrrolidine due to its low energy barrier to rotate around the adsorption site [12], with peaks at 1545.8 nm and 1550.4 nm corresponding to the H state and L state rotational excitation respectively. The bigger FWHM value for the 1550.4 nm peak can be the interpreted as a smaller coherence time due to a stronger interaction between the molecule and the metal substrate at L state. On the other hand, K_S spectra baseline shown in Figure 3.4b exhibits a "U" shape, which is close to the inversed profile of the liquid phase absorption spectra. Based on the ab-initio calculation done by El-Gogary and Soliman[9], N-H bond has a strong force interaction with the two neighboring C-N bonds, and the C-N stretching makes a leading component in the potential energy distribution of the ring breathing mode. Combining information from the electron action spectra (see Supporting Information 3.6.3) where ring breathing mode is highly in favor of H → L transitions, we can infer a possible equilibrium shift towards the L state associated with the photoexcitation of N-H stretch mode and its overtones. This inference provides potential

explanation to the shape of baseline observed in K_S spectra. Nonetheless, to make conclusive statements regarding the peaks and line shape, K_S spectra of a wider wavelength range are needed. We also compared K_S spectra measured at 3 different sample biases (Figure 3.5a) to show that all three K_S spectra measurements are consistent both in values and overall line shapes, which experimentally confirms K_S spectra to be independent of sample bias. With a different tip, we also compare the K_S spectra at sample bias -50 mV for an isolated pyrrolidine, a pyrrolidine adsorbed next to a CO molecule, and a pyrrolidine adsorbed next to a step edge (Figure 3.5c). K_S spectra of the latter two display offsets of approximately -0.1 and -0.2 with respect to the isolated pyrrolidine, indicating a shift towards L state due to the change of local environment. This can be interpreted as the result of a gentle modification to the potential well model (Figure 3.5b) due to local surface potential change induced by nearby CO adsorption and step edge. Small redshifts in both peaks can be resolved from the gaussian fitting, which indicate change in rotational energy due to the influence of local environment. Again, the above reasoning is based on the assumption that both peaks are rotational features, which requires K_S spectra of a broader wavelength range and rigorous calculation to confirm. However, such small peak shift induced by local environment variation indeed demonstrates a promising application of PEAS for single molecule vibrational sensing with sub-meV energy resolution.

Figure 3.4 Wavelength dependence of single pyrrolidine conformational transition in the 1544 ~ 1554 nm range. (a) Photon yield as a function of wavelength for L → H and H → L transition respectively with laser illumination at 0.68 mW nominal power. Current traces are recorded at -50 mV bias with tip feedback off at set point -500mV, 1 nA. (b) Corresponding K_S spectra computed from photon yield. Error bars indicate propagated uncertainty from standard errors of transition rate measurement. The red curve is the cumulative fitting results of two Lorentzian peaks (green and magenta curves, offset by 2.2 for easy comparison to measured data) and a broad baseline (blue curve). (c) NIR absorption spectra obtained with bulk liquid sample of pyrrolidine. The measured wavelength range in (a) and (b) is located at one of the N-H stretch $v = 0 \rightarrow 2$ overtone peaks.

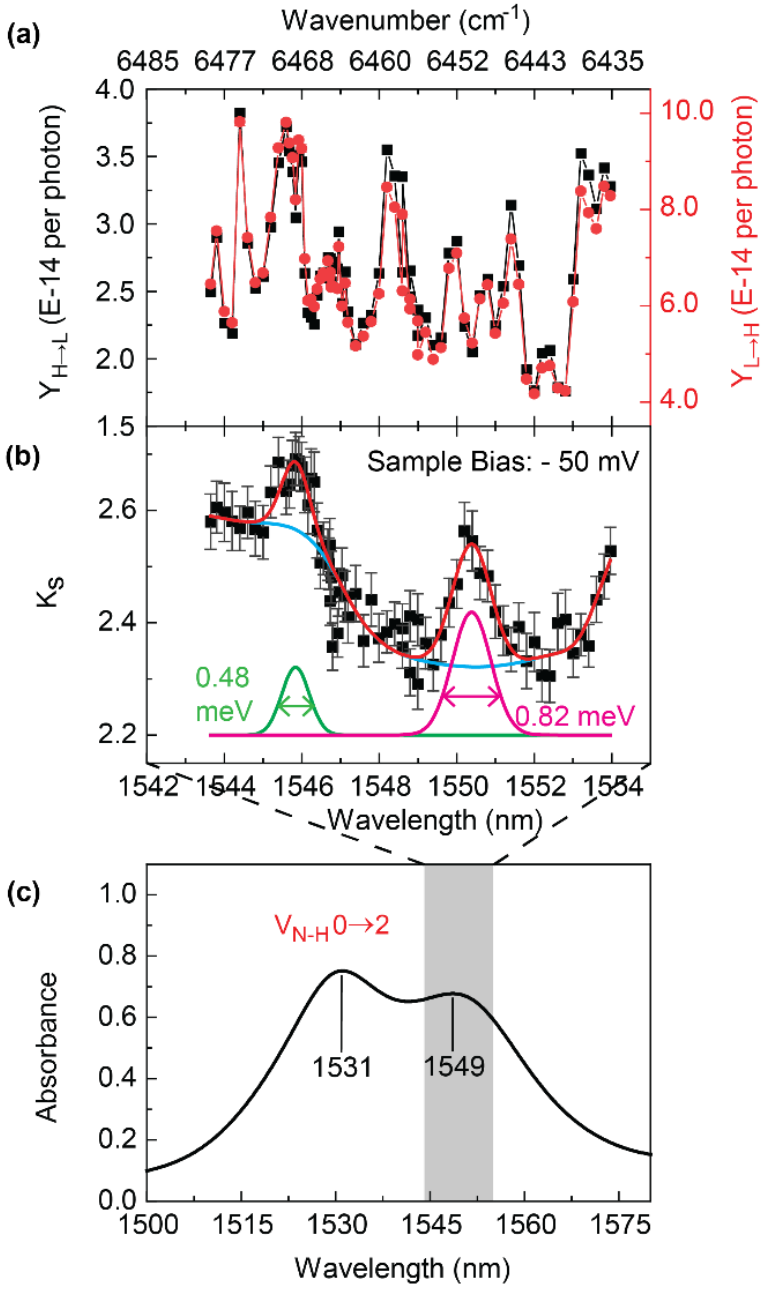
(a)
Wavenumber (cm-1)
6485 6477 6468 6460 6452 6443 6435
4.0
3.5
3.0
2.5
2.0
1.5
10.0
8.0
6.0
4.0
Y H→L (E-14 per photon)
Y L→H (E-14 per photon)
(b)
Sample Bias: - 50 mV
2.6
2.4
2.2
Ks
0.48
meV
0.82 meV
1542 1544 1546 1548 1550 1552 1554
Wavelength (nm)
(c)
1.0
0.8
0.6
0.4
0.2
0.0
Absorbance
V N-H 0→2
1531
1549
1500 1515 1530 1545 1560 1575
Wavelength (nm)

Figure 3.5 Comparison of saturated reaction equilibrium constant K_s for different bias and molecule local environment, in the range of 1544 ~1554 nm. (a) $K_s(\nu)$ measured with sample bias at -30 mV,-50 mV and +50 mV respectively with 0.68 mW nominal laser power. 3-point adjacent averaging for the averaged data of all three biases are displayed as black curve to guide the view. (b) K_s as a function of wavelength for an isolated pyrrolidine, a pyrrolidine adsorbed next to a carbon monoxide, and a pyrrolidine adsorbed next to a step edge, probed with tip position indicated in (c) - (e) respectively. Current traces are measured at -50 mV with 0.68 mW nominal laser power. Black curves in (b) is fitted curve as the sum of two gaussian peaks and a baseline. The black and blue dotted lines indicate the peak positions measured for an isolated pyrrolidine. All current traces are measured with feedback off at set point -500 mV, 1 nA. (c)-(e) display the topographies (top) of pyrrolidines with different local environment and the corresponding double well potential schematic diagrams (bottom) that qualitatively describe each pyrrolidine 2-level system.

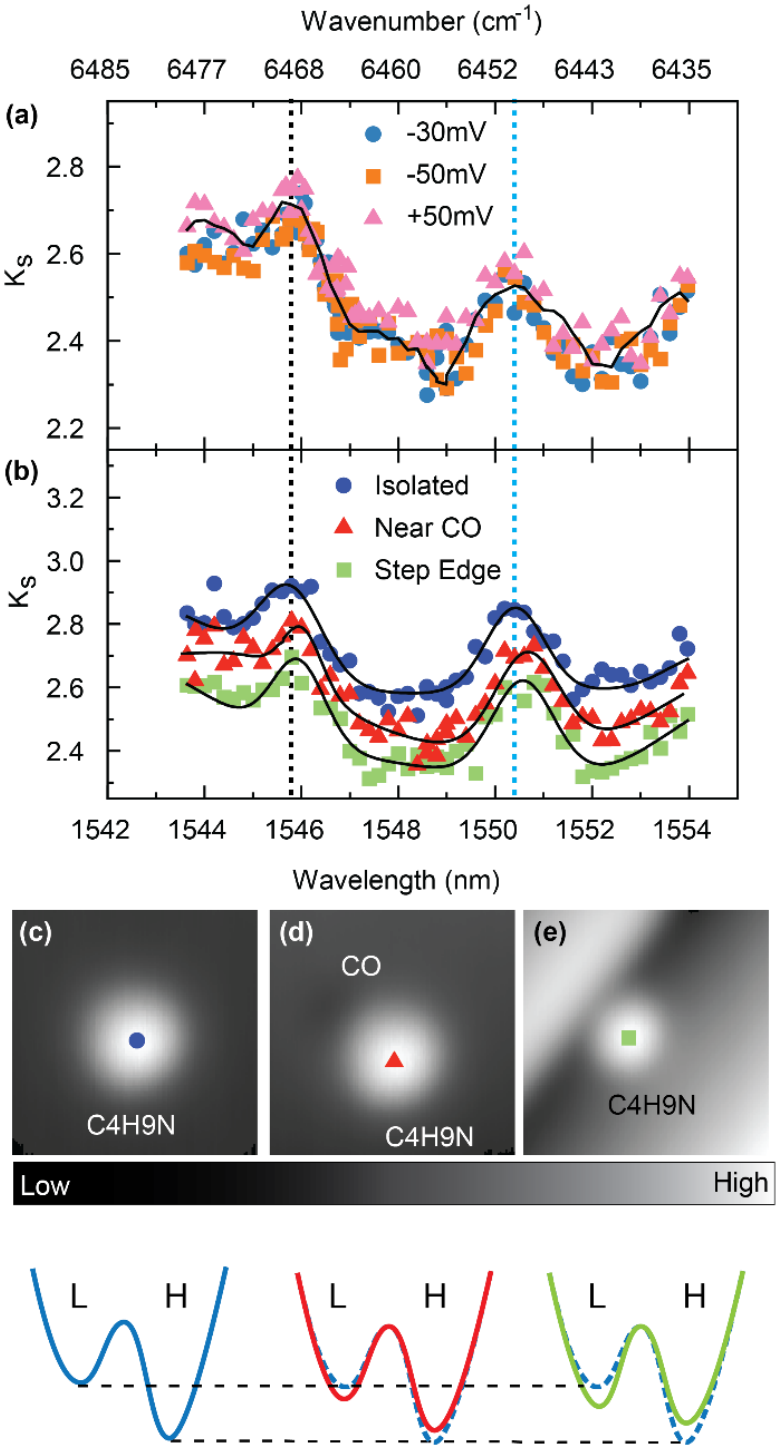
Wavenumber (cm-1)
6485
6477
6468
6460
6452
6443
6435
(a)
-30mV
-50mV
+50mV
Ks
2.8
2.6
2.4
2.2
(b)
Isolated
Near CO
Step Edge
3.2
3.0
2.8
2.6
2.4
1542
1544
1546
1548
1550
1552
1554
Wavelength (nm)
(c)
C4H9N
(d)
CO
C4H9N
(e)
C4H9N
Low
High
L
H
L
H
L
H

3.5 Conclusion

In summary, we have successfully demonstrated PEAS in detection of vibrational overtone photoexcitation in a single pyrrolidine molecule with sub-meV energy resolution. With PEAS , we can probe purely photon-induced equilibrium shift with great robustness against any frequency-dependent electric field variation at junction, either caused by LSP mode or optical transmission. This technique provides a new prospective for mode-selective photocatalysis in product concentration control of reversible chemical reactions. Moreover, the observation of possible rotational-vibrational excitation and the local environment sensitivity of such measurement also demonstrate the superior energy resolution of this novel single molecule optical spectroscopy technique.

3.6 Supporting Information

3.6.1 Optical Setup For Two Types of Laser Sources

For measurement from 725 ~ 985 nm, a tunable Ti-Sapphire laser (Spectra Physics MaiTai eHP DeepSee) is used at pulsed continuous-wave mode, with a bandwidth around 3 nm (Figure 3.6a). Laser power is stabilized and controlled by a laser power controller first and then fine-tuned by a set of linear polarizers. The transmitted light is then aligned and focused to STM junction with a pair of mirrors and a 4-inch focal length Tsurupica lens (BroadBand Inc.). Laser power is measured with a silicon diode power meter (Thorlabs S120VC) after the second polarizer and used as nominal laser power for experimental measurement.

For measurement from 1544 ~ 1554 nm, a set of DFB lasers (Toptica TeraScan1550) are used (Figure 3.6b). Each laser covers roughly half of the wavelength tuning range, and they together provide a tuning range of 2580 GHz with less than 10 MHz frequency linewidth. Light emission from both laser heads is coupled into a 2×2 50:50 optical fiber mixer (Toptica TeraScan1550) to maintain consistent optical setup when switching between the 2 lasers. Light out of one output port of the 50:50 mixer is then fed to an Electrical Variable Optical Attenuator (EVOA, Thorlabs V1550PA) for power regulation and the output light is further split with a 25:75 fiber splitter (Thorlabs PNH1550R3A1). The 25% portion is measured by an InGaAs photodiode (Thorlabs DET08CFC) and photocurrent is used as real-time feedback for a home-made PID power regulation box, which in turn controls the EVOA to reach target output power. The 75% portion is coupled to a fiber collimator (Thorlabs F260APC-1550) through another fiber patch cable (Thorlabs P3-1550PMP-2). A 4-inch focal length Tsurupica lens (BroadBand Inc.) is used to

eventually focus the collimated beam into the STM junction. The power measured by the InGaAs photodiode is multiplied by 3 and used as nominal laser power for experimental measurements. In both setups, we adjust laser beam to p-polarization to maximize the electric field component along the tip axis.

Figure 3.6 Detailed experimental setup for different types of laser sources. (a) Optical setup for a free space laser source. (b) Optical setup for a pair of fiber-coupled DFB lasers.

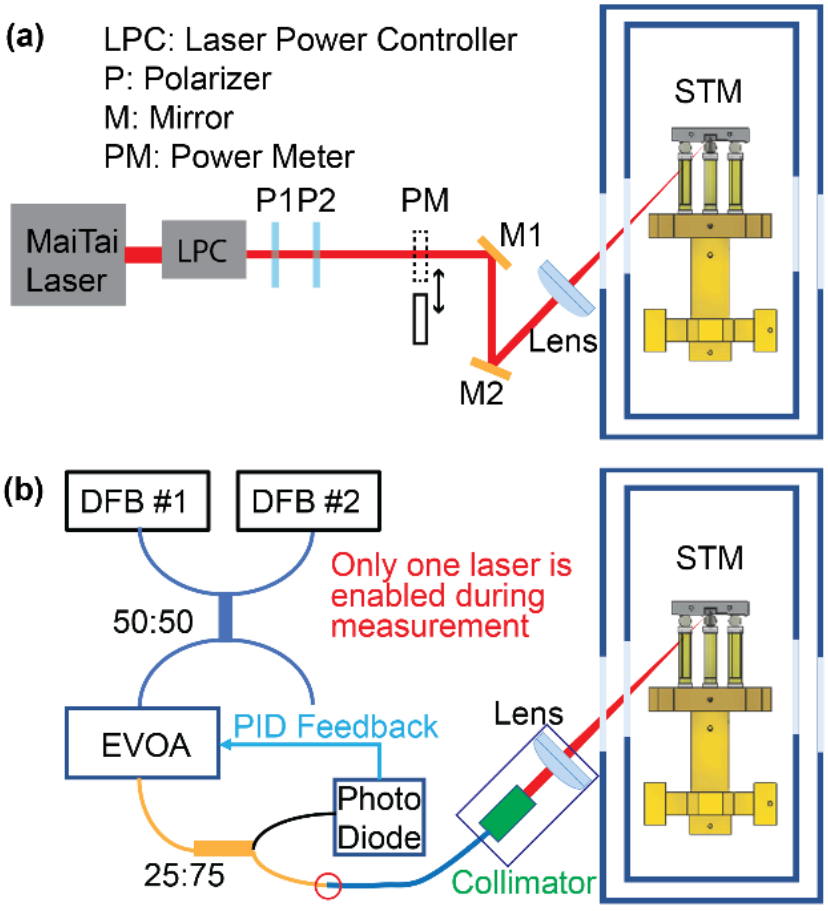

3.6.2 Alignment of 1550 nm Laser Beam to Junction

To align laser beam around 1550 nm to junction, instead of using an InGaAs camera to image the exiting beam, we use a 635 nm diode laser for pre-alignment. As shown in Figure 3.7, the 635 nm laser beam is first dimmed by a ND filter and then coupled to a fiber port (Thorlabs PAF2A-11B). In the optical setup shown in Figure 3.6b, disconnect the fiber patch cable from the position indicated by the red circle, and connect it to the fiber port as indicated by the red circle in Figure 3.7. The 635 nm laser beam will transmit to the STM junction and exit to form image at the CMOS camera. Guided by the camera view, 635 nm beam can be aligned to tip apex. We then switch back to the regular setup in Figure 3.6b and further optimize the 1550 nm laser alignment by maximizing the conformational transition rate of a pyrrolidine molecule. Since the fiber patch cable and collimator are both designed for 1550 nm light, the transmitted 635nm beam shape is not ideal (see inset of Figure 3.7). However, with this method, we can reproduce the optical alignment with 1550nm light after the fiber collimator with minimum discrepancy by avoiding any movement of the fiber collimator and focusing lens.

Figure 3.7 Optical setup for pre-alignment with 635 nm diode laser. Inset shows the camera view with light beam aligned to STM junction.

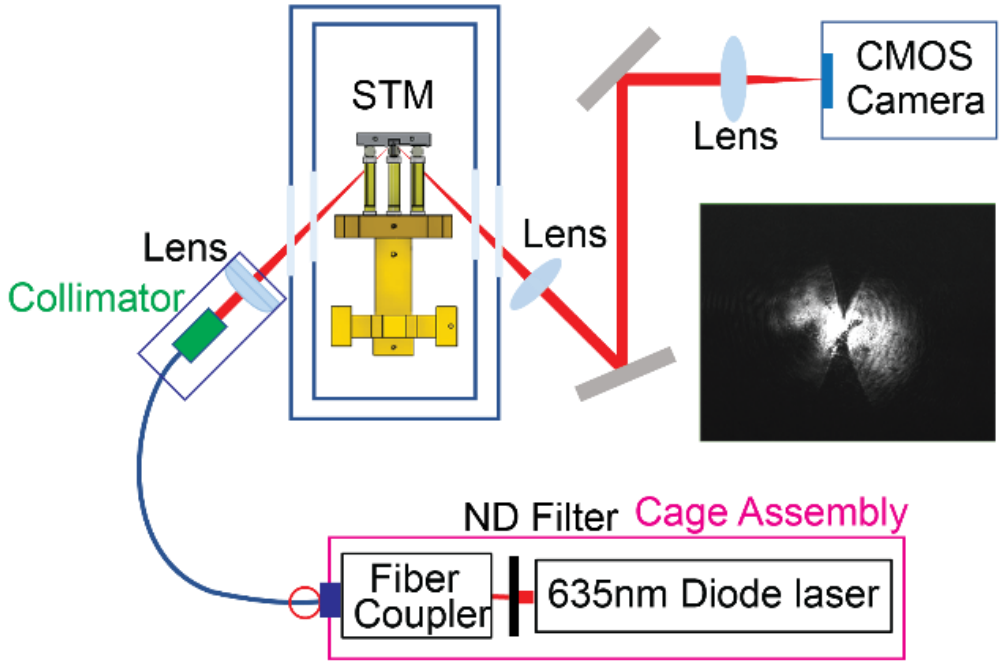

3.6.3 Electron Action Spectra of Pyrrolidine Reversible Conformational Transition

To better understand the role played by tunneling electrons in the reversible transition of pyrrolidine, we measured the transition rate as a function of sample bias without light illumination (Figure 3.8a). It is interesting to see that, H → L and L → H transitions are driven by different vibrational modes through inelastic tunneling process[13–17]. $R_{L\to H}$ and $R_{H\to L}$ are fitted to the equation below (see details in reference [18]):

$$R_{dark}(V) = \sum_i k_i I_{IET,i}(V) + \text{const.}$$

The first term represents the sum of vibration-induced transition rates that's proportional to the inelastic tunneling current $I_{IET,i}(V)$ of vibrational mode i. The small constant offset accounts for an intrinsic transition that occurs without any vibrational excitation.

From the fitting results we can resolve the dominating modes for H → L transitions at 47.2 meV, 109.4 meV, 160.6 meV and 365.12 meV, which can be assigned to out-of-plane ring, ring breathing, H-N-C wagging and C-H stretch modes respectively. And for L → H transitions, dominating modes at 79.8 meV, 160.6 meV and 358.36 meV are resolved, corresponding to in-plane ring, H-N-C wagging and C-H stretch mode. Comparing the transition rates to the computed the reaction equilibrium constant K from $\frac{R_{L\to H}}{R_{H\to L}}$ (displayed in Figure 3.8b), we can obtain the following two insights: A. Excitation of certain vibrational modes is favored in one conformational state over the other. B. The dominating vibrational excitation at one conformational state will shift transition equilibrium towards the other state. For example, excitation of out-of-plane ring mode and ring breathing mode is favored for H state conformation, which greatly facilitated H → L transitions at bias near 47.2 meV and 109.4 meV, leading to an equilibrium shift towards the L state; similarly, excitation of in-plane ring mode at 79.8 meV is favored for L → H transitions and

leads to a dramatic equilibrium shift towards the H state. On the other hand, transitions in both directions are facilitated with similar intensity at 160.6 meV due to H-N-C wagging mode excitation. As this mode is barely affected by the conformation state, no significant change in equilibrium is induced by this mode. For the C-H stretch mode, the fitting results indicate a lower excitation energy for L state than high state, this can be attributed to the mode softening of the C-H bonds closer to copper substrate, a similar effect was observed by Patel et. al. for pyrrolidine on Cu(110) substrate[19]. The mode softening results in bigger cross section of C-H stretch excitation for state H and shifted the equilibrium slightly towards state L. At bias +500 mV and -500 mV, the cumulative vibration excitation of all lower energy modes has resulted in an equilibrium constant of 1.8 and 0.9 respectively, this difference is potentially cause by molecule structural difference due to opposite electric field orientation.

Figure 3.8 Action spectra for reversible conformational transition of pyrrolidine. (a) The transition rates of L → H and H → L ($R_{L\rightarrow H}$, $R_{H\rightarrow L}$) as a function of sample bias from -500 mV to +500 mV. Fitted results are displayed in black curves. Data are measured with constant height probing at set point -500 mV, 1 nA, without light illumination. For sample bias in the range -80 ~ +80 mV, transition rates are measured from current traces as described in Experimental Methods. For sample bias beyond the range -80 ~ +80 mV, due to limited bandwidth of current pre-amplifier, transition rates are measured using a different method discussed in detail by Jiang in ref[18]. (b) Corresponding reaction equilibrium constant K, defined as $R_{L\rightarrow H}$ / $R_{H\rightarrow L}$, is plotted as a function of sample bias. Black curve is calculated from the fitted curve in (a). Increase in K indicates a shift of transition equilibrium towards state H, vice versa.

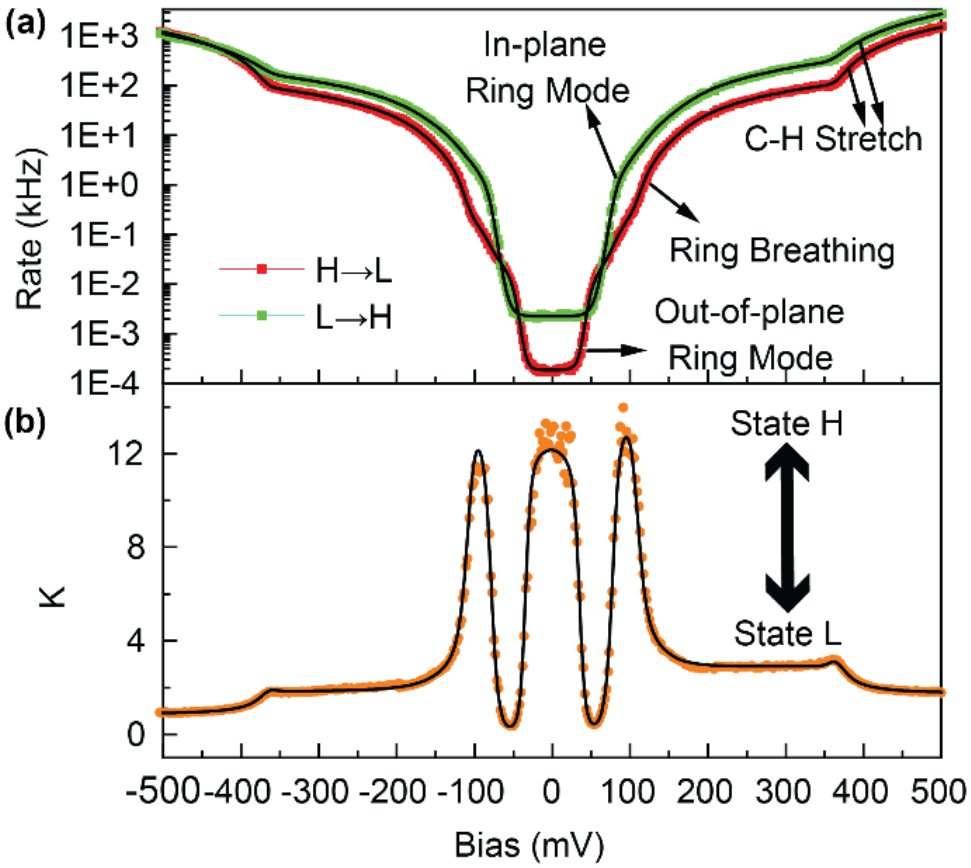
(a)
1E+3
1E+2
1E+1
1E+0
1E-1
1E-2
1E-3
1E-4
Rate (kHz)
In-plane
Ring Mode
C-H Stretch
Ring Breathing
H→L
L→H
Out-of-plane
Ring Mode
(b)
12
8
4
0
K
State H
State L
-500 -400 -300 -200 -100 0 100 200 300 400 500
Bias (mV)

3.6.4 Statistical Error Analysis of Transition Rate, Photon Yield and Photon Equilibrium Constant

In the conformational transitions of pyrrolidine, state L to H and H to L transitions are viewed as 2 independent Poisson processes. For a Poisson process that takes a transition as an event, the probability for no event occurring within a time interval τ can be written as:

$$P(n = 0, t \leq \tau) = e^{-r\tau}$$

Here, r is the average transition rate. Therefore, the probability for a transition to occur between τ and $\tau + \Delta t$ is:

$$P(\tau, \Delta t) = P(n = 0, t \leq \tau) - P(n = 0, t \leq \tau + \Delta t) = (1 - e^{-r\Delta t})e^{-r\tau}$$

This probability is still an exponential decay with the same decay rate constant r. The histograms of experimentally measured state residence times of state L and H are plotted in Figure 3.9, both fitted well to an exponential decay yielding transition rates $R_{L\rightarrow H} = 12.5\text{Hz}$ and $R_{H\rightarrow L} = 6.7\text{Hz}$. With $\Delta t \rightarrow 0$, we get the probability mass function for a state residence τ being:

$$P(\tau) = \frac{1}{r}e^{-r\tau}$$

This would yield an expectation and variance for rate constant R:

$$E(R) = \text{Var}(R) = r$$

Experimentally we take the inverse of mean state residence time as the transition rate constant

$$R_{H\rightarrow L\ (L\rightarrow H)} = \frac{1}{T_{H(L)}}$$

The standard error of the transition rate constant measurement is therefore written as:

$$\delta R_{H\rightarrow L\ (L\rightarrow H)} = \sqrt{\frac{R_{H\rightarrow L\ (L\rightarrow H)}}{\sum t_{H(L)}}}$$

Now suppose we use N pairs of power dependent transition rate measurements to compute the light-induced rate constant k (which is the slope of the linear regression between rate and power) and consider only the statistical error from transition rate measurement, we can model the experimental measurements as below:

$$p_i = p_i^*$$

$$R_i = R_i^* \pm \delta R_i$$

p_i, R_i represent the measurement values laser power and transition rates, and p_i^*, R_i^* represent the true values, δR_i being the standard error for R_i.

The linear regression estimate for slope (rate constant) k from true values is:

$$\hat{m} = \frac{\mathrm{Cov}(p, R^*)}{\mathrm{Var}(p)} = \frac{\mathrm{Cov}(p, R \pm \delta R)}{\mathrm{Var}(p)}$$

whereas the estimate of k from measurement values is:

$$\bar{m} = \frac{\mathrm{Cov}(p, R)}{\mathrm{Var}(p)}$$

Therefore, the relative error of estimated photon efficiency $\bar{m}$ is:

$$\beta = \frac{|\bar{m} - \hat{m}|}{\hat{m}} = \left|\frac{\mathrm{Cov}(p, \delta R)}{\mathrm{Cov}(p, R)}\right|$$

The propagated uncertainties for photon yield Y and saturated reaction equilibrium constant are written as follow:

$$\delta Y = \delta\left(\frac{m}{E_{photon}}\right) = Y * \beta$$

$$\delta K_s = \delta\left(\frac{m_{L\to H}}{m_{H\to L}}\right) = K_s\sqrt{\beta_{L\to H}^2 + \beta_{H\to L}^2}$$

Figure 3.9 Histogram of residence times at state L and H (t_L and t_H) extracted from current trace of 100s in total and displayed in (a) and (b) respectively. Current trace is measured at +50 mV bias with feedback off at set point -500 mV, 1 nA, without light illumination. The red lines are exponential fit of events as a function of t_L or t_H, which yield transition rates of 12.5 Hz and 6.7 Hz respectively.

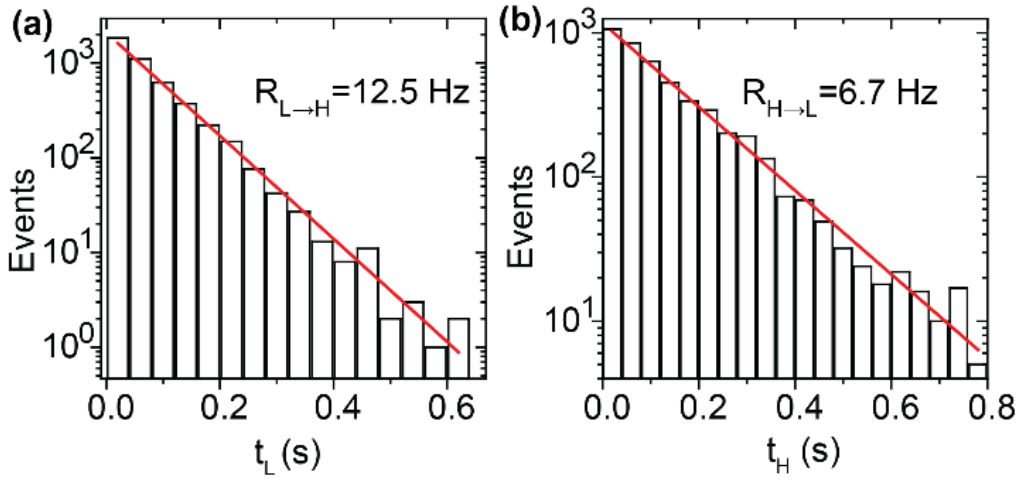

Bibliography

[1] S. Li, G. Czap, H. Wang, L. Wang, S. Chen, A. Yu, R. Wu, and W. Ho, Physical Review Letters, **122**, 077401 (2019).

[2] F.F. Crim, Journal of Physical Chemistry, **100**, 12725–12734 (1996).

[3] S. Mahapatra, J.F. Schultz, L. Li, X. Zhang, and N. Jiang, J Am Chem Soc, **144**, 2051–2055 (2022).

[4] H. Böckmann, M. Müller, A. Hammud, M.G. Willinger, M. Pszona, J. Waluk, M. Wolf, and T. Kumagai, Journal of Physical Chemistry Letters, **10**, 2068–2074 (2019).

[5] E. Kazuma, J. Jung, H. Ueba, M. Trenary, and Y. Kim, Science, **360**, 521–526 (2018).

[6] M.J. Comstock, N. Levy, A. Kirakosian, J. Cho, F. Lauterwasser, J.H. Harvey, D.A. Strubbe, J.M.J. Fréchet, D. Trauner, S.G. Louie, and M.F. Crommie, Physical Review Letters, **99**, 038301 (2007).

[7] M.J. Comstock, N. Levy, J. Cho, L. Berbil-Bautista, M.F. Crommie, D.A. Poulsen, and J.M.J. Fŕchet, Applied Physics Letters, **92**, 123107 (2008).

[8] M. Bazarnik, L. Jurczyszyn, R. Czajka, and K. Morgenstern, Physical Chemistry Chemical Physics, **17**, 5366–5371 (2015).

[9] T.M. El-Gogary, Spectrochimica Acta - Part A: Molecular and Biomolecular Spectroscopy, **57**, 1405–1415 (2001).

[10] J. Yao, Y. Park, and W. Ho, In Preparation.

[11] E. Kazuma, J. Jung, H. Ueba, M. Trenary, and Y. Kim, Science, **360**, 521–526 (2018).

[12] S. Li, S. Chen, J. Li, R. Wu, and W. Ho, Physical Review Letters, **119**, 176002 (2017).

[13] Y. Kim, K. Motobayashi, T. Frederiksen, H. Ueba, and M. Kawai, Progress in Surface Science, **90**, 85–143 (2015).

[14] K. Motobayashi, Y. Kim, H. Ueba, and M. Kawai, Physical Review Letters, **105**, 076101 (2010).

[15] Y. Sainoo, Y. Kim, T. Okawa, T. Komeda, H. Shigekawa, and M. Kawai, Physical Review Letters, **95**, 246102 (2005).

[16] J. Oh, H. Lim, R. Arafune, J. Jung, M. Kawai, and Y. Kim, Physical Review Letters, **116** (5), 056101 (2016).

[17] W. Ho, Accounts of Chemical Research, **31**, 567–573 (1998).

[18] J. Yao, S. Chen, W. Shi, and W. Ho, In Preparation.

[19] C.J. Patel, Investigating Single Molecule Physics with the Scanning Tunneling Microscope, Ph.D. Dissertation, University of California, Irvine, 2017.

Chapter 4

Line Shape Study for Pyrrolidine Optical Rectification Spectra

4.1 Abstract

The photo-switching behavior of a surface-adsorbed pyrrolidine molecule makes it a good photo-rectifier at a tunneling junction. Photocurrent generated at from a single pyrrolidine molecule can be measured by Optical rectification spectroscopy (ORS). Here we demonstrate the line shape and signal intensity variation in ORS of a single pyrrolidine molecule observed at different tunneling gaps and different laser powers with 1548 nm illumination. We simulate ORS with line shapes highly consistent with the experimental measurements by employing a two-level system model and an assumption of bias-independent photo-switching rate. The results indicate that the competition between photon-induced conformational transitions and electron-induced transitions can be engineered through multiple factors and leads to effective tuning of the photocurrent generated from a single molecule.

4.2 Introduction and Theoretical Background

Single molecule electronics and devices [1–3] are important building blocks for the next-generation integrated circuits. Molecular photo-switches are in particular of interest to researchers due to their potential application as photo mixers and phototransistor in digital circuit[4–10]. For molecules that undergo fast conductance switching under photo-illumination, it is even possible to build single molecule photo-conductive devices that generates radio frequency or even terahertz radiation. A recent study by Yao et al.[11] demonstrated the optical rectification spectroscopy in measuring photocurrent induced in a single pyrrolidine molecule. The photocurrent was shown to be bias dependent and exhibit a setpoint dependence and laser power dependence as well. In this paper, we discuss in detail the setpoint and power dependence in the experimental ORS line shapes of a pyrrolidine molecule adsorbed on Cu (001) surface, providing a deeper understanding of the nature of ORS line shapes through numerical simulations based on theoretical models.

As discussed in Chapter 3, for a pyrrolidine adsorbed on a 8-K Cu(001) substrate under laser illumination, its conformational transition rates in both directions are controlled jointly by the sample bias V, laser illumination frequency ν and power p, which can be written as:

$$R_{L\to H(H\to L)}(V,\nu,p) = R_{L\to H(H\to L),dark}(V) + m_{L\to H(H\to L)}(\nu)\times p \tag{4.1}$$

Here $m_{L\to H(H\to L)}(\nu)$ is the photon rate coefficient, which is unique to each laser frequency ν. The dark rate $R_{dark}(V)$ is written as [12]:

$$R_{L\to H(H\to L),dark}(V) = \sum_{i(j)} k_{i(j)} I_{IET,i(j)}(V) + C_{L\to H(H\to L)} \tag{4.2}$$

Where $I_{IET,i}(V)$ is the inelastic tunneling current from excitation of vibrational mode i, and k_i represents the conversion efficiency between the vibrational excitation of mode i and the conformational transition reaction.

Considering a simple two-level system[13] where population is conserved, the equilibrium state populations of a single pyrrolidine molecule are determined by $R_{L\to H}$ and $R_{L\to H}$ simultaneously:

$$\begin{cases} n_{H,eq}(V) = \dfrac{R_{L\to H}(V)}{R_{L\to H}(V) + R_{H\to L}(V)} \\ n_{L,eq}(V) = 1 - n_{H,eq}(V) \end{cases} \tag{4.3}$$

Where $n_H, n_L, R_{L\to H}$ and $R_{H\to L}$ are the high-state population, low state population, low-to-high transition rate and high-to-low transition rate respectively.

For an immediate change in $R_{L\to H}(V)$ or $R_{H\to L}(V)$ at time $t = 0$, the successive time evolution of high-state population is described by an exponential transition [11,13,14] from its initial population $n_{H0}(V)$ to the new equilibrium population $n_H{}'(V)$ controlled by the new transition rates $R'_{L\to H}(V)$ and $R'_{H\to L}(V)$:

$$\begin{cases} n_H(V,t) = \left(n_{H0}(V) - n_{H,eq}{}'(V)\right) e^{-[R'_{L\to H}(V) + R'_{H\to L}(V)]t} + n_{H,eq}{}'(V) \\ n_L(V,t) = 1 - n_H(V,t) \\ n_{H,eq}{}'(V) = \dfrac{R'_{L\to H}(V)}{R'_{L\to H}(V) + R'_{H\to L}(V)} \end{cases} \tag{4.4}$$

The exponential decay rate equals the total rate of conformational transitions. Therefore, change in $R_{L\to H}$ and $R_{L\to H}$ will in general lead to a change in the state population, hence a change in the total tunneling current, which can be modelled as a population-weighted average between 2 conformational states[15]:

$$I_{total}(V,t) = n_H(V,t)\sigma_H V + n_L(V,t)\sigma_L V \tag{4.5}$$

Where σ_H and σ_L are the high-state and low-state conductance respectively and assumed to be constant as a function of sample bias. This model has been used to explain the vibrationally mediated negative differential resistance (NDR) observed for pyrrolidine and pyrrolidine-d8 [15]. For ORS, there are two types of measurements we can perform: static ORS, which is the I-V curve subtraction between the bright condition (laser on) and dark condition (laser off), and dynamic ORS, which is obtained by illuminating the molecule junction with a chopped laser beam and acquiring the first harmonic signal from tunneling current. The static ORS has shown to be quite different from the dynamic ORS in line shapes, especially in the low bias region[11]. The reason for such line shape difference originates from the chopping method used by the dynamic ORS measurement.

For static ORS, we can interpret the signal as the total change in equilibrium tunneling current due to light-induced population shift. Combining Equation (4.3) and (4.5), we can write static ORS signal as:

$$I_{\text{static ORS}}(V) = I_{\text{Bright,eq}}(V) - I_{\text{Dark,eq}}(V) = \Delta n_{\text{H,eq}}(V) \times \Delta\sigma \times V \tag{4.6}$$

Where

$$\Delta n_H(V) = n_{\text{H,eq}}^{\text{Bright}}(V) - n_{\text{H,eq}}^{\text{Dark}}(V) \tag{4.7}$$

$$\Delta\sigma = \sigma_H - \sigma_L \tag{4.8}$$

$I_{\text{Bright,eq}}(V)$ and $I_{\text{Dark,eq}}(V)$ are equilibrium tunneling current at bright and dark condition. $n_{\text{H,eq}}^{\text{Bright}}(V)$, $n_{\text{H,eq}}^{\text{Dark}}(V)$ are equilibrium high-state population at bright and dark condition respectively, and σ_H, σ_L are high and low state conductance.

For dynamic ORS measurement, the pyrrolidine molecule is under periodic change in light-induced transition rate, therefore its high-state population is expected to alternate between the

bright and dark equilibrium population within each chopping cycle as described by Equations (4.4), resulting in a periodic oscillation in the tunneling current. The dynamic ORS signal is then obtained by extracting first harmonic component of the tunneling current. Mathematically in-phase and out-of-phase components are computed by the equations below:

$$I_{\text{dynamic ORS}}(V) = \begin{cases} f\int_0^{\frac{1}{f}} I_{\text{total}}(V,t)\sin(2\pi ft+\theta_0)\,dt, & \text{In phase} \\ f\int_0^{\frac{1}{f}} I_{\text{total}}(V,t)\cos(2\pi ft+\theta_0)\,dt, & \text{Out of phase} \end{cases} \tag{4.9}$$

Here f denotes the chopping frequency of laser illumination. It's worth noting that for some chopping frequencies, the amount of current change during each half chopping cycle can be limited by the slow exponential decay rate for low bias region. This can result in a much smaller first harmonic component compared to the static ORS measurement. As shown in Figure 4.1a and b, we simulated the high-state population $n_H(V,t)$ for the first few chopping cycles of laser illumination, with 0.01 Hz and 273 Hz chopping frequencies respectively. The corresponding dynamic ORS are simulated according to Equation (4.4), (4.5) and (4.9) and displayed in Figure 4.1c and d. For the 0.01 Hz slow chopping, each half cycle is sufficiently long for $n_H(V,t)$ to decay to the new equilibrium, even for the slow decay rate at 21.04 mV. Therefore, the corresponding dynamic ORS preserves the majority of the low bias features (Figure 4.1c). For the 273 Hz fast chopping, each half chopping cycle is too short, and $n_H(V,t)$ at 22.04 mV and 61.12 mV decays faster during the bright half cycle than the dark half cycle, therefore we observe an overall shift towards the equilibrium population under the bright condition during the first few chopping cycles. $n_H(V,t)$ eventually forms a steady periodic fluctuation around the bright equilibrium population with a much smaller fluctuation amplitude than in the case of 0.01 Hz chopping. This leads to suppressed features in the low bias region of dynamic ORS (Figure 4.1d) as compared to the 0.01

Hz case. On the other hand, $n_H(V,t)$ decays fast enough at the high bias 221.44 mV due to its high switching rate, therefore no significant difference in its time evolution is observed between the fast and slow chopping cases. However, for the parameters used in this simulation, population difference between bright and dark is quite small in the high bias region due to the dominating transition rates induced by inelastic tunneling electrons, therefore the dynamic ORS signal is nearly zero for both fast and slow chopping cases. Figure 4.2a and b show the simulated dynamic ORS for different chopping frequencies from 0.01 Hz to 729 Hz and compares the in-phase components to the static ORS. As chopping frequency increases, we can observe a gradual decay for the in-phase components from the static ORS line shape to a low-bias filtered line shape, accompanied by small feature in the out-of-phase components. By comparing Figure 4.2b and c, we can see that a significant phase angle shift occurs near a specific bias for each chopping frequency, and the corresponding feature in out-of-phase components happens to fall in the region where phase shift occurs. Based on the discussion above, we can qualitatively interpret the phase shift bias threshold as the threshold to which the total molecular transition rate no longer catches the chopping frequency. The immergence of out-of-phase components only near the threshold bias can be attributed to the limited capture of phase-delayed signal within each chopping cycle. For bias below the phase shift threshold, where the chopping frequency far exceeds the molecular response, out-of-phase components will also reduce to zero.

Figure 4.1 Comparison of dynamic optical rectification spectra (ORS) for chopping frequency 0.1 Hz and 273 Hz. Time traces of high-state population n_H upon laser illumination chopped at (a) 0.01 Hz and (b) 273 Hz are simulated for four different biases. (c) and (d) are the simulated dynamic ORS with chopping frequency 0.01 Hz and 273 Hz respectively. A data set of experimentally measured bias-dependent transition rates at -500 mV/ 1 nA (Figure 3.8, positive bias data) are used for the dark transition rates. The parameters used for simulation include: photon rate coefficient $m_{H\to L} = 200\,\mathrm{Hz/unit\ power}$, saturated equilibrium constant $K_s = 3$ (defined as $K_s = \frac{m_{L\to H}}{m_{H\to L}}$ in chapter 3), laser power $p = 1$, low-state conductance $\sigma_L = 0.672\ \mathrm{pA/mV}$ and high-state conductance $\sigma_H = 4\sigma_L$.

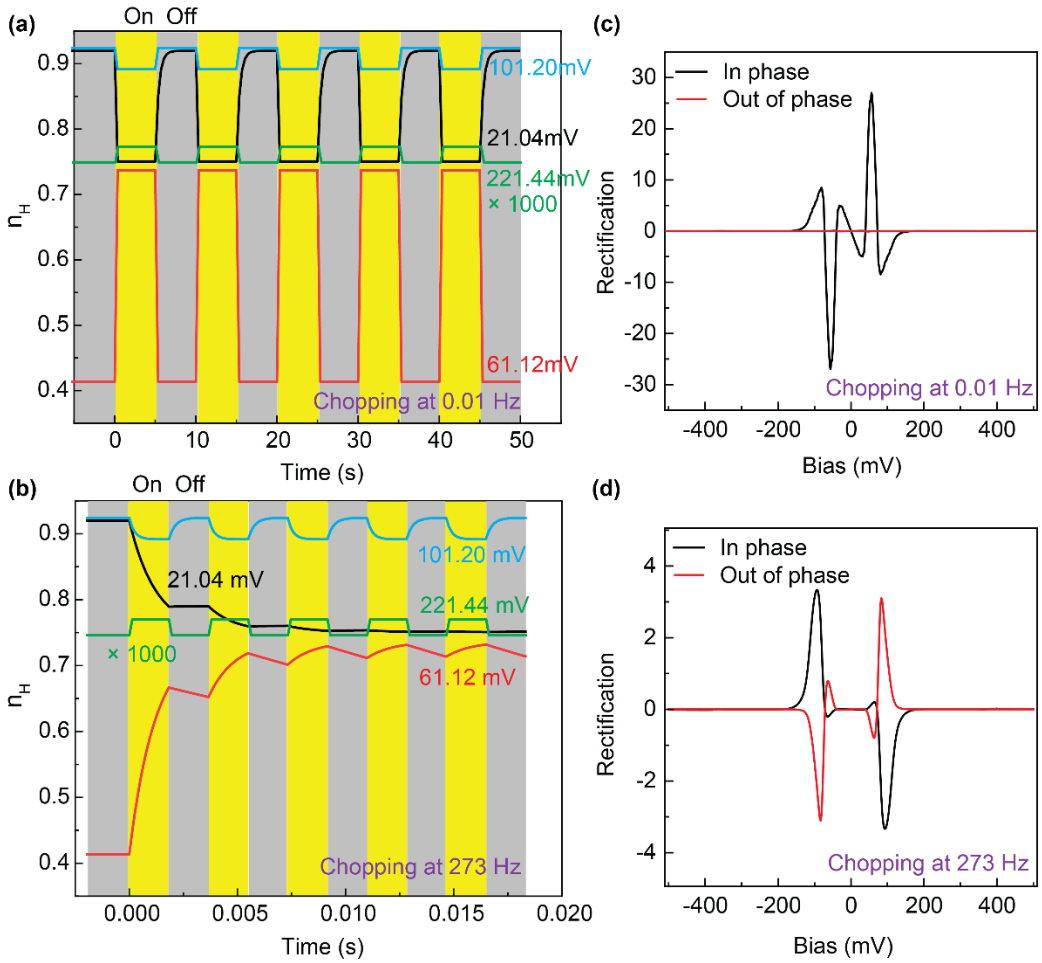

Figure 4.2 Simulated dynamic ORS of a pyrrolidine at different chopping frequencies. In-phase components (Rx), out-of-phase (Ry) components and phase angle of simulated dynamic ORS are displayed in (a), (b) and (c) respectively. The static ORS, which is light-off current subtracted from light on current, is displayed as gray dashed curve in (a) as a reference. The steep change in phase angle for low bias region is induced by insufficient switching rate of pyrrolidine compared to the chopping frequency. Curves in (a) and (b) are offset for clarity. The parameter used for simulation is the same as in Figure 4.1.

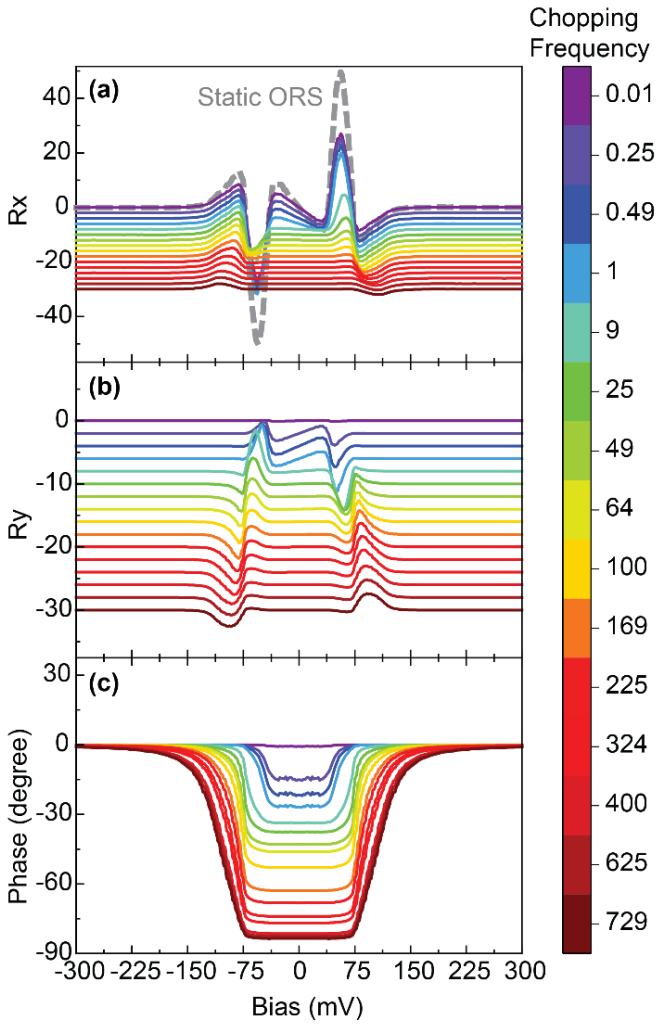

4.3 Experimental Methods

A Cu(001) substrate is prepared in the UHV chamber with repeated cycles of Neon bombardment at 1.5 keV energy and annealing at 650 ℃. All measurements are done with an atomic-sharp silver tip. The tip is prepared by repeated cycles of Neon bombardment at up to 1.5 keV and annealing. After sample is approached to tunneling distance, tip apex is further sharpened by gentle poking on the substrate. Pyrrolidine (>99.5%, Sigma Aldrich) is purified with repeated freeze-pump-thaw procedures and evaporated to a clean Cu(001) substrate cooled to 8K.

To measure the dynamic ORS of a pyrrolidine molecule, we couple a tunable distributed feedback (DFB) laser to the tunneling junction of a low temperature home-made STM. As shown in Figure 4.3, the DFB laser output is fiber-coupled to an electrical variable optical attenuator (EVOA#1), the output of EVOA#1 is split by a 25:75 splitter with the 25% portion fed to a photodiode to monitor the power. The photocurrent is then used as a feedback signal for a PID power control box, which regulates the input of EVOA#1 to maintain a stable power output after EVOA#1. The 75% portion of light is coupled to EVOA#2, which is controlled by a synced square wave signal from lock-in amplifier to provide the periodic chopping of light. The chopped light from EVOA#2 is finally coupled to a fiber collimator and converted into free-space collimated beam. The collimated beam is focused and aligned into STM junction. The detailed alignment method for 1550 nm light beam is described in chapter 3 Supporting Information 3.6.2. With tip placed over the center of a pyrrolidine molecule in constant height mode, the tunneling current is measured by a pre-amplifier, and a lock-in amplifier is used to extract the first harmonic component for the optical rectification signal at different sample biases.

Figure 4.3 Experimental setup for optical rectification measurement.

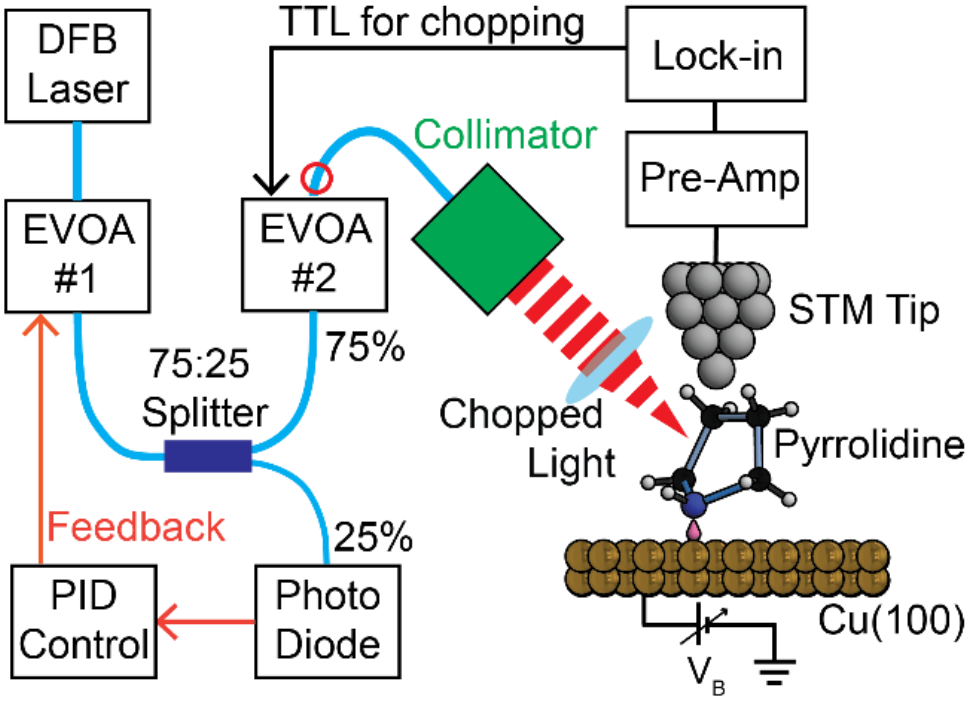

During the experiment, if a slow chopping is applied, the chopped laser illumination can cause a large thermally induced junction gap oscillation that yields big artificial offset in the ORS signal. On the other hand, if chopping frequency is too high, a large signal suppression can occur due to the limited bandwidth of the pre-amplifier. Balancing the two limiting factors, a 273 Hz chopped light at 1548 nm was used for all dynamic ORS measurements in our experiment. With a 273 Hz chopping frequency, the thermally induced junction gap oscillation was observed to be very small, typically less than 1 picometers for the laser power used. This amount of junction gap oscillation doesn't give rise to significant offset signal in the ORS, therefore, no tip height compensation is used for the 1548 nm ORS measurements.

4.4 Results and Discussion

To investigate the setpoint dependence of ORS line shapes, we measured dynamic ORS of a pyrrolidine molecule with fixed setpoint bias at -500 mV and different setpoint current values from 56 pA to 2 nA, as shown in Figure 4.4a and b. Due to the overall good polarity symmetry of the dynamic ORS line shape, we herein only discuss line shape features in the negative bias and assume the same conclusion applies to the positive bias side. For setpoint current below 0.5 nA, there is a small negative overshoot (Figure 4.4a inset) for the in-phase component near -200 mV, forming a Fano-type line shape with the main peak near -100 mV. For setpoint current above 0.5 nA, the positive ORS signal near -100 mV drops to zero towards higher bias direction without overshoot features. To understand this setpoint-dependent line shape variation, we need to understand how transition rates vary under different tunneling gaps, which involves investigation of photon-induced and dark transition rate as a function of tunneling setpoint current. For photon-induced transitions, due to the lack of sufficient experimental data, we assume a simple linear relation between the photon-induced transition rate and the setpoint current value, with an

unchanged ratio K_s between the L → H and H → L transition photon rate coefficients. For tunneling electron induced rate, we measured the dark condition transition rate as a function of setpoint current for the target bias -378 mV and -20mV, as shown in Figure 4.5a and b. For -378 mV, where the transition rates are dominated by inelastic tunneling electron contribution, L → H transition rate increases linearly as a function of setpoint current, while H → L transition rate increases in an exponential decay fashion, indicating an overall reaction equilibrium shift towards high state as the tunneling gap decreases. Whereas for -20 mV, where only thermally-induced transitions are detected, L → H transition rate increases with setpoint current in a logarithm fashion and H → L transition rate decreases with setpoint current in an inversed logarithm fashion. Taking the experimentally measured bias dependent transition rate at -500mV/1 nA as a reference, we introduce a modified version of Equation (4.1) and (4.2) to simulate the transition rate at different tunneling setpoints:

$$\begin{cases} R_{L\to H(H\to L)}(V,\nu,p,I_{set}) = R_{L\to H(H\to L),dark}(V,I_{set}) + m_{L\to H(H\to L)}(\nu,I_{set})\times p \\ m_{L\to H(H\to L)}(\nu,I_{set}) = \dfrac{I_{set}}{I_{ref}} m_{L\to H(H\to L)}(\nu,I_{ref}) \\ R_{L\to H,dark}(V,I_{set}) = \alpha_1(I_{set})\sum_{i(j)} k_{i(j)} I_{IET,i(j)}(V,I_{ref}) + \alpha_2(I_{set}) C_{L\to H(H\to L)}(I_{ref}) \\ R_{H\to L,dark}(V,I_{set}) = \beta_1(I_{set})\sum_{i(j)} k_{i(j)} I_{IET,i(j)}(V,I_{ref}) + \beta_2(I_{set}) C_{L\to H(H\to L)}(I_{ref}) \end{cases} \quad (4.10)$$

Here, I_{ref} is the reference current setpoint at which dark transition rates are measured and used for simulation. I_{set} is the current setpoint to be computed. The correction pre-factors $\alpha_1(I_{set})$, $\alpha_2(I_{set})$, $\beta_1(I_{set})$ and $\beta_2(I_{set})$ are obtained through fitting of the transition rate data in Figure 4.5a and b.

With the simulated transition rates calculated with Equation (4.10), we computed the dark condition high-state population $n_{H,eq}^{Dark}(V)$(shown in **Error! Reference source not found.** 4.5c).

The high state population is shifted upward with increasing setpoint current, which can be attributed to the potential surface modification in pyrrolidine due to increased tip-molecule interaction. On the other hand, when comparing $n_{H,eq}^{Dark}(V)$ to the equilibrium high-state population at saturated laser power $\lim_{power\to\infty} n_{H,eq}^{Bright}(V)$, which is calculated to be 0.75 for $K_s = 3$, it's interesting to see that $n_{H,eq}^{Dark}(V) \geq \lim_{power\to\infty} n_{H,eq}^{Bright}(V)$ in the bias range of -100 mV to -200mV for setpoint current 1 nA and 2nA, while $n_{H,eq}^{Dark}(V) < \lim_{power\to\infty} n_{H,eq}^{Bright}(V)$in bias range of -100 mV to -200mV for setpoint current equal and below 0.5 nA. This leads to positive $\Delta n_H(V)$ near -200 mV for setpoint current 1 nA and 2nA and negative $\Delta n_H(V)$ for setpoint current equal and below 0.5 nA (shown Figure 4.5d), hence a positive static ORS signal for setpoint current 1 nA and 2nA and negative static ORS signal for setpoint current equal and below 0.5 nA (shown in Figure 4.5e), according to Equation (4.6). Even for the smallest setpoint current 56 pA, the simulated total transition rate at -200 mV is around 10^5 Hz, which is much higher than the 273 Hz chopping frequency, therefore we can expect static ORS feature near -200 mV to be well preserved in the dynamic ORS measurements for all setpoints measured here, which provide a qualitative explanation to the line shape variation observed for different setpoint gaps. With the simulated $R_{L\to H(H\to L)}(V, \nu, p, I_{set})$ for each setpoint current, we further computed the dynamic ORS as shown in Figure 4.4c and d. The simulated line shape variation is highly consistent with the experimental data, which also validates the assumption we made about the photon-induced transition rate correction in Equation (4.10).

Figure 4.4 Experimental and simulated results of single-pyrrolidine ORS at different tunneling setpoints. (a) and (b) are experimentally measured in-phase (Rx) and out-of-phase (Ry) components. (c) and (d) are simulated in-phase and out-of-phase components. Insets of (a) and (c) display the enlarged in-phase data in the range -300 mV to 0 mV to show the line shape transition with increasing tunneling gap. For a setpoint at –500 mV/x nA, parameters used for simulation include: photon rate coefficient $m_{H\to L} = 200 \cdot x\,\mathrm{Hz/unit\,power}$, saturated equilibrium constant $K_s = 3$ (defined as $K_s = \frac{m_{L\to H}}{m_{H\to L}}$ in chapter 3), laser power $p = 2$, low-state conductance $\sigma_L = 0.672 \cdot x\,\mathrm{pA/mV}$ and high-state conductance $\sigma_H = 4\sigma_L$. The dark rate data used for simulation is adjusted for each setpoint based on the setpoint dependence measurement shown in **Error! Reference source not found.**.

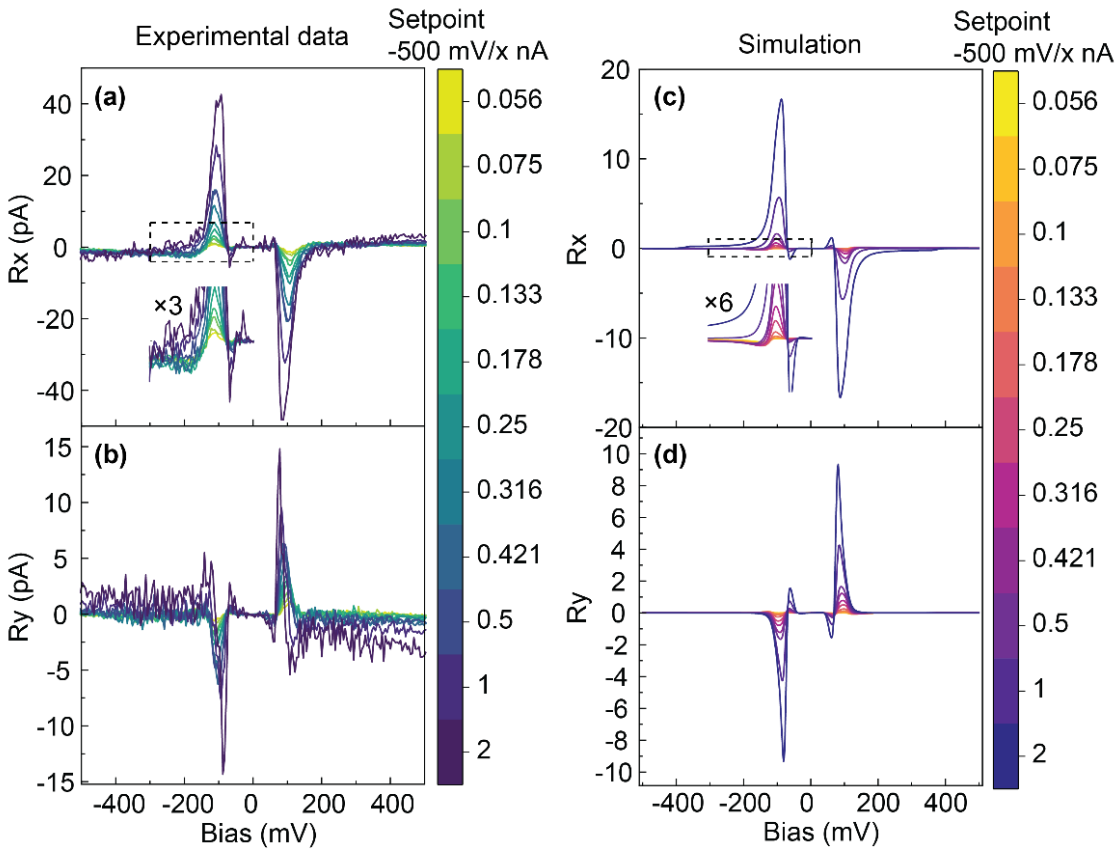

Figure 4.5 Setpoint dependence of transition rate and static ORS simulation. (a) and (b) display experimentally measured transition rate with constant height probing at -500 mV setpoint bias and varying current setpoints for a target bias at -378 mV and -20 mV respectively. The fitted results are displayed as solid curves. (c) The dark condition high-state population is plotted as a function of sample bias for different setpoint current values. The dashed red line indicate the equilibrium high-state population with light illumination at an infinitely high power. (d) Light induced change in high-state population (calculated from subtraction between red dashed line and other curves in (c)) is plotted as a function of bias for different setpoint current values, for the light illumination at an infinitely high power. (e) Static ORS (light-induced tunneling current difference) is calculated from curves in (d) according to equation (4.6)

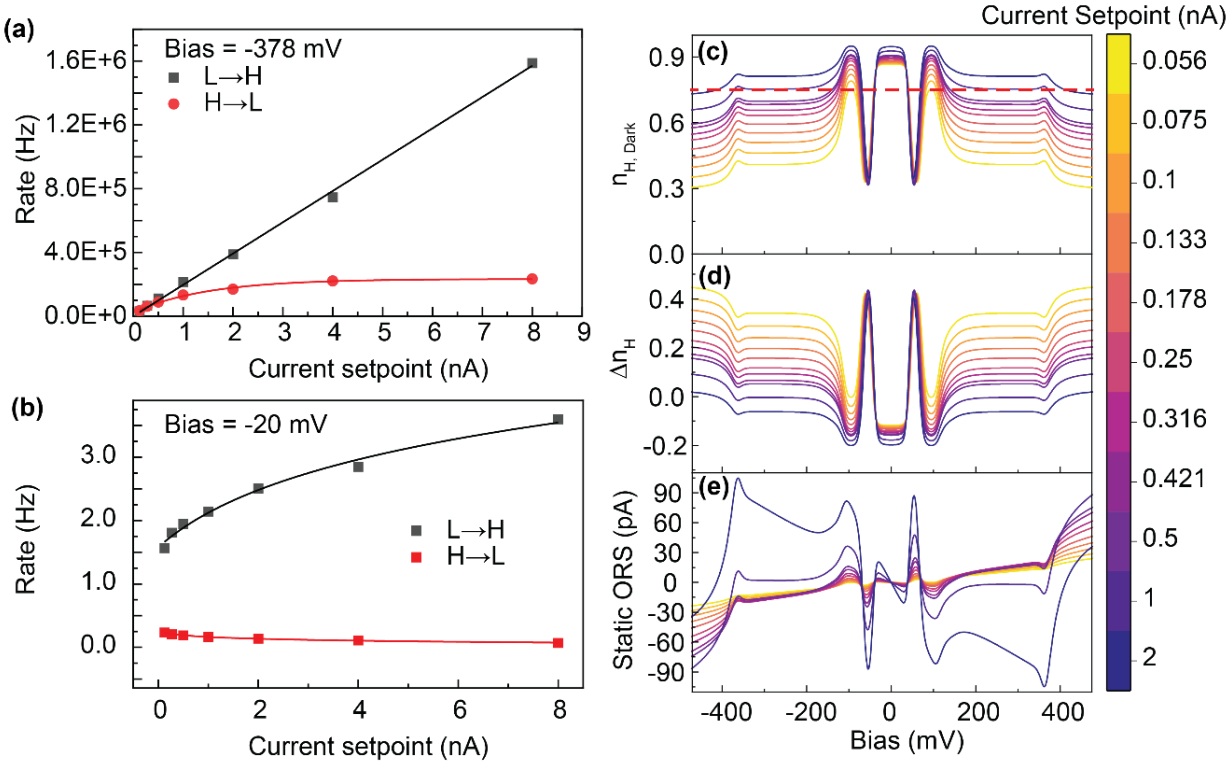

Although chopping should cause no suppression to the feature in high bias region due to the high transition rate, it is still elusive that for all dynamic ORS measurements we have performed, the line shape is nowhere close to the simulated static ORS in Figure 4.5e for high bias region. Given that Figure 4.5e displays the simulated static ORS for the extreme case of infinitely high-power illumination, it's necessary to consider the finite power effect in the ORS line shape. Figure 4.6a-d show the power-dependence measurements of dynamic ORS with a close setpoint – 500 mV/2 nA and a far setpoint -500 mV/ 56 pA and corresponding simulations are displayed in Figure 4.6 e – h with highly consistent line shapes. We noticed that even for the strongest laser power used, there is still no strong features in high bias region. Besides, the overall signal intensity doesn't increase linearly with the power for both setpoints, instead, there are signs of saturation in the signal as power is increased. To understand such power dependence behavior, we further simulated the $n_{H,eq}^{Bright}(V)$, $\Delta n_H(V)$, and static ORS for both setpoints and compare them to the extreme case with infinitely high-power illumination, as shown in Figure 4.7. From the simulation, 3 insights can be obtained:

1. Under a finite power illumination, the high-state population $n_{H,eq}^{Bright}(V)$ always falls in the range between $n_{H,eq}^{Dark}(V)$ and $\lim_{power\to\infty} n_{H,eq}^{Bright}(V)$, therefore the photon-induced population change $\Delta n_H(V)$ is always in the range between zero and $\lim_{power\to\infty} n_{H,eq}^{Bright}(V) - n_{H,eq}^{Dark}(V)$. This defines a specific direction in which the ORS signal can increase with stronger illumination power and an asymptotic limit for the ORS signal with extremely high-power illumination.

2. For low bias region ($|V|<$ +100 mV), the dark transition rate is relatively small and easily overpowered by photon-induced transitions, therefore the high-state population $n_{H,eq}^{Bright}(V)$ can

very quickly approach the high-power limit defined by $\lim_{\text{power}\to\infty} n_{H,eq}^{Bright}(V)$, thus the static ORS signal saturates pretty quickly in the low bias region with increasing illumination power.

3. For high bias region (|V|>100 mV), the dark transition rate grows rapidly with increasing bias so that photon-induced transitions become negligible in terms of driving the population change, therefore suppressing the potentially existing features in the static ORS. It is in this region that the static ORS starts to deviate from its saturation limit rapidly and reduce towards zero with increasing bias.

The finite power effect observed in static ORS simulation is expected to be preserved into the dynamic ORS, except that low bias features are flattened due to chopping suppression effect. For the experimental measurements we have made, even the highest laser power used was far too small to induce significant population shift in high bias region, therefore, the dynamic ORS signal is always very small in the high bias region. It's worth mentioning that, although we are discussing the finite power effect, it is in fact the total photon-induced transition rate that matters. If the photon rate coefficient is extremely high, for example, due to the localized surface plasmon excitation, we can still expect a strong signal with relatively weak power of laser illumination. A good example is demonstrated in Figure 4.8 by comparing a 635 nm dynamic ORS to a 1548 nm dynamic ORS. Although the nominal power used for 1548 nm is more than ten times higher than the 635 nm light, the resulting signal intensity is comparable between the two.

Figure 4.6 Experimental and simulated results of single-pyrrolidine ORS at different laser powers for -500 mV/ 2 nA and -500 mV/ 56 pA. In-phase (Rx) and out-of-phase (Ry) components are displayed in separate plots. (a) to (d) are experimental measurements taken with 273 Hz chopped laser illumination, each power unit represent 1.356 mW nominal power before chopped. (e) to (h) are simulated results. Same parameters are used for simulation as in (c) and (d).

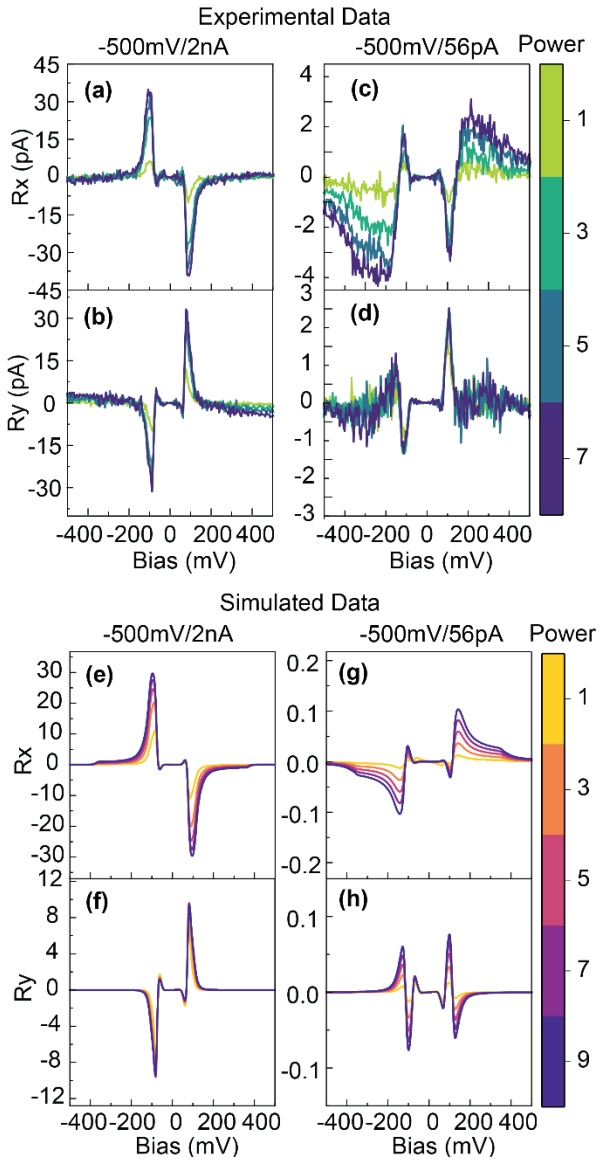

Figure 4.7 Simulation of power dependence of static ORS for -500 mV/ 56 pA and -500 mV/ 2 nA. (a)(d) High-state population n_H with constant-power laser illumination as a function of bias for different laser powers. The special case of dark condition (zero power) and infinitely high-power laser illumination are displayed as gray and yellow dashed curves respectively. (b)(e) Laser induced change in high-state population Δn_H as a function of bias for different laser powers. The special case of infinitely high-power laser illumination is displayed as yellow dashed curve. (c)(f) static ORS calculated from current subtraction between bright and dark condition. The special case of infinitely high-power laser illumination is displayed as yellow dashed curve. Same parameters are used for simulation as in Figure 4.4(c) and (d).

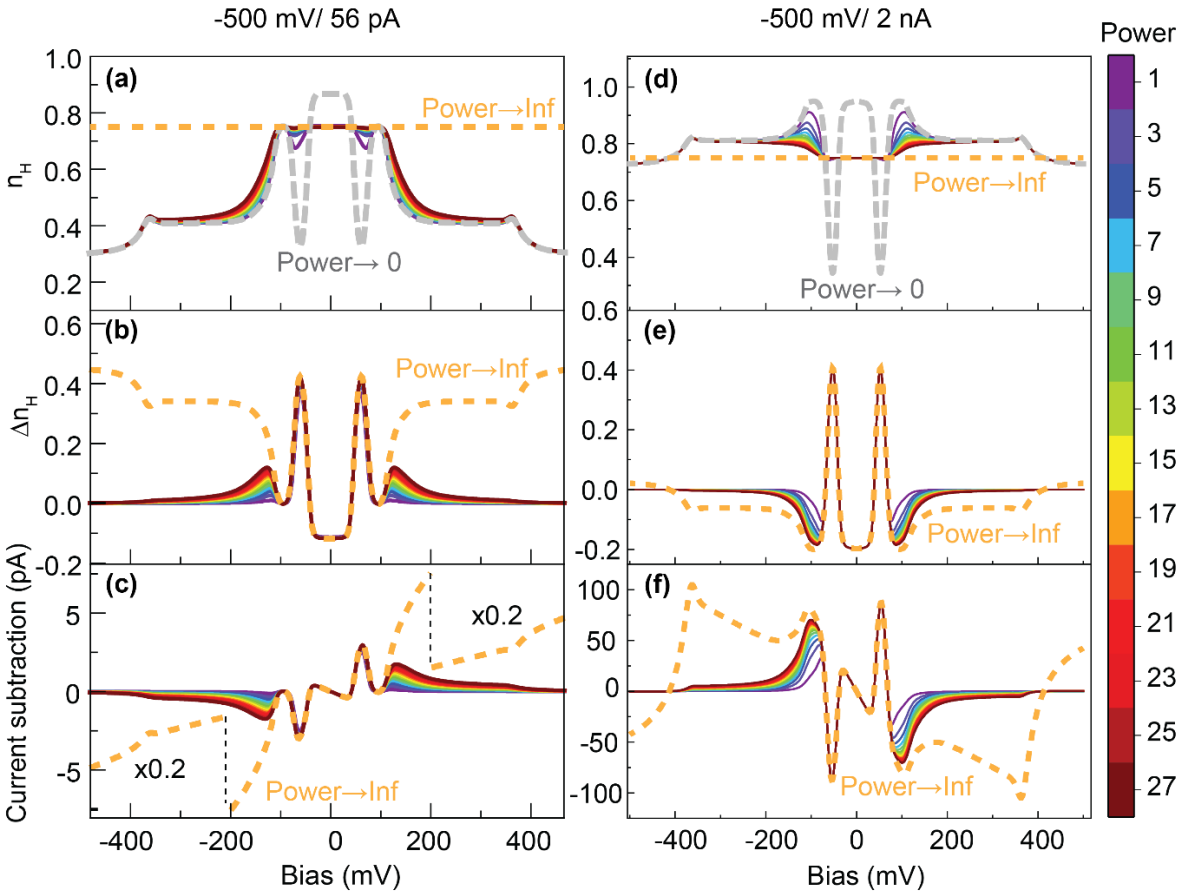

Figure 4.8 Comparison between a 635 nm dynamic ORS and a 1548 nm dynamic ORS taken at -500 mV/ 2nA. A nominal power (before chopping) of 100 μW and 1.36 mW are used for the 635 nm and 148 nm measurements respectively.

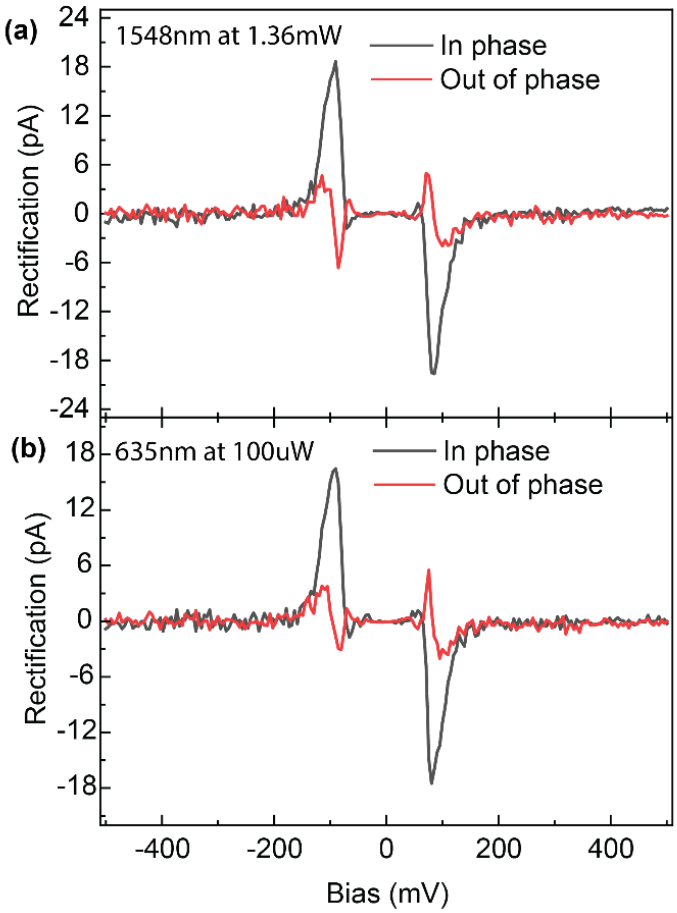

4.5 Conclusion

In summary, we report the line shape and signal variation in dynamic ORS measurement on a single pyrrolidine molecule as a function of tunneling setpoint and illumination power. Theoretical simulation based on a two-level system model and a modified transition rate model were used to illustrate the relation between the static ORS and the dynamic ORS measurements. We revealed that the dynamic ORS line shape is essentially determined by the dynamic light induced population shift, which is susceptible to many other factors including light chopping frequency, laser power, photon rate coefficient and dark condition transition rate. Combining experimental data, we successfully reproduced the dynamic ORS through simulation for different setpoints and illumination power, which validates the adopted theoretical models. With the simulation demonstrated in this paper, we can also obtain useful predictions to ORS measurements for conditions not achieved in our experimental setup and achieve highly controlled engineering of single molecule photo-rectifier.

Bibliography

[1] L. Sun, Y.A. Diaz-Fernandez, T.A. Gschneidtner, F. Westerlund, S. Lara-Avlia, and K. Moth-Poulsen, Chemical Society Reviews, **43**, 7378–7411 (2014).

[2] H. Song, M.A. Reed, and T. Lee, Advanced Materials, **23**, 1583–1608 (2011).

[3] M. Tsutsui and M. Taniguchi, Sensors (Switzerland), **12**, 7259–7298 (2012).

[4] M. Bazarnik, L. Jurczyszyn, R. Czajka, and K. Morgenstern, Physical Chemistry Chemical Physics, **17**, 5366–5371 (2015).

[5] T. Darwish and S. Ciampi, Nano Letters, **14**, 7064–7070 (2014).

[6] J. Henzl, P. Puschnig, C. Ambrosch-Draxl, A. Schaate, B. Ufer, P. Behrens, and K. Morgenstern, Physical Review B, **85**, 035410 (2012).

[7] M.J. Comstock, N. Levy, J. Cho, L. Berbil-Bautista, M.F. Crommie, D.A. Poulsen, and J.M.J. Fŕchet, Applied Physics Letters, **92**, 123107 (2008).

[8] M.J. Comstock, N. Levy, A. Kirakosian, J. Cho, F. Lauterwasser, J.H. Harvey, D.A. Strubbe, J.M.J. Fréchet, D. Trauner, S.G. Louie, and M.F. Crommie, Physical Review Letters, **99**, 038301 (2007).

[9] K. Yadav, S. Mahapatra, T. Halbritter, A. Heckel, and T.G. Gopakumar, Journal of Physical Chemistry Letters, **9**, 6326–6333 (2018).

[10] C. Nacci, M. Baroncini, A. Credi, and L. Grill, Angewandte Chemie, **130**, 15254–15259 (2018).

[11] J. Yao, Y. Park, and W. Ho, In Preparation.

[12] Y. Kim, K. Motobayashi, T. Frederiksen, H. Ueba, and M. Kawai, Progress in Surface Science, **90**, 85–143 (2015).

[13] A. Halbritter, L. Borda, and A. Zawadowski, Advances in Physics, **53**, 939–1010 (2004).

[14] A. Halbritter, P. Makk, S. Csonka, and G. Mihály, Physical Review B - Condensed Matter and Materials Physics, **77**, 075402 (2008).

[15] J. Gaudioso, L.J. Lauhon, and W. Ho, Physical Review Letters, **85**, 1918–1921 (2000).

Chapter 5

Concluding Remarks and Future Prospects

5.1 Concluding Remarks

Combining an 8-Kelvin STM with a tunable CW Terahertz source or optical lasers, we were able to extend the single molecule vibrational spectroscopy into new spectral ranges with superior energy resolution compared to traditional IETS spectroscopy.

We developed CW Terahertz rectification spectroscopy (THz RS) as an alternative vibrational spectroscopy technique to IETS. THz RS provides the same good chemical sensitivity for molecular characterization while the signal intensity exhibiting extra sensitivity to THz near field and far field. The development of CW THz RS paves the way for THz frequency domain spectroscopy, which can probe resonant excitation of low energy vibrational modes or spin excitations in the THz region with <10 MHz frequency resolution. It is beneficial to combine the CW THz source with our ultrafast THz STM to achieve a joint temporal and energy resolution in single molecule studies. Moreover, the sensitivity of THz rectification signal to weak variation in THz far field intensity makes it promising for application in single molecule THz detectors. The fast-oscillating electric field of CW THz radiation also makes it useful as a tool to study frequency response of molecular systems exhibiting ultrafast switching dynamics that is not detected through tunneling current measurement by a pre-amplifier.

The wavelength-dependence study of pyrrolidine isomerization provides a new perspective in single molecule laser action spectroscopy. We demonstrated the advantage of photon equilibrium measurement to the photon yield action spectra in the context of a reversible single molecule

reaction. Not only does photon equilibrium action spectroscopy reveal how the reaction kinetics can be influenced by photon energy, but it also allows for detection of tiny shifts in mode energies of a molecule induced by change in molecule structure, local adsorption environment, and tip geometry with sub-meV energy resolution.

By measuring photocurrent in a single pyrrolidine molecule with optical rectification spectroscopy, we also demonstrate STM tuning of a single molecule photo-rectifier. The sample bias, laser power and tip-substrate distance dependence of the optical rectification signal has shown that the competition between photon-induced conformational transitions and electron-induced transitions can be engineered through multiple factors and leads to effective tuning of the photocurrent. This study has shown the great potential in photo-switching molecules as tunable single molecule devices for photo-mixing and phototransistor.

5.2 Future Prospects

Overall, all three studies have served the same purpose in expanding the STM capability in probing and control of chemical reactions on a single-molecule level. Other than rectification measurement, we can also perform spin sensing with the CW THz source using a functionalized tip. For example, a nickelocene attached to tip can be used to probe exchange interaction with other spin centers on surface.[1–4]

With the tunable DFB laser near 1550 nm in our current experimental setup, only a limited energy range was explored, and it is hard to give conclusive remarks on the fine features observed with laser action spectroscopy. Therefore, a tunable CW optical laser sources with a broader frequency range is desired for further study on vibration-mediated isomerization of pyrrolidine. Besides, isotope substitution in pyrrolidine can be used to check if the features observed in action spectra is induced by X-H bonds. Using the photon equilibrium action spectroscopy, we can further study

photocatalytic dynamics of other single-molecule reversible photo-switching reactions, such as porphycene cis-cis tautomerization[5], $(OH)_2$ flipping[5], manganocene spin crossover switching[6] and azobenzene derivatives isomerization[7,8], etc.

Bibliography

[1] B. Verlhac, N. Bachellier, L. Garnier, M. Ormaza, P. Abufager, R. Robles, M.L. Bocquet, M. Ternes, N. Lorente, and L. Limot, Science, **366**, 623–627 (2019).

[2] M. Ormaza, N. Bachellier, M.N. Faraggi, B. Verlhac, P. Abufager, P. Ohresser, L. Joly, M. Romeo, F. Scheurer, M.L. Bocquet, N. Lorente, and L. Limot, Nano Letters, **17**, 1877–1882 (2017).

[3] M. Ormaza, P. Abufager, B. Verlhac, N. Bachellier, M.L. Bocquet, N. Lorente, and L. Limot, Nature Communications, **8**, 1974 (2017).

[4] G. Czap, P.J. Wagner, F. Xue, L. Gu, J. Li, J. Yao, R. Wu, and W. Ho, Science, **364**, 670–673 (2019).

[5] H. Böckmann, M. Müller, A. Hammud, M.G. Willinger, M. Pszona, J. Waluk, M. Wolf, and T. Kumagai, Journal of Physical Chemistry Letters, **10**, 2068–2074 (2019).

[6] F.H. Koehler and B. Schlesinger, Inorganic Chemistry, **31**, 2853–2859 (1992).

[7] M. Bazarnik, J. Henzl, R. Czajka, and K. Morgenstern, Chemical Communications, **47**, 7764–7766 (2011).

[8] M. Bazarnik, L. Jurczyszyn, R. Czajka, and K. Morgenstern, Physical Chemistry Chemical Physics, **17**, 5366–5371 (2015).

Appendix A

Modification to STM IV for THz/Optical Coupling

In order to couple Terahertz (THz) wave into STM junction with high efficiency, modifications were made to the previous optical-STM system for better transmission of THz radiation while still capable of optical transmission. The modifications can be divided into 4 parts as shown in Figure A.1.

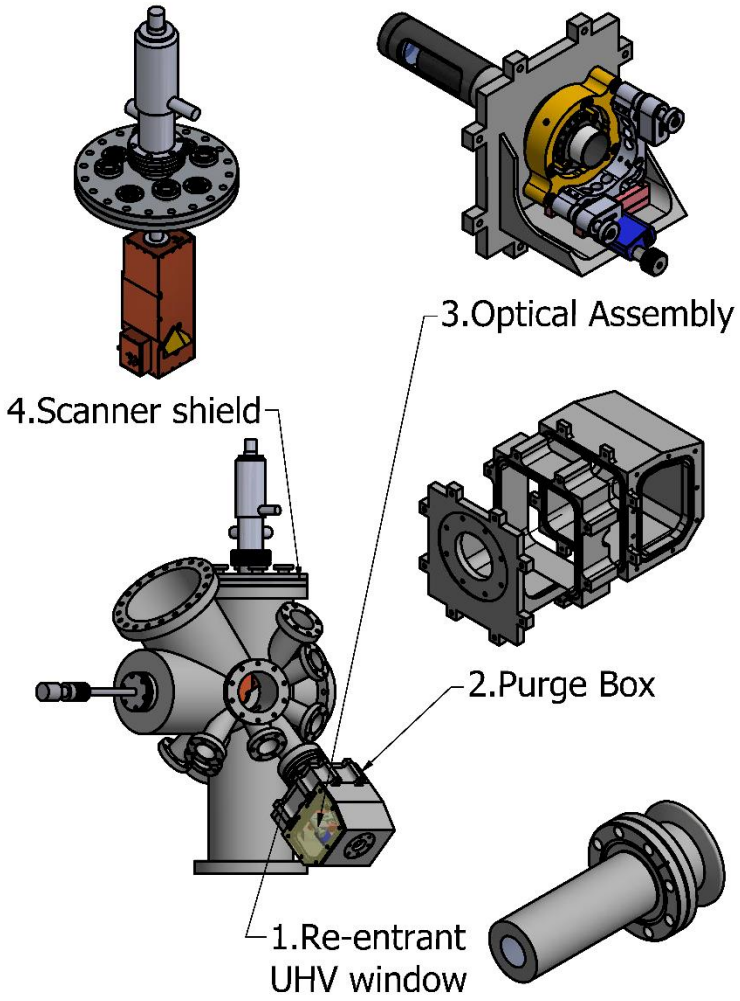

Figure A.1 Overview of major modifications for THz-STM

A.1 UHV Window Design

To accommodate both THz radiation and optical radiation of visible/IR range, a custom-designed re-entrant UHV viewport (manufactured by MPF Products Inc.) with a 3mm thick Z-cut crystal quartz window is used for the UHV Chamber (see Figure A.2). Although polymer materials such as Tsurupica and TPX have even better THz transmission, Z-cut crystal quartz is selected due to its good hardness and heat resistance, making it ideal for UHV sealing applications. The viewport is manufactured with an extension welding neck, which is later welded to an NW50 flange by the local machine shop. The NW50 flange is used for connection with the purge box that holds the entire THz optical assembly.

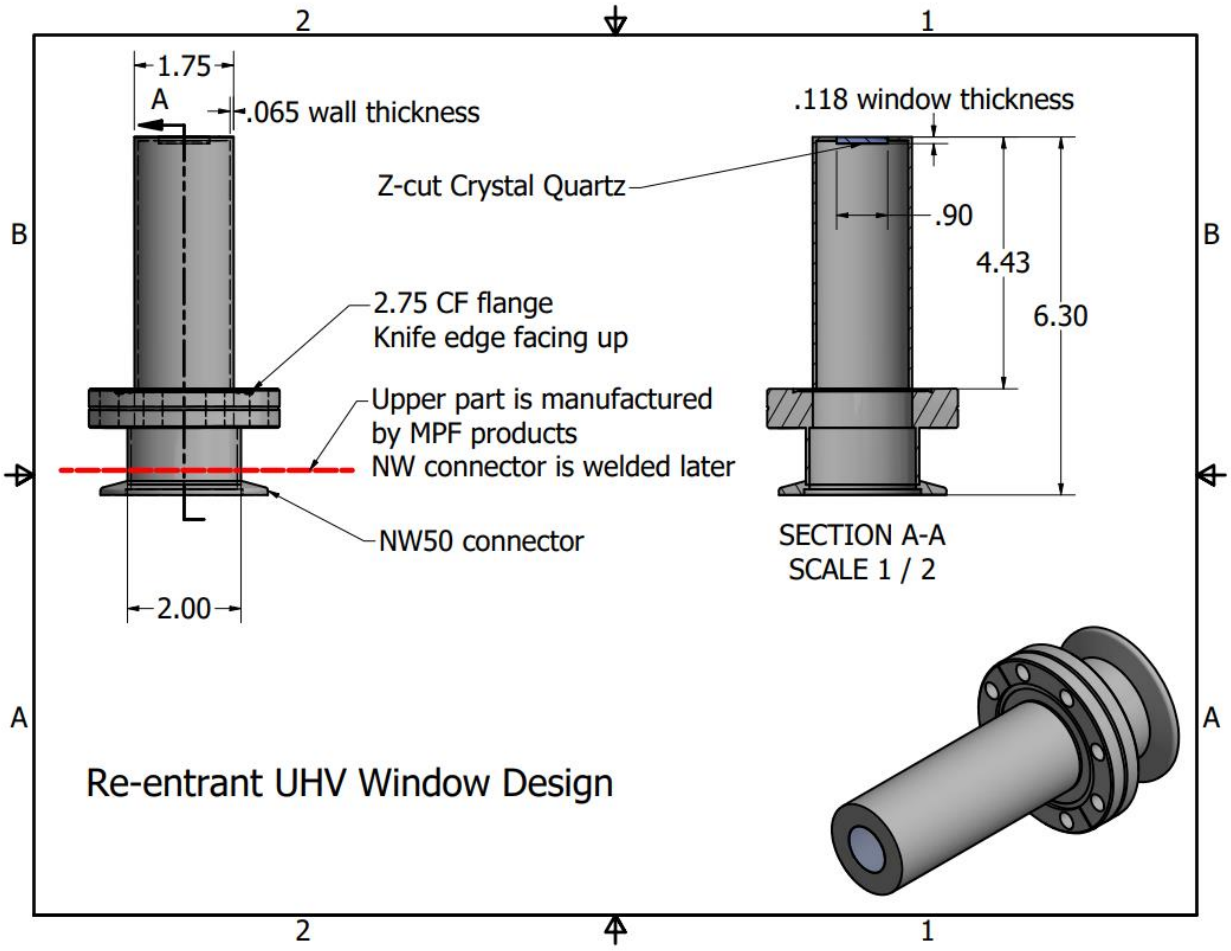

Figure A.2 Drawing of re-entrant UHV quartz window design.

A.2 Purge Box

The purge box consists of 3 major parts: the flange bracket (see drawings in Figure A.3), the box extension piece (see drawing in Figure A.4) and the cover box (see drawings in Figure A.5). An acrylic cover for side viewport (see drawing in Figure A.6) is used to seal the access/view port on cover box. The flange bracket is attached to the UHV chamber by a NW50 connector, and the entire optical assembly is mounted on the flange bracket through the linear stage. The NW25 ports on the cover box are designed for feedthrough connection and vacuum pumping or purging port.

When not purging, extension piece and cover box can be taken off for easy access of the optical assembly. When setting up for purging, put the box extension piece in place first and make sure all the cables for piezo actuator power and optical fibers are collected within the semi-circle notch on the extension piece (as shown in Figure A.4), then add the cover box carefully and use 8 long 8-32 threaded rods and nuts to fix the cover box and extension piece to the flange bracket.

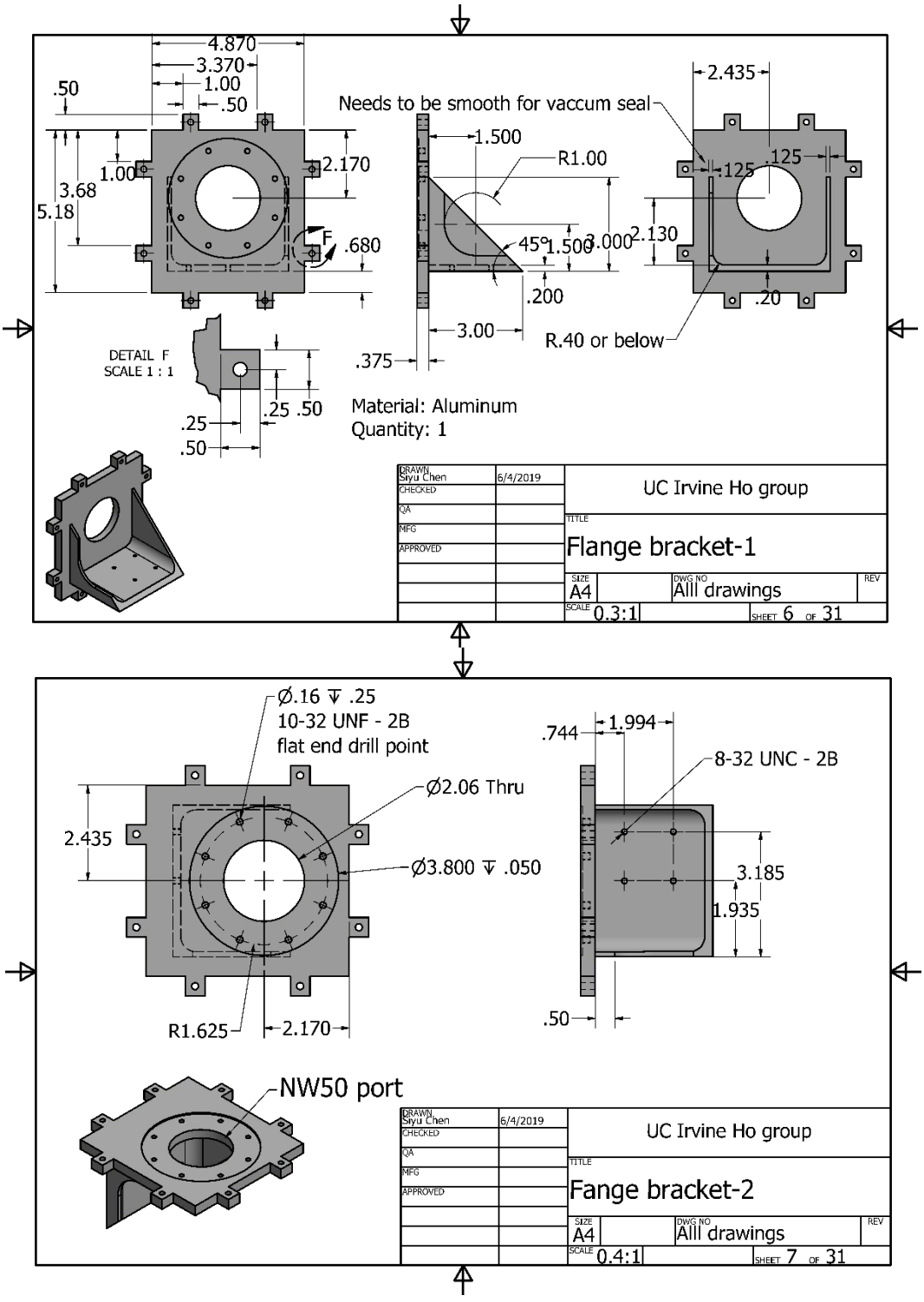

Figure A.3 THz purge box-Flange bracket

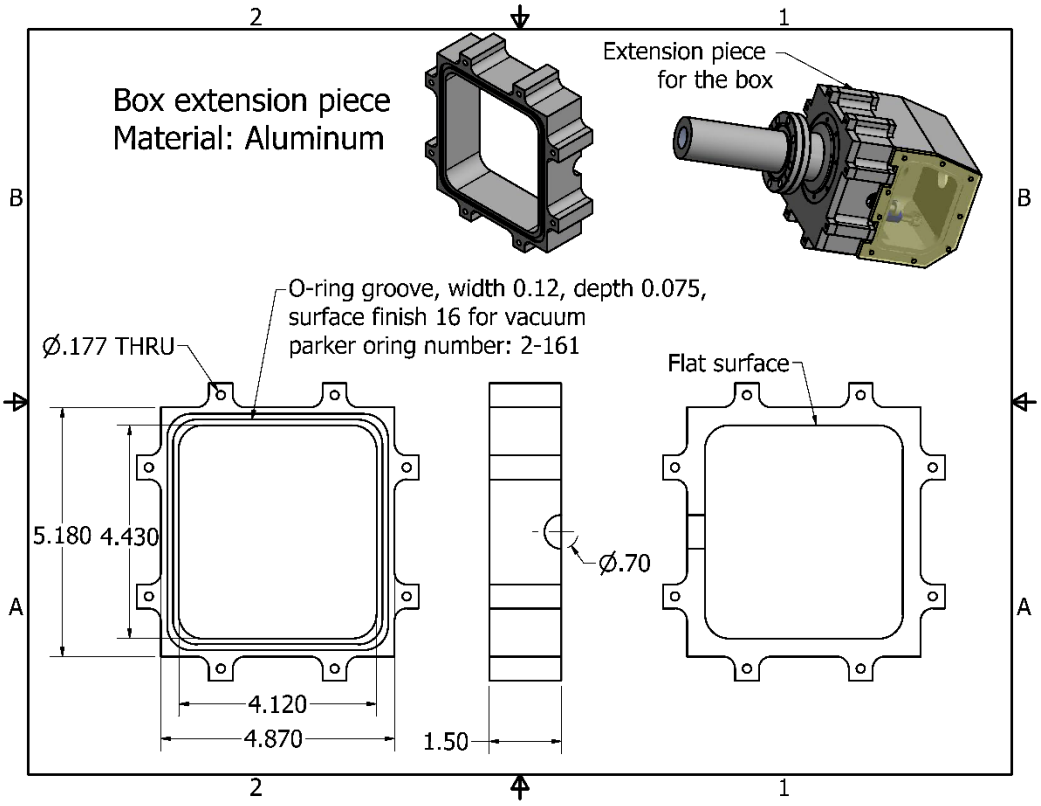

Figure A.4 THz purge box extension piece

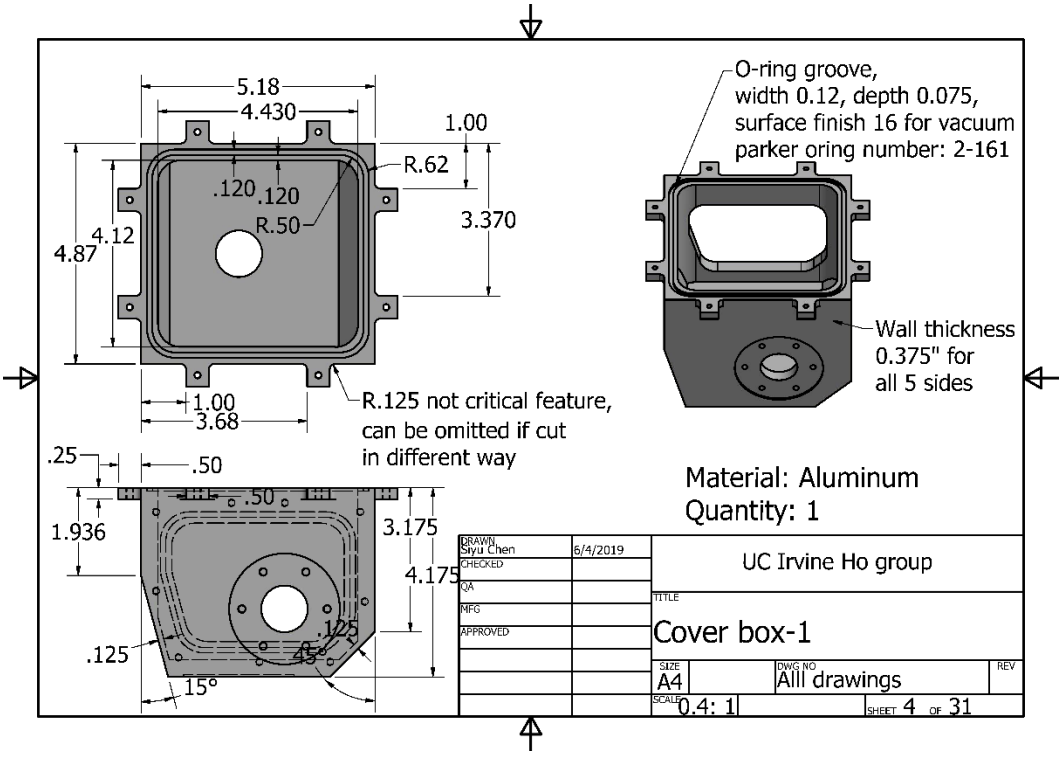

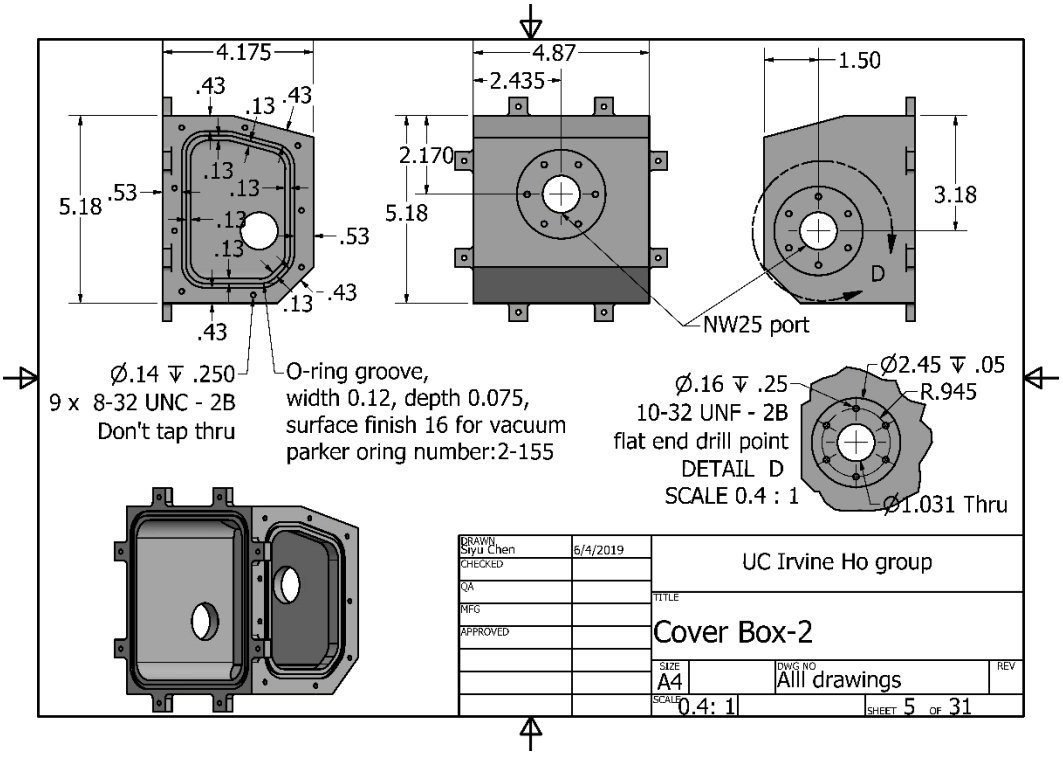

Figure A.5 THz purge box- Cover box

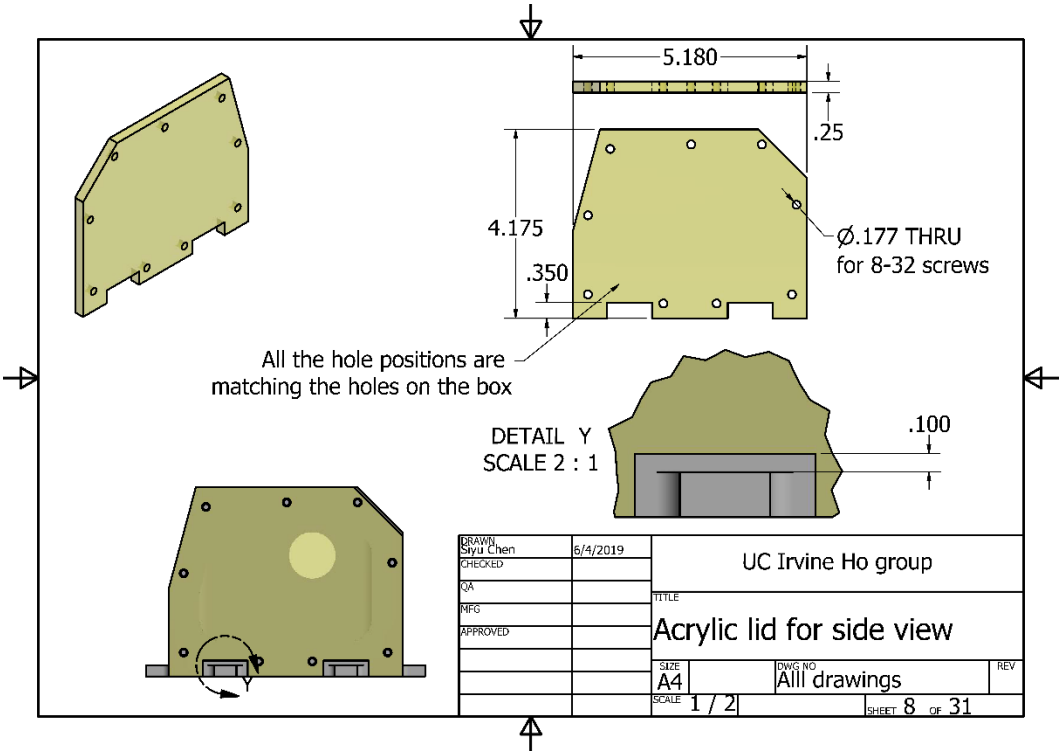

Figure A.6 Acrylic lid for side view

A.3 Optical Assembly

The optical assembly is mounted on the flange bracket and consists of a list of the following as indicated in (Figure A.7):

a. Tsurupica lens (Broadband Inc. P/N: Tsurupica-RR-CX-1.5-100-SPS-1")
b. TPX lens (BATOP GmbH P/N: TPX-D25.4-f32.5)
c. Photoconductive antenna (PCA) emitter (Toptica P/N: TeraScan1550)
d. Lens tube mounting Tsurupica lens (Thorlabs Inc. P/N: SM1L03)
e. Lens tube mounting TPX lens and PCA emitter (Thorlabs Inc. P/N: SM1L30)
f. Lens tube (Thorlabs Inc. P/N: SM1L20)
g. Adjustable lens tube (Thorlabs Inc. P/N: SM1V15)
h. Rotational mount (normally locked) (Thorlabs Inc. P/N: LRM1)
i. Custom 1.5’ to 2” adapter for rotation mount (see drawing in Figure A.8)
j. Piezo actuated kinematic Ø2” optical mount (Newport Corporation P/N: 8822-AC)
k. Linear stage (Newport Corporation P/N: 9062-COM)
l. Closed-loop piezo actuator (Physik Instrumente P/N: N-472.210)

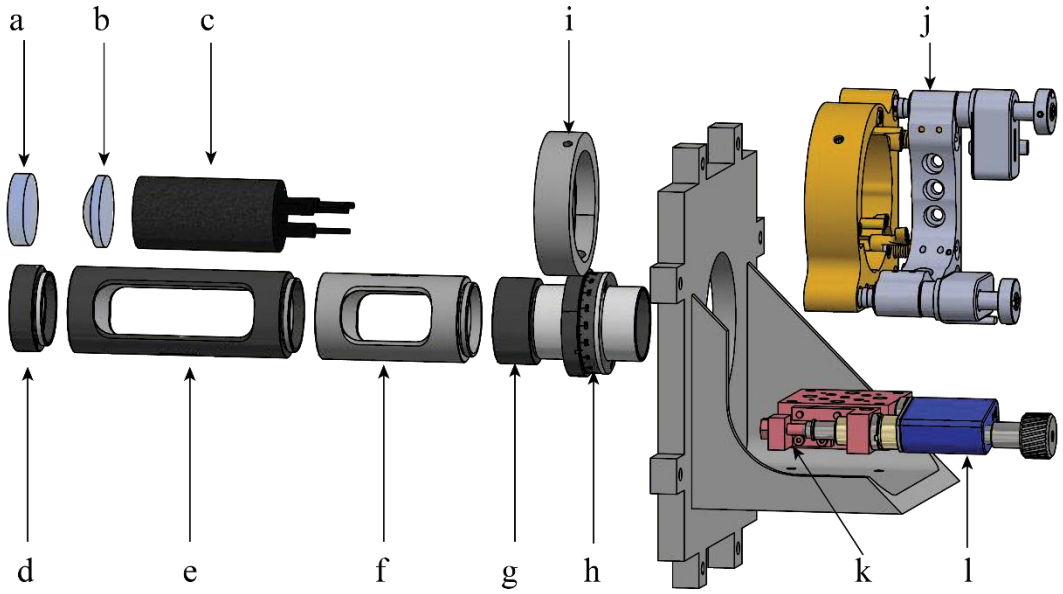

Figure A.7 Exploded view of optical assembly for THz-STM

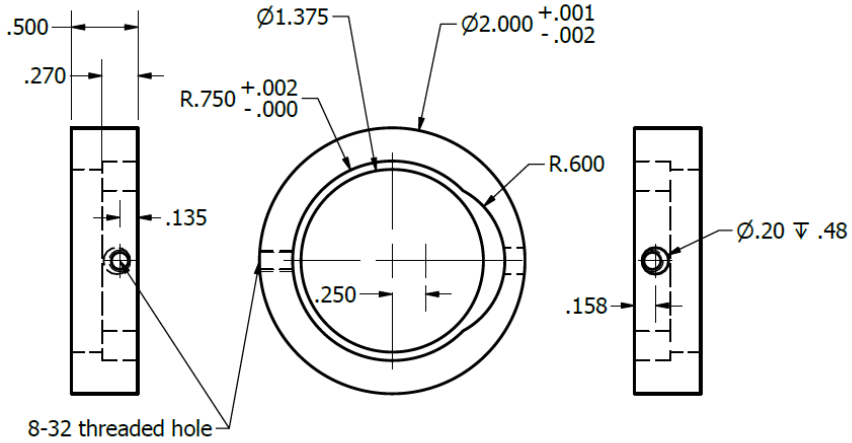

Figure A.8 Custom 1.5’ to 2” adapter for rotation mount

As of now, both piezo actuators on the optical mount (Newport 8822-AC) are replaced with closed-loop piezo actuators (PI N-472.210) for more reproducible alignment optimization.

The lens tube assembly shown in Figure A.7 can be switched between different configurations for different purposes (see **Figure A.9**), by replacing the 3-in lens tube segment. Refer to supporting information sections in Chapter 2 and 3 for detailed application of each assembly.

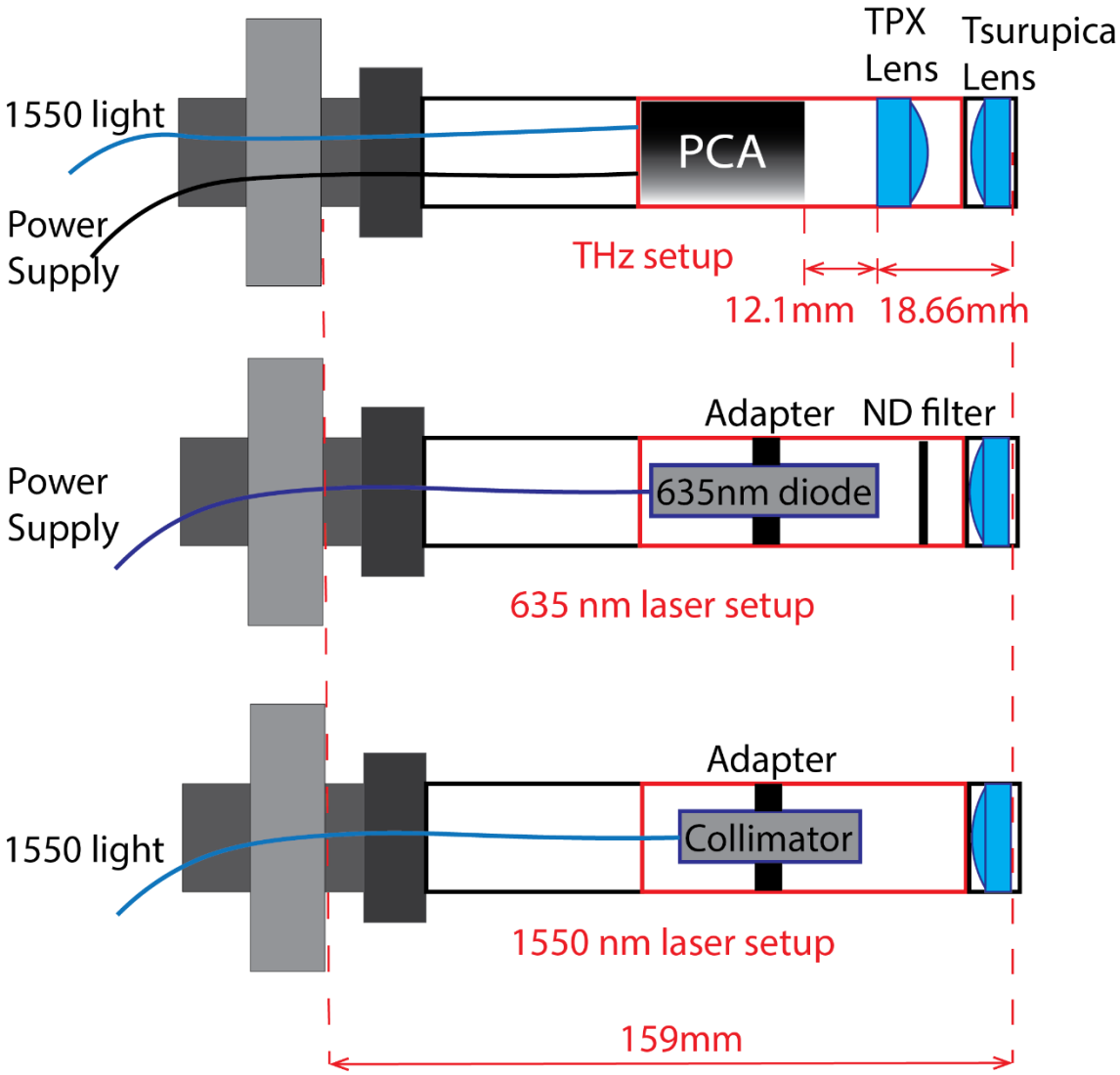

Figure A.9 Schematic for different types of lens tube assemblies

A.4 Scanner Shield Modification and Window Design

For the windows on the STM thermal shields, 1x1 inch, 2mm-thick, optically polished Tsurupica windows are used (Broadband Inc.). Bakeout temperature is kept below 100C to avoid heat-deformation of Tsurupica windows. Modifications were made to the STM scanner shields for optimized THz transmission aperture and good clearance of dosing holes.

Two different set of designs for scanner shield side plates and window frames were developed to accommodate the Tsurupica window in different orientations, one vertical window design (currently implemented) and one 45-degree tilted window design, Figure A.10 shows an overview of the 2 types of design.

The vertical window design includes inner shield and outer shield side plates (Figure A.11), window frames (Figure A.12) and window hoods (Figure A.13) that fix on the outer shield window frames. The window hood is designed to protect window from coating due to side dosing, heater outgassing and sample sputtering. A special shape for inner shield windows is required to avoid conflict with dosing holes (Figure A.14). Photos showing the optical path and dosing path clearance after assembling the new scanner shields with vertical window design is shown in Figure A.15.

The drawings for the 45-degree window design is displayed in **Figure A.16**-18.

Beside the window modification, the inner shield back plate and clamp screw housing door are also modified for better system performance, as shown in **Figure A.19**.

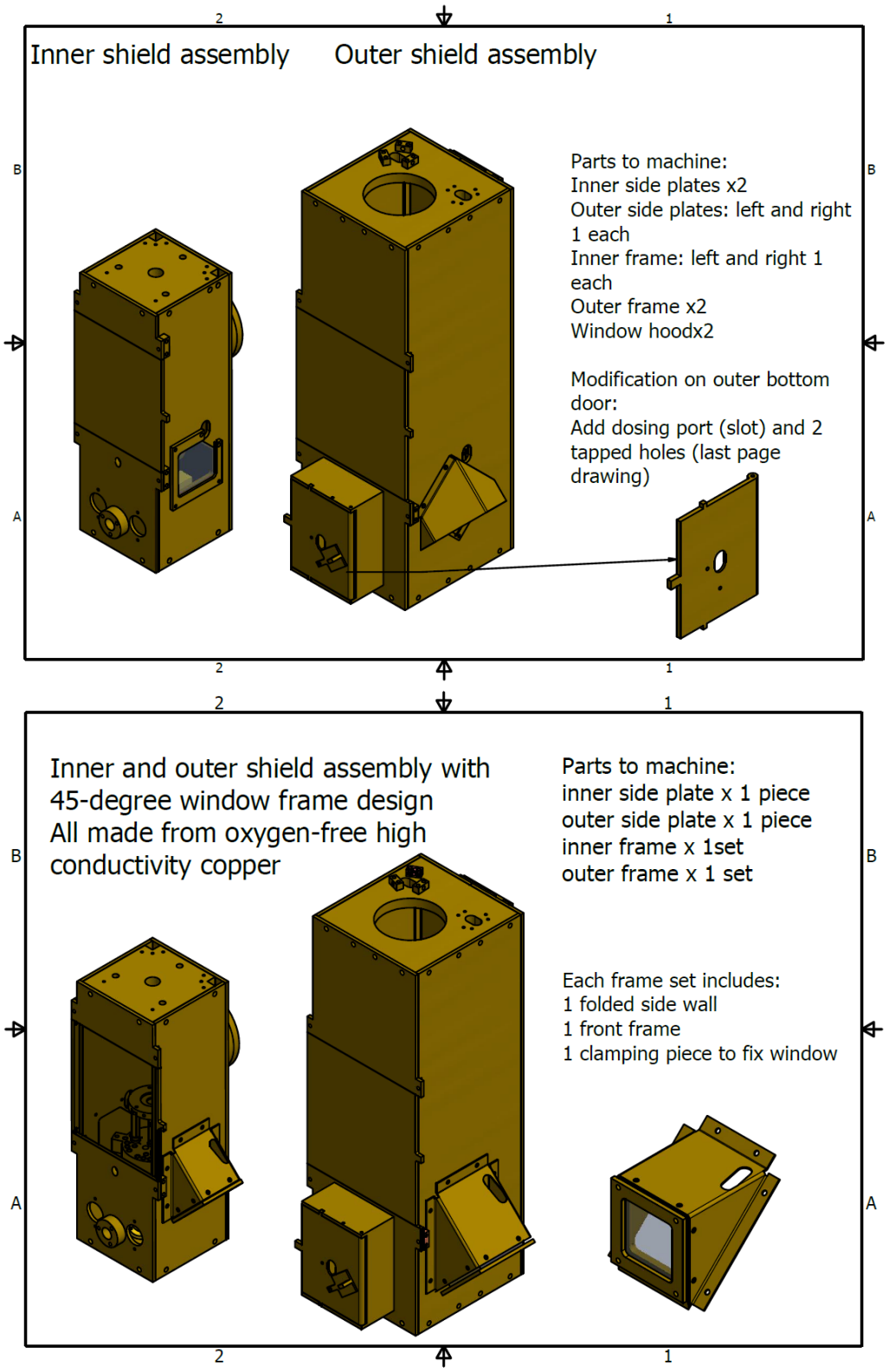

Figure A.10 Scanner shield assembly overview

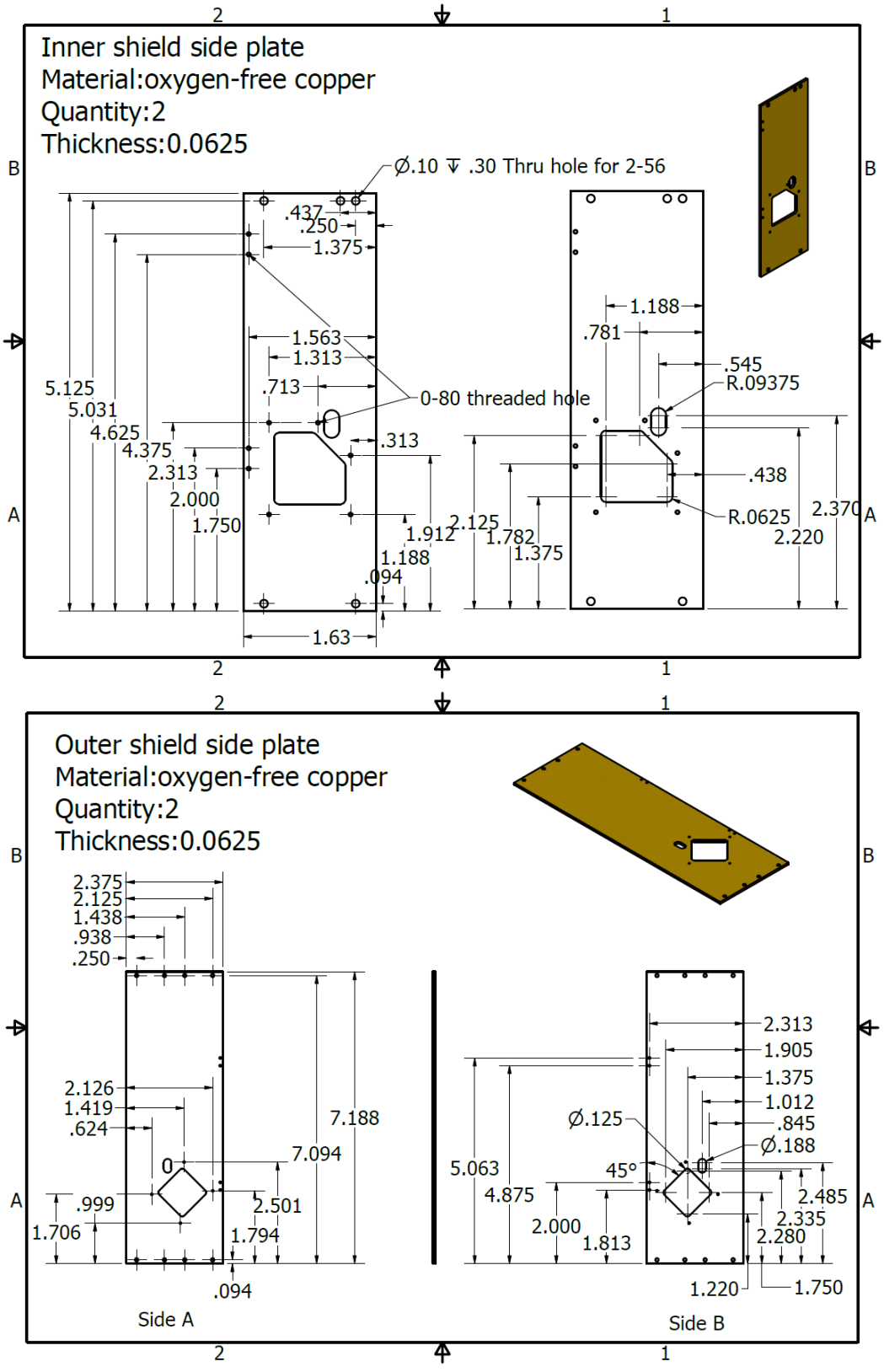

Figure A.11 Inner and outer side plates for vertical window design

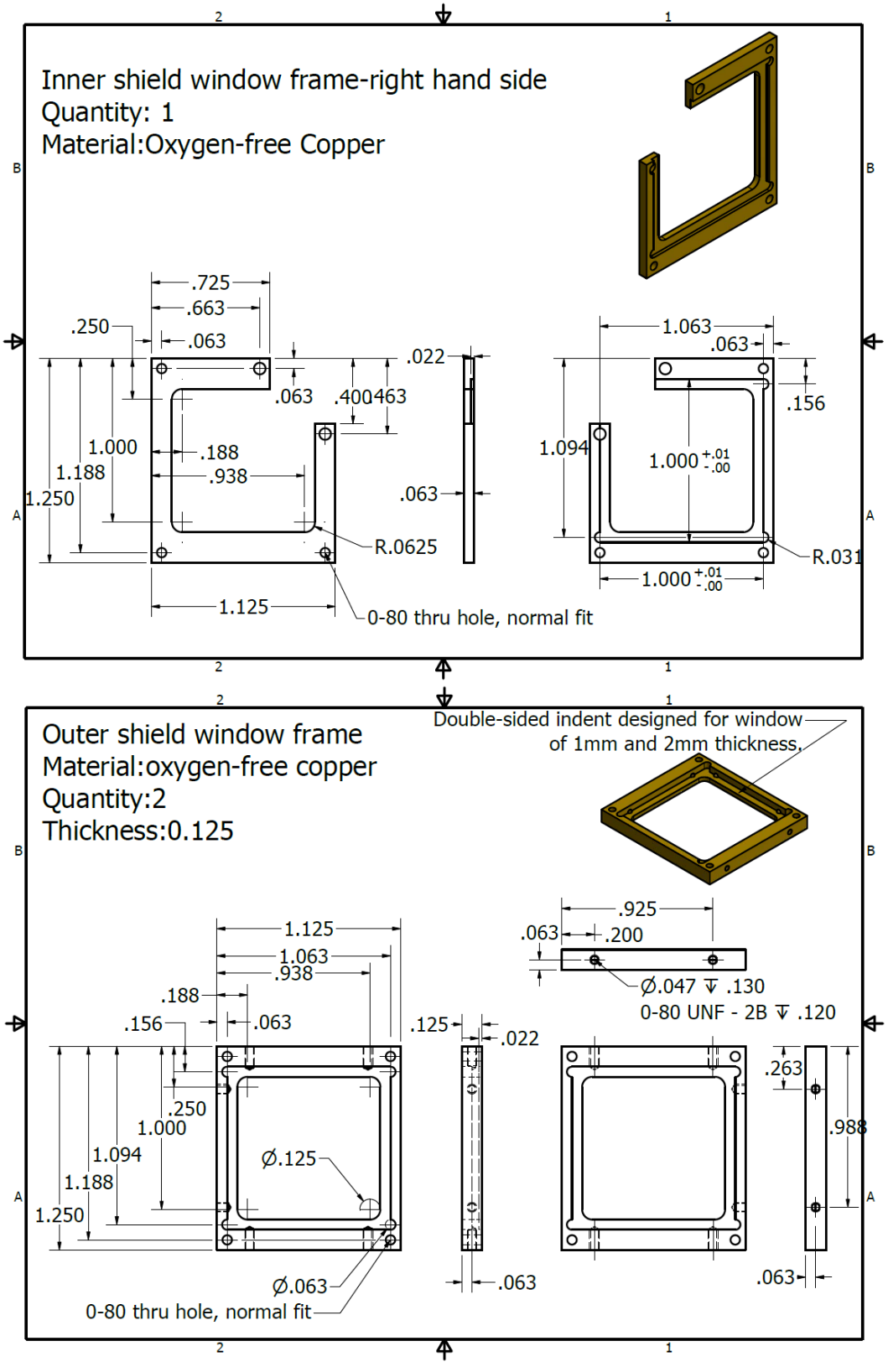

Figure A.12 Window frame design for vertical window

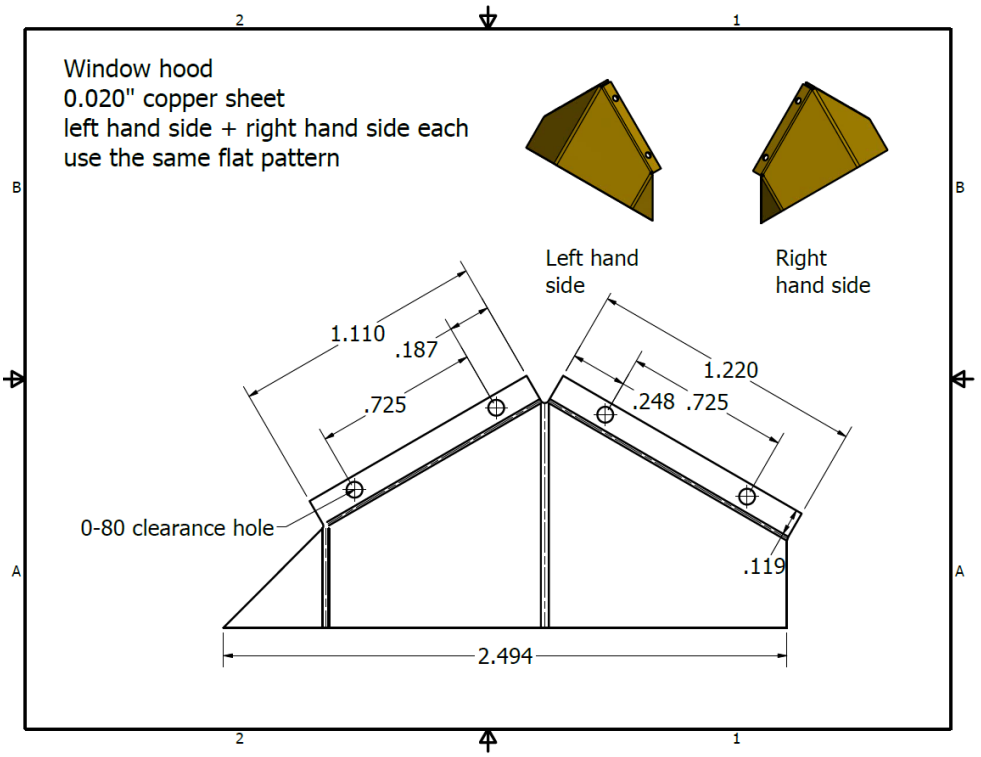

Figure A.13 Window hood for outer window

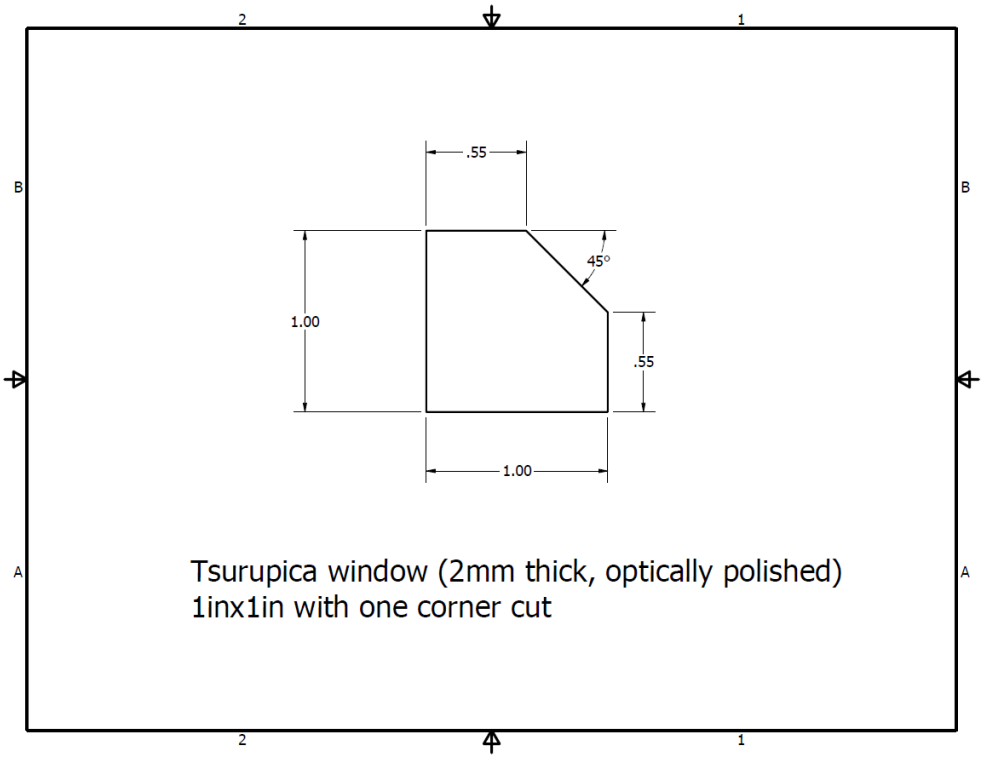

Figure A.14 Customized Tsurupica window shape for inner shield of vertical window design

Figure A.15 Photos showing THz/optical path clearance and dosing hole clearance on both side of scanner with updated shield design

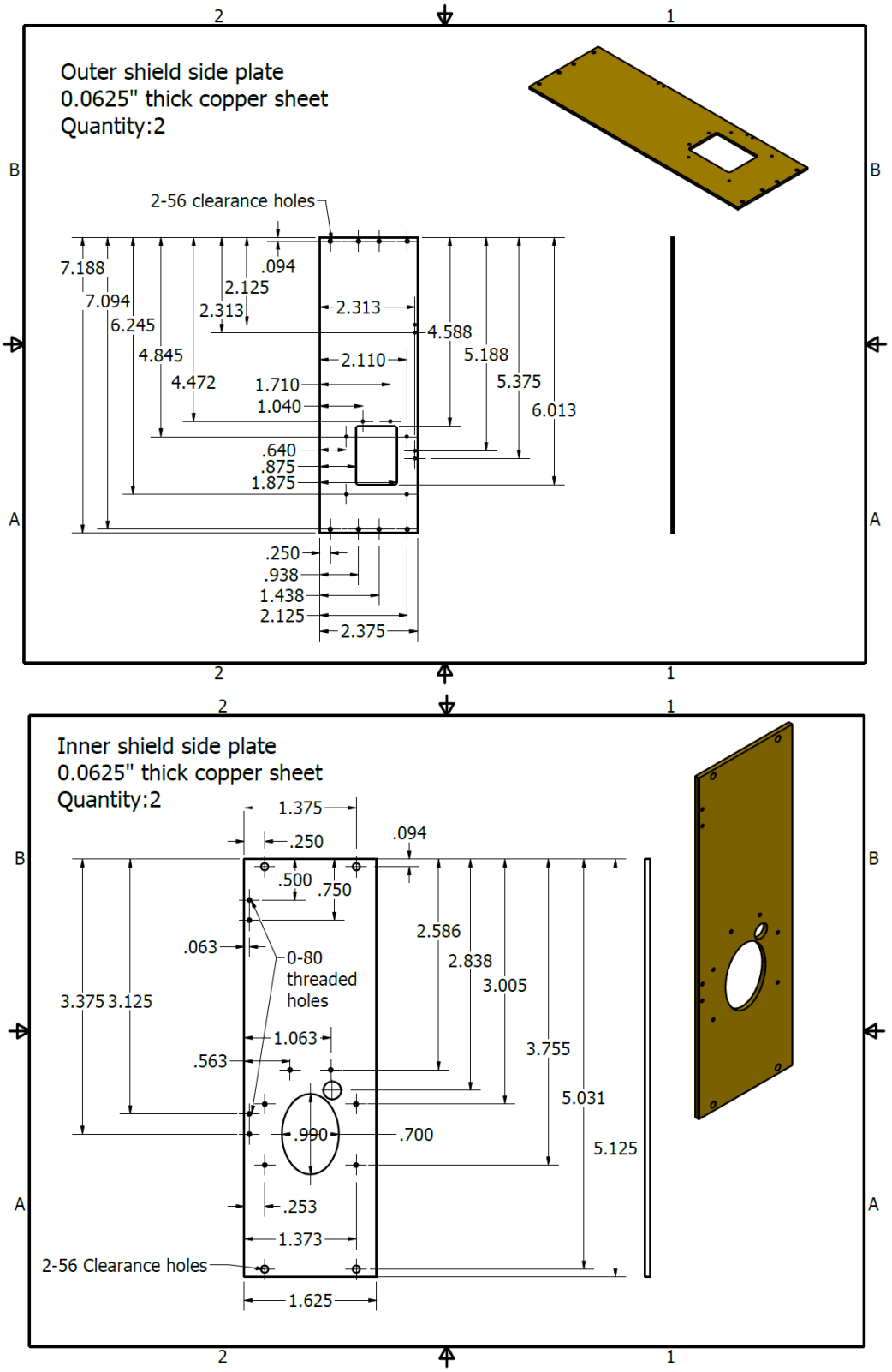

Figure A.16 Outer and inner shield side plates for 45-degree window design

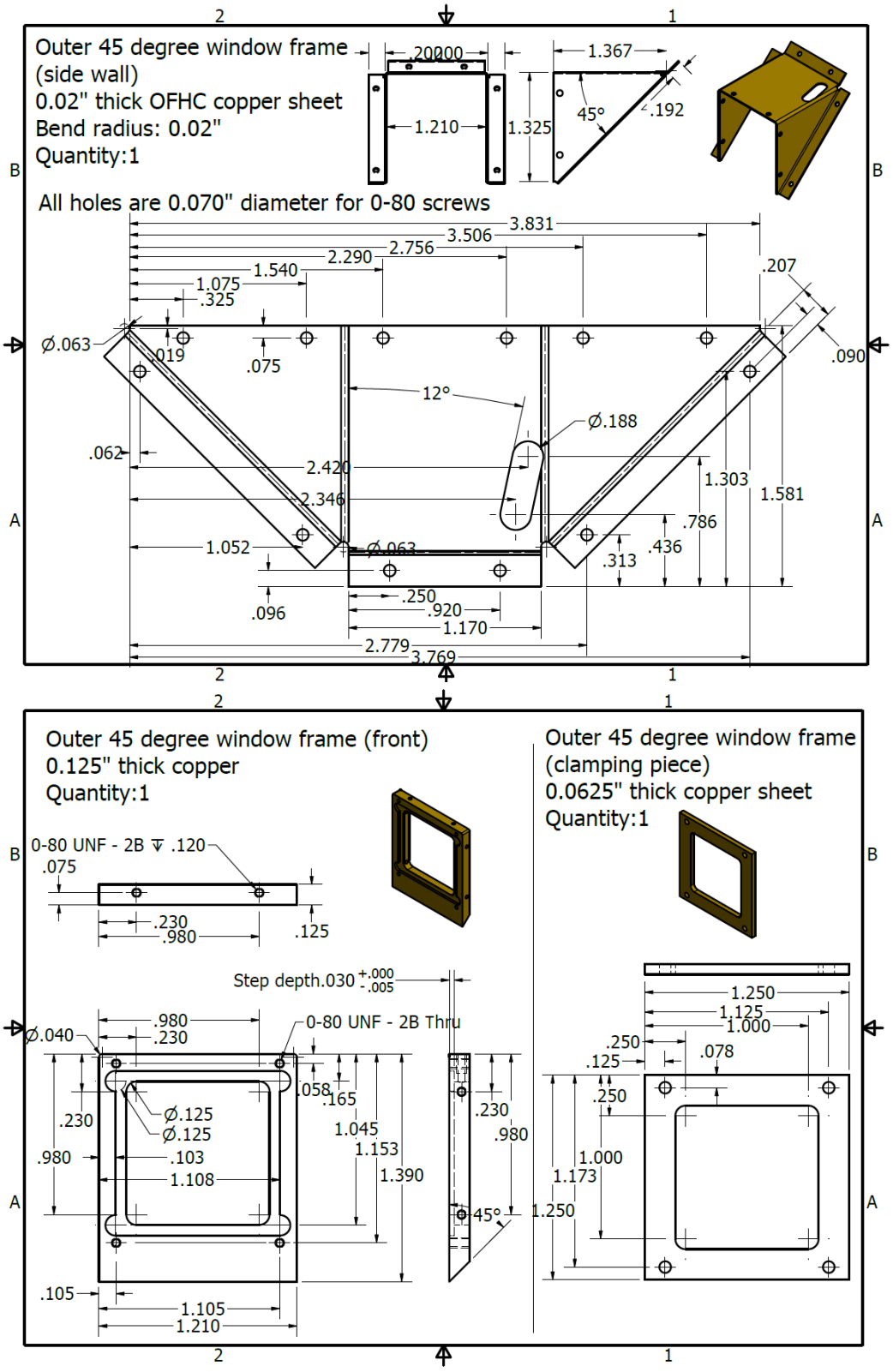

Figure A.17 Drawings of parts for 45-degree outer window frame

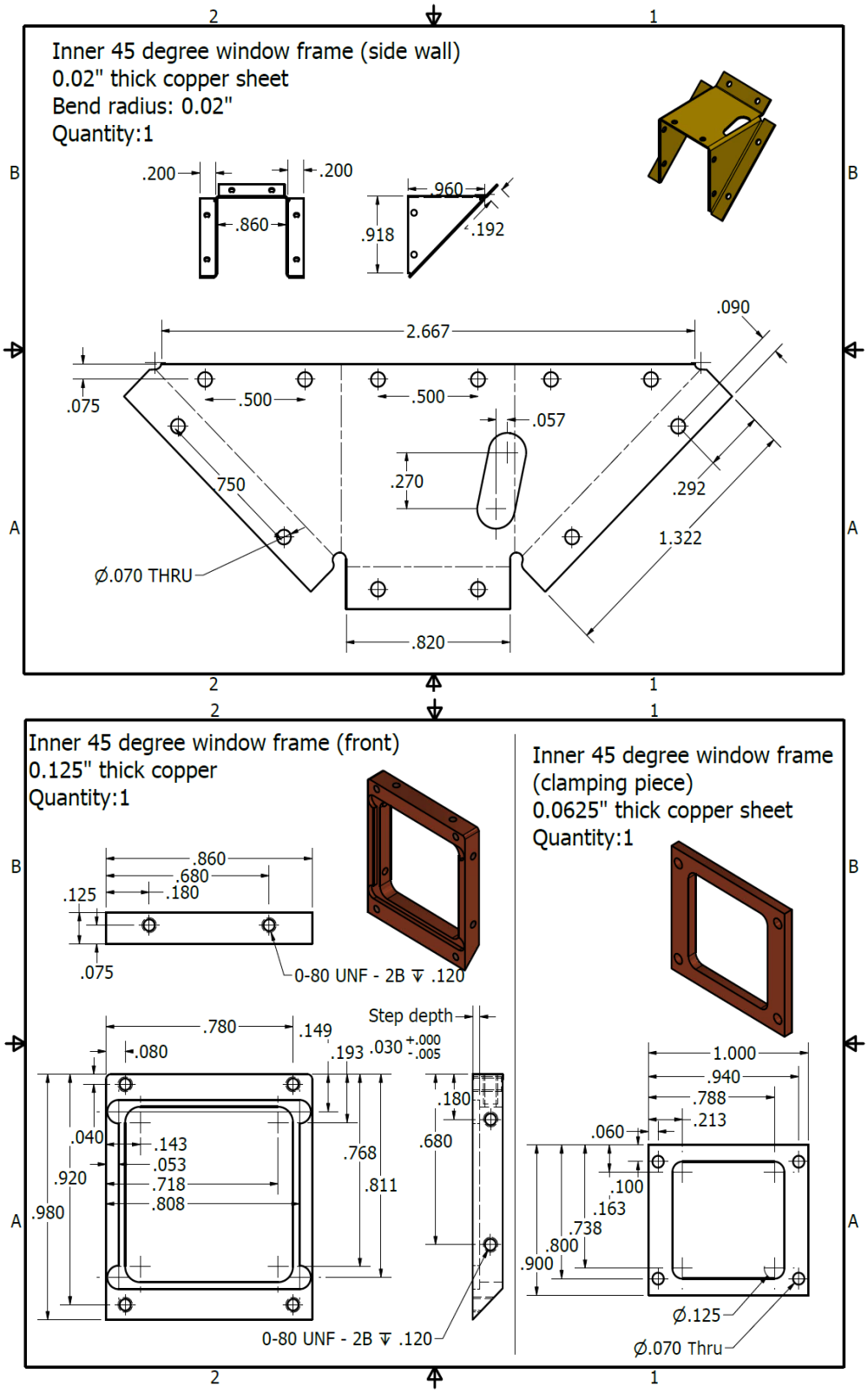

Figure A.18 Drawings of parts for 45-degree inner window frame

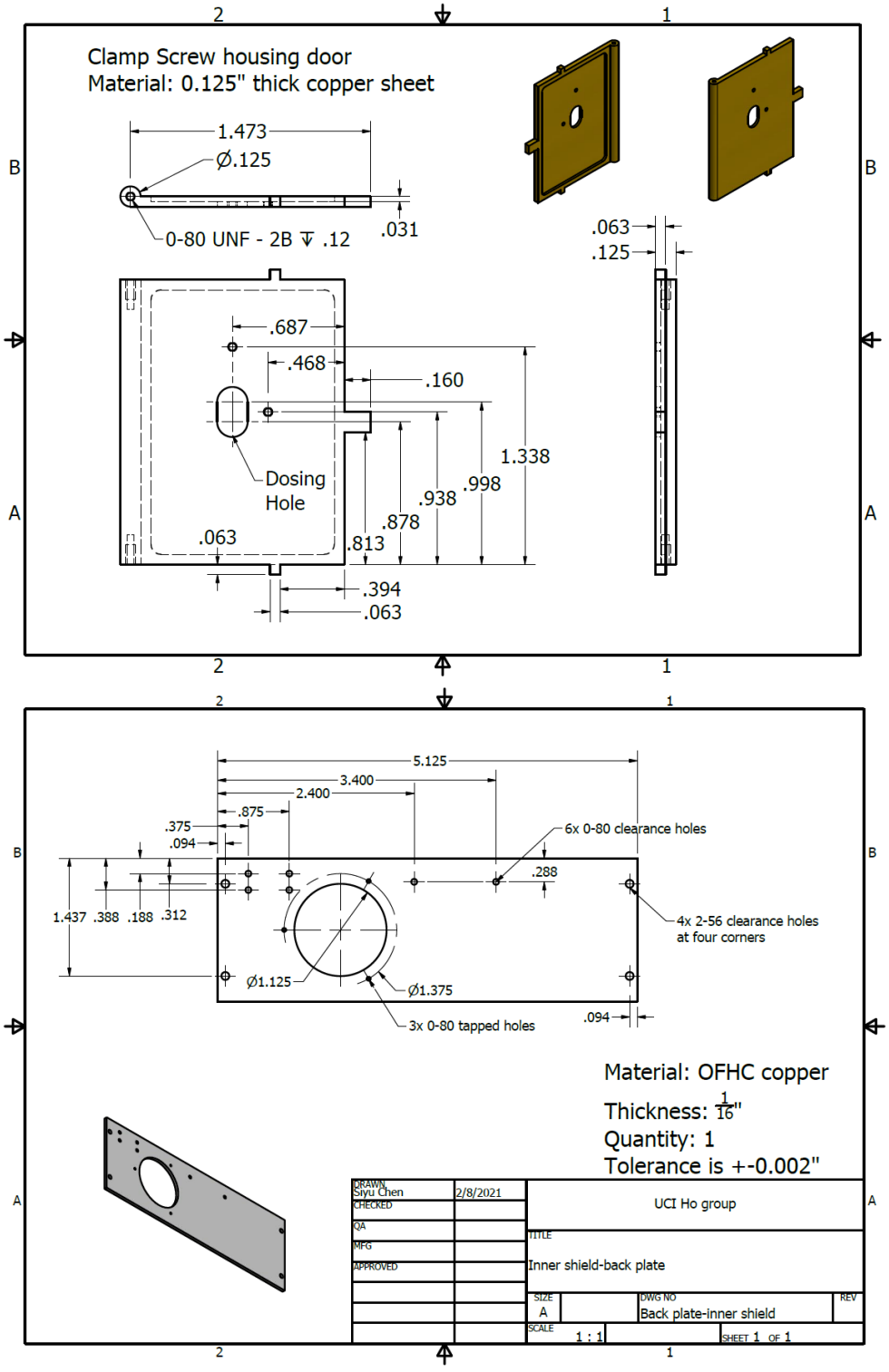

Figure A.19 Updated design for clamp screw housing door and inner back plate

Appendix B

Other Modifications to STM IV for Improved Performance

B.1 Improved Scanner Crosspiece and Reduced Mechanical Noise

As of 2019, STM IV has been suffering big mechanical noise at low temperature. After several rounds of troubleshooting, we found out the main reason to be the damping structure used by STM IV, with magnets mounted on inner shield plates and small copper plates on each side of the crosspiece (shown in Figure B.1). The small plate on each side of the crosspiece can induce strong Eddy damping current at low temperature, therefore overdamping the scanner. This overdamping effect leads to strong coupling of surrounding mechanical noise into the scanner baseplate and makes the tunneling junction very sensitive to talking sound. Besides, loose connection between the crosspiece and scanner base plate has previously caused a slow cooling speed due to poor thermal conductance. To avoid such problems in the future, we decided to switch to the classical damping structure with magnets mounted on the crosspiece and adapted the previous design into a one-piece design for better integrity (Figure B.2). Photos of the finished, gold-plated crosspiece assembled to the scanner baseplate is shown in Figure B.3.With the new vibration damping design, we achieved a much smaller mechanical noise (shown in Figure B.4), hence a much higher signal-to-noise ratio for imaging and spectroscopy.

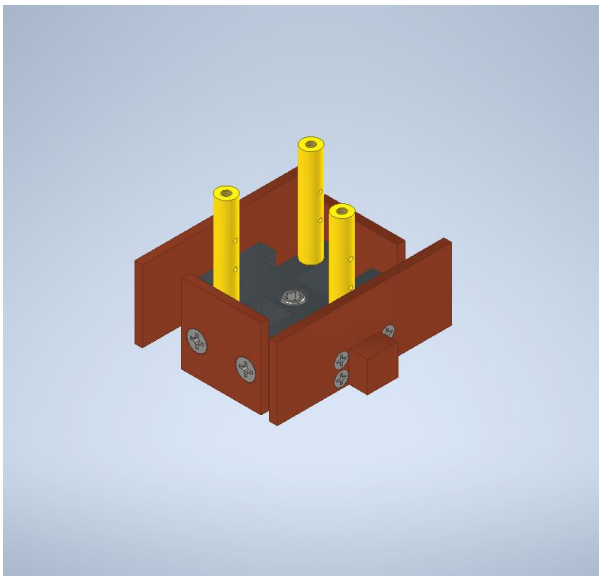

Figure B.1 The previous cross piece design

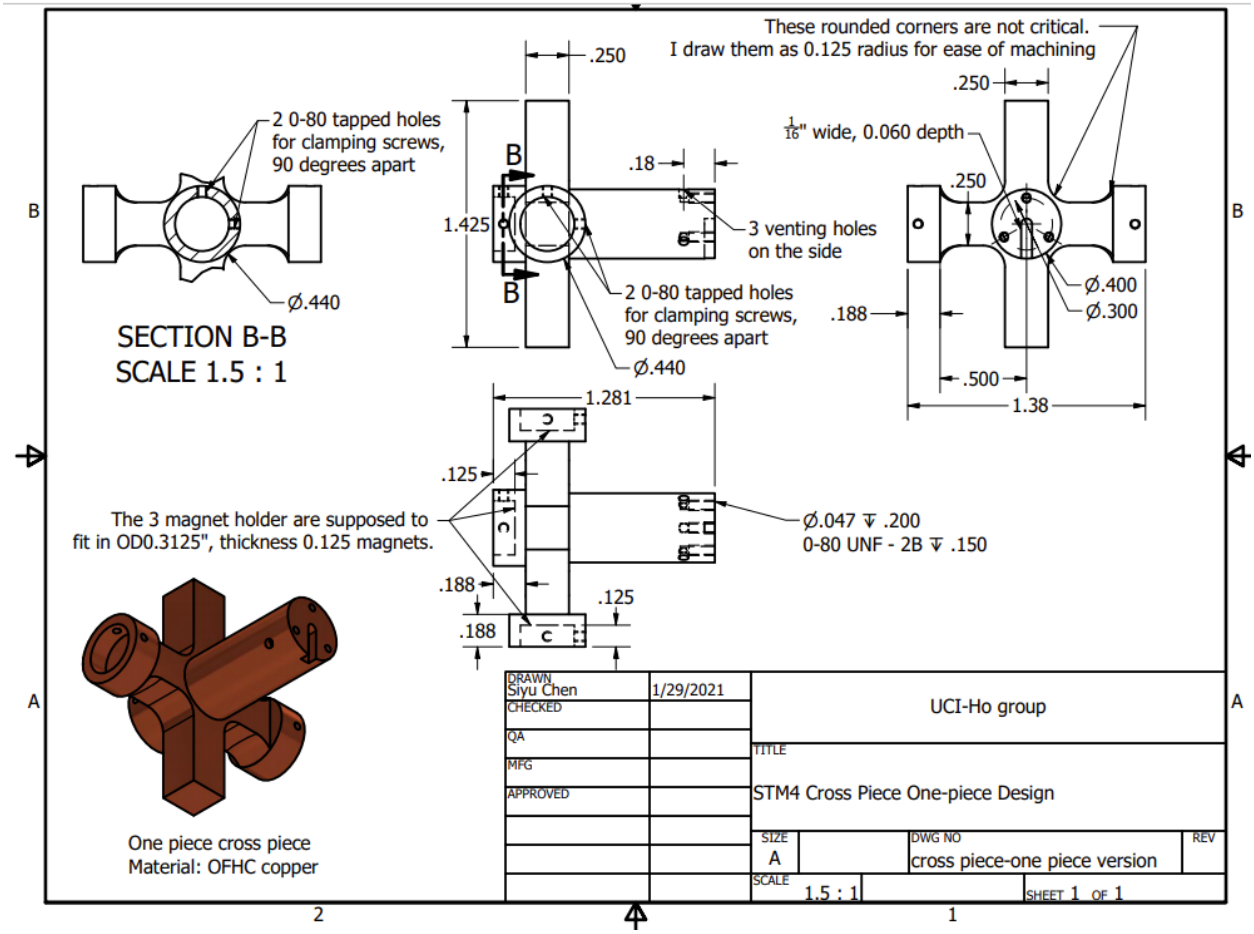

Figure B.2 Drawing of new one-piece deign for crosspiece

Figure B.3 Photos showing the new crosspiece mounted to scanner base plate.

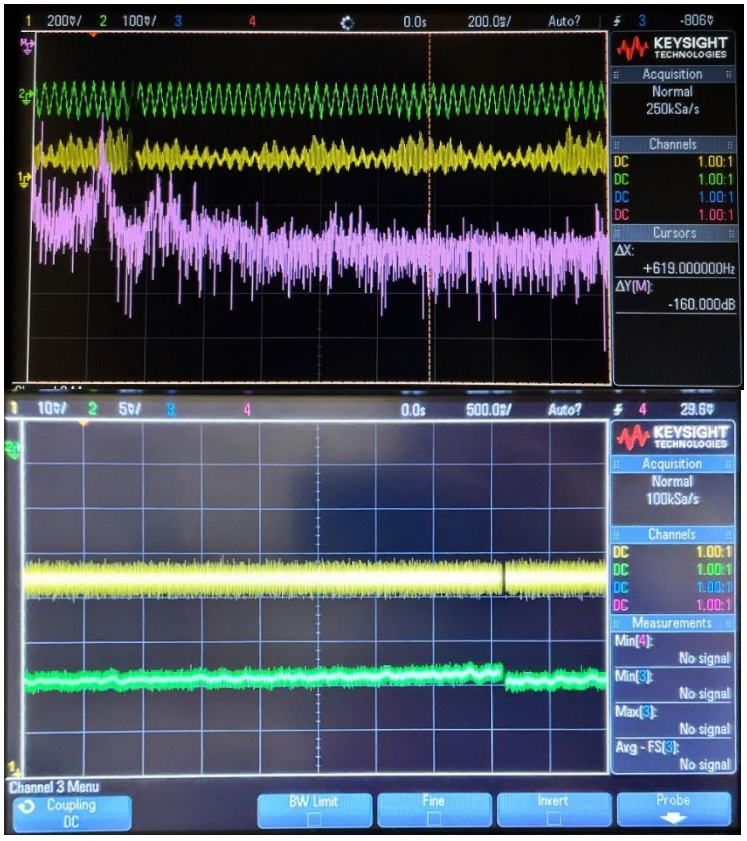

Figure B.4 Screenshot of oscilloscope showing the mechanical noise before (top) and after (bottom) switching to new damping method at 100mV/0.1nA with pre-amp at gain 9. Green is feedback Z and yellow is tunneling current.

B.2 Thermal Anchor Wires for Improved Cool Down Temperature

To further decrease the temperature of scanner at regular Helium consumption rate, we added 2 bundles of OD0.005” copper wires (Teflon coated) as thermal anchor wire to increase the thermal conductance. Each bundle consists of 10 wires, soldered to 2 pieces of copper foil that are attached to top plate of inner shield and the scanner base plate respectively (shown in Figure B.5). With the thermal anchor wire bundles, we have improved the baseplate cool-down temperature at regular Helium consumption rate (~30L/day) to below 8K from the previous 14K.

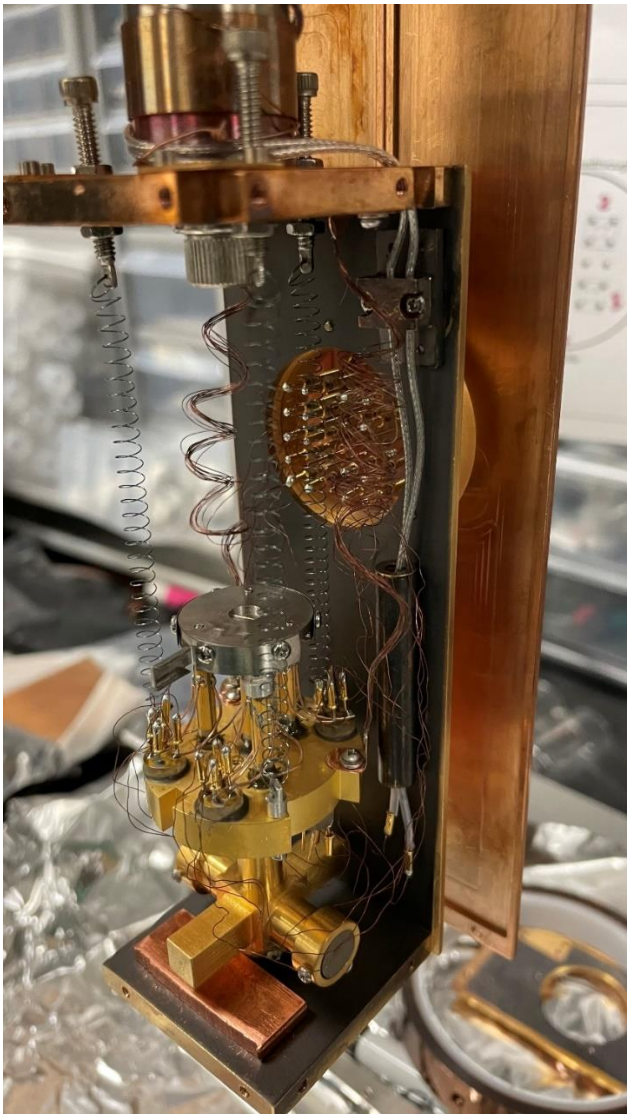

Figure B.5 The STM scanner assembly with thermal anchor wire just mounted

B.3 New Wobble Stick Pincer Design

To improve the structure stability and ease of use for the wobble stick, an improved version for wobble stick is designed. The design consists of 2 pincer arms pivoted around 2 axles each, and a center shaft restricted by a coaxial anchoring ring to provide stable operation (Figure B.6). All hinge axles are now stainless dowel pins fixed on both ends with clip-on retaining rings (McMaster Carr P/N 98408A116) for easy assembling (Figure B.7). Other than the overall structure improvement, the gripping force conversion efficiency is also shown to be improved significantly compared with the old design (shown in Figure B.8). The annotated drawings are displayed in Figure B.9 to Figure B.*15*.

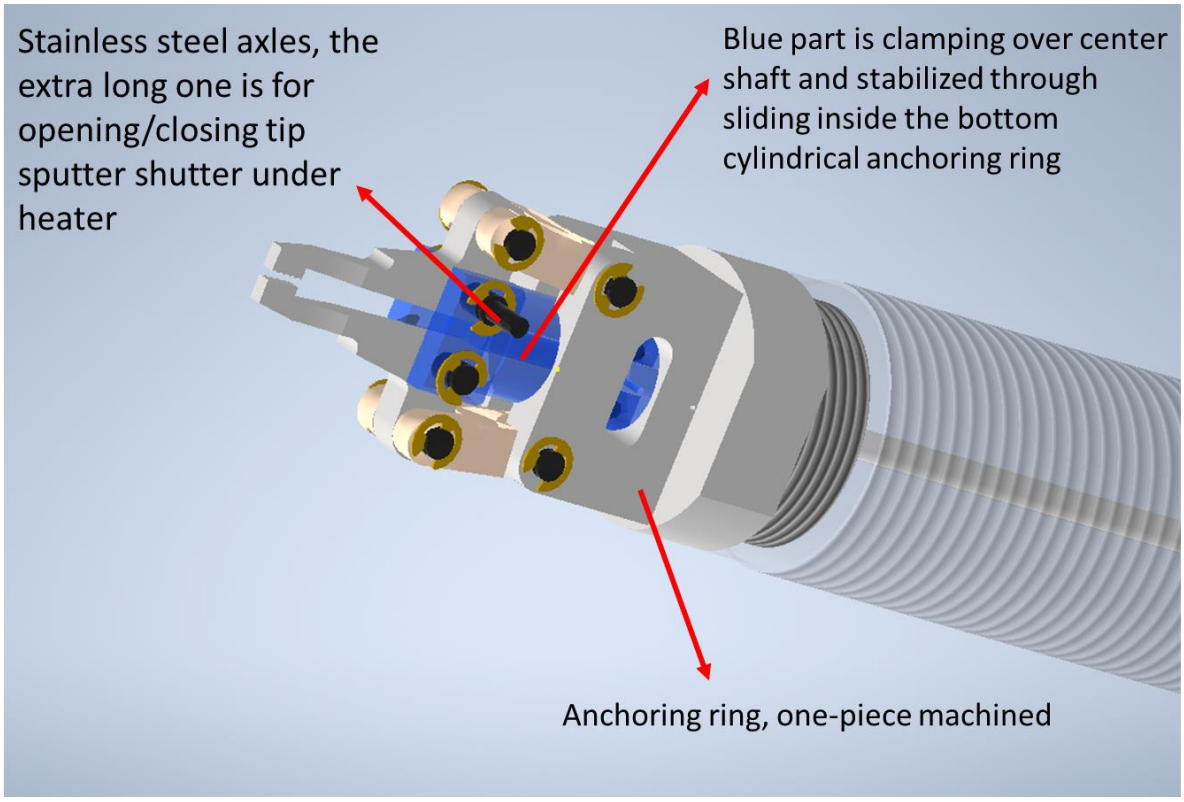

Figure B.6 Highlights of new wobble stick pincer head design

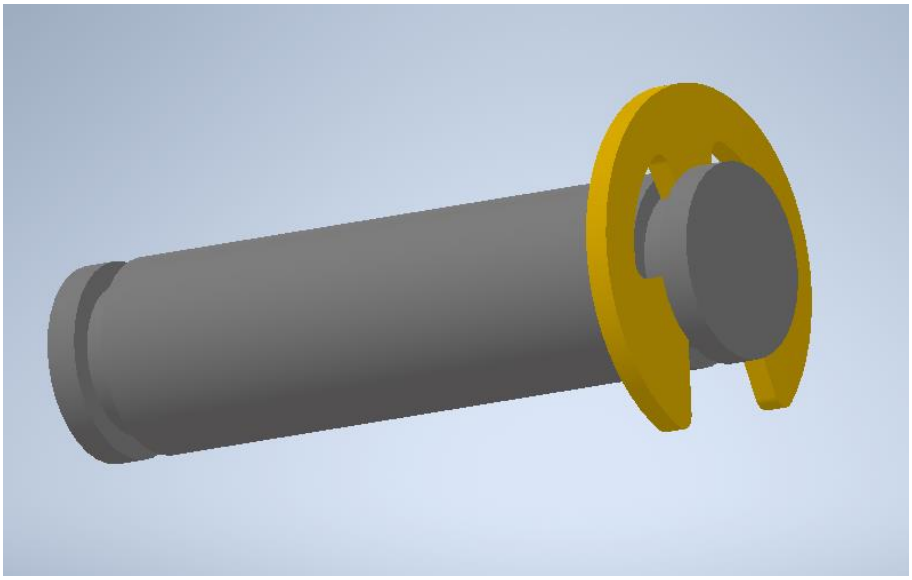

Figure B.7 A dowel pin axle with retainer ring mounted on one end

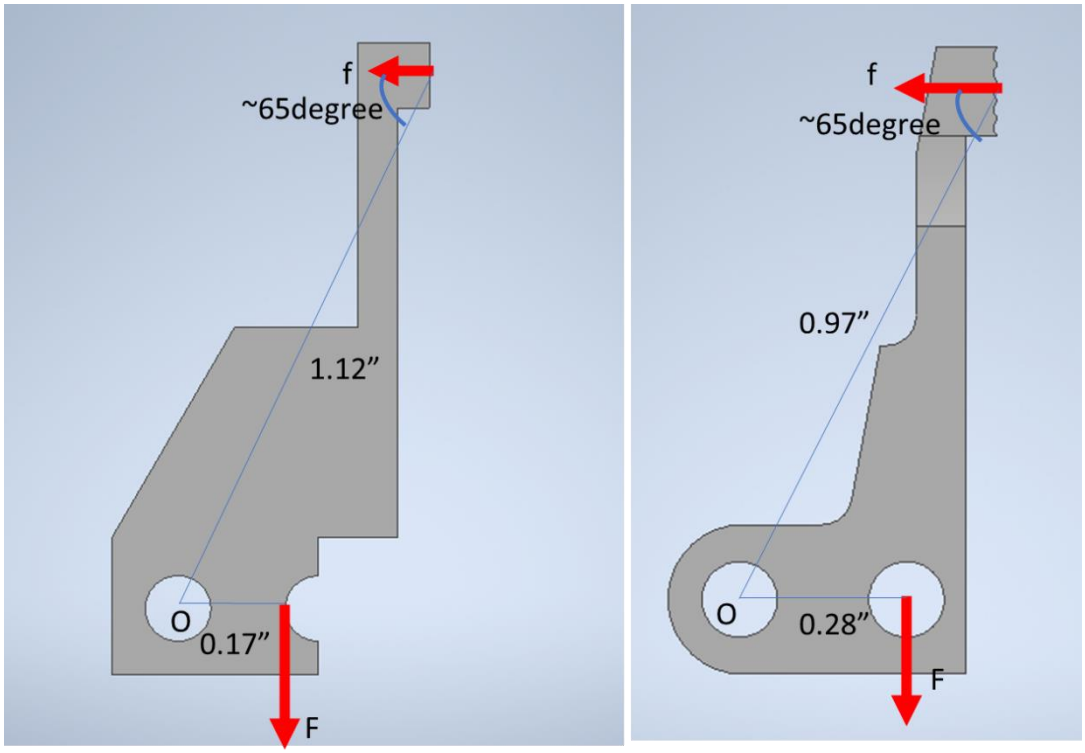

$0.17"\times F=1.12"\times f\times sin65$
$F/f=6.01$

$0.28"\times F=0.97"\times f\times sin65$
$F/f=3.16$

Figure B.8 Comparison of gripping force conversion efficiency between old (left) and new (right) design

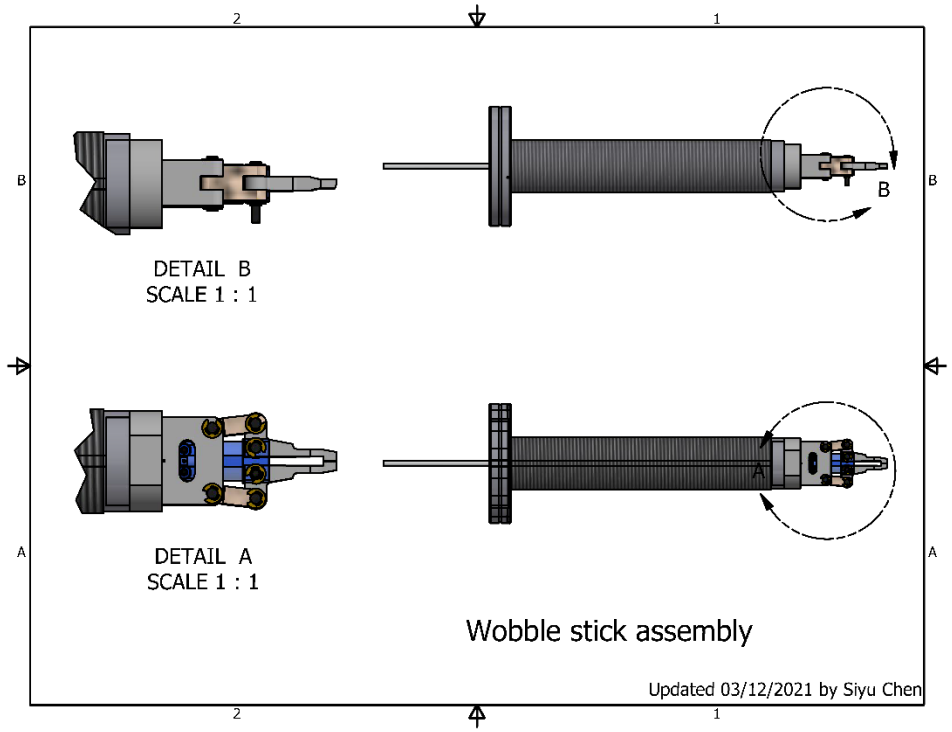

Figure B.9 Wobble stick pincer head - overview

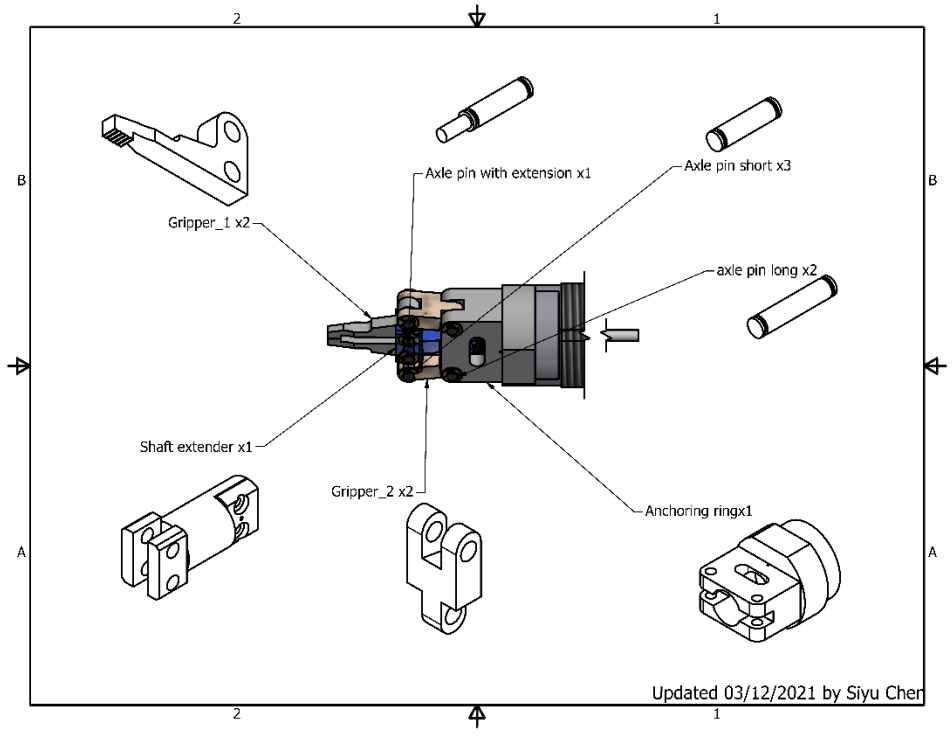

Figure B.10 Wobble stick pincer head - part list

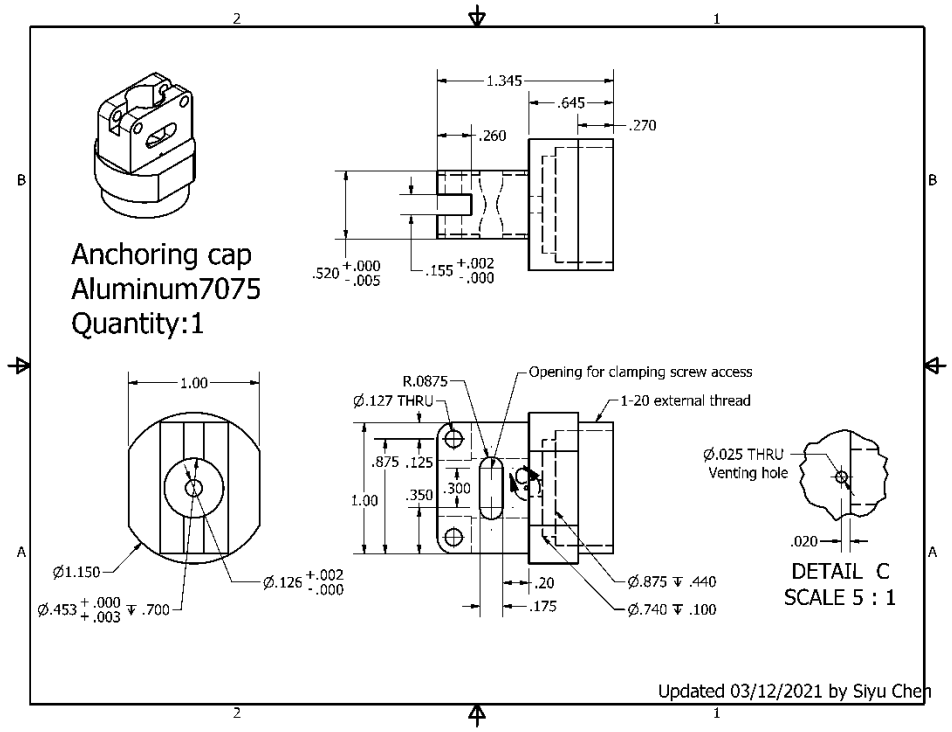

Figure B.11 Wobble stick pincer head - anchoring cap

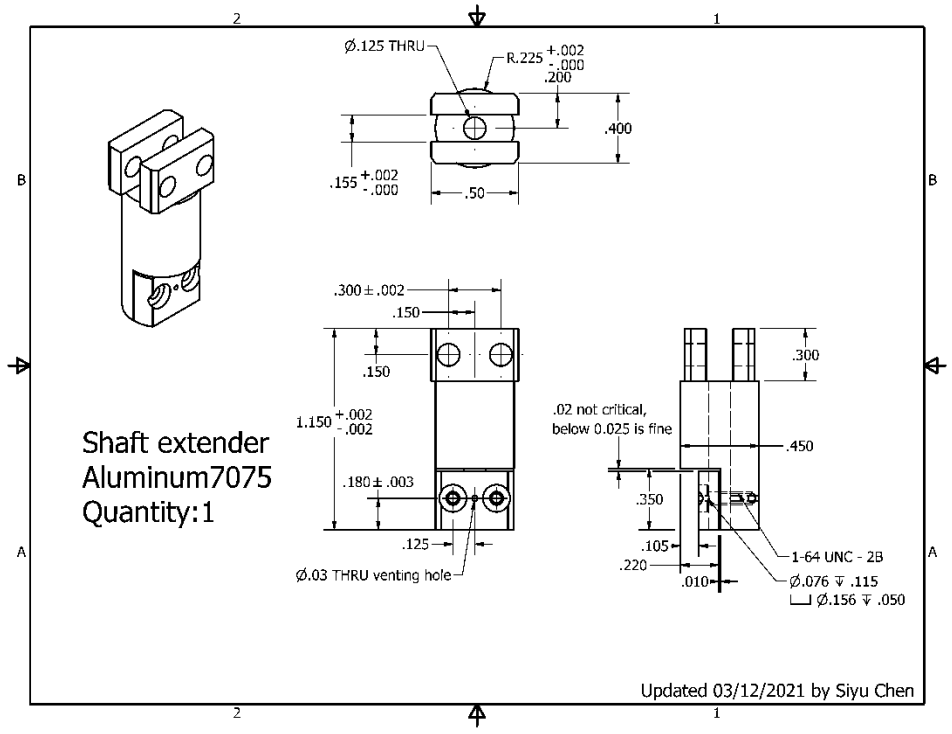

Figure B.12 Wobble stick pincer head - shaft extender

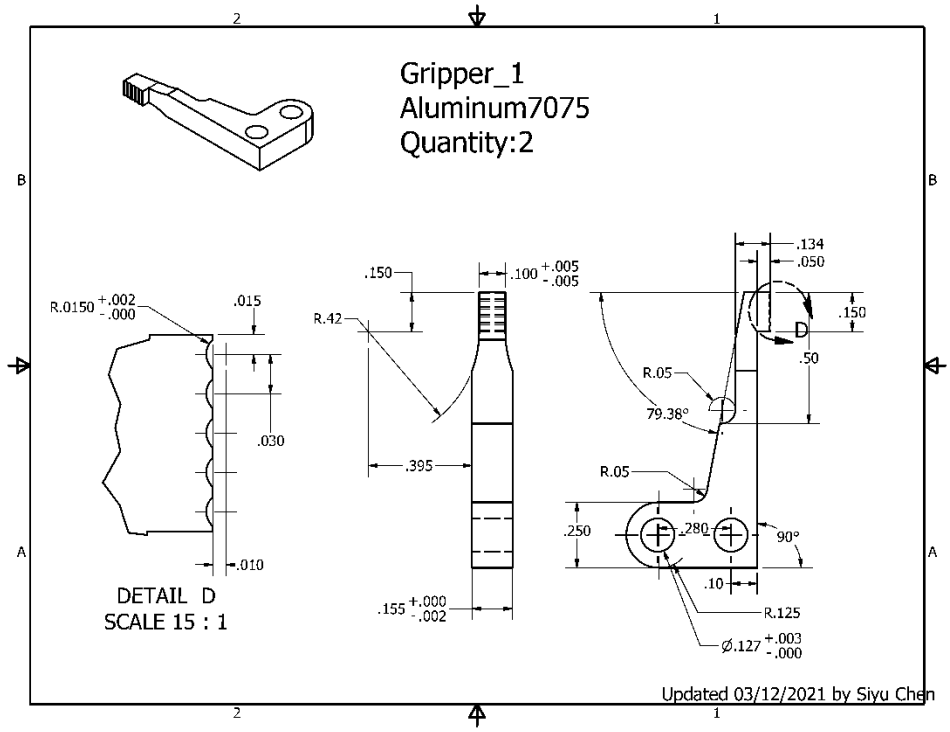

Figure B.13 Wobble stick pincer head – gripper arm 1

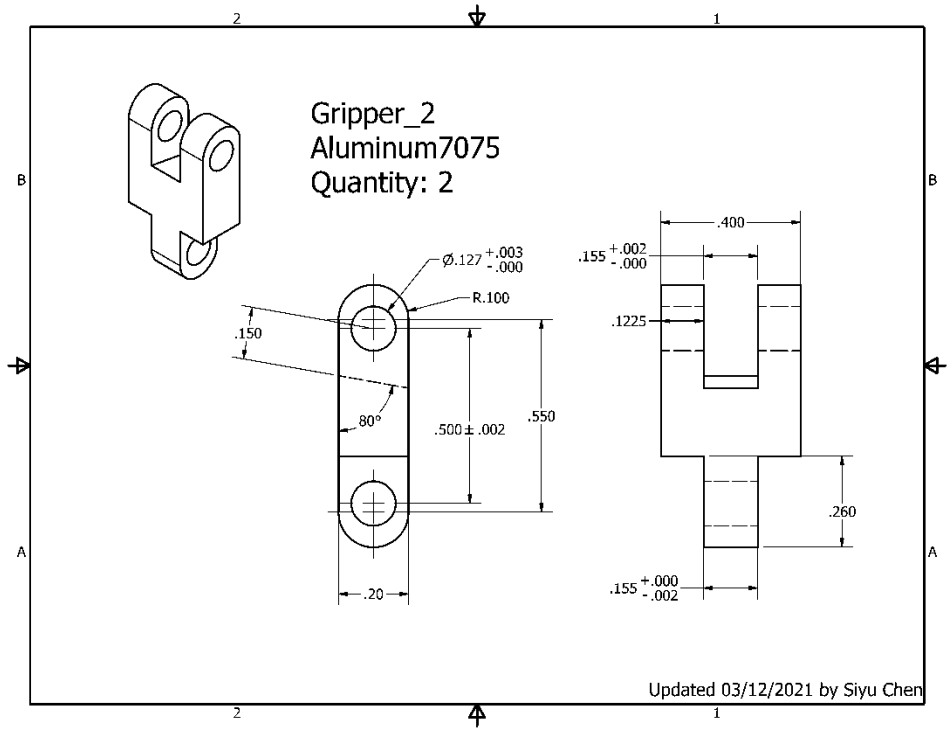

Figure B.14 Wobble stick pincer head – gripper arm 2

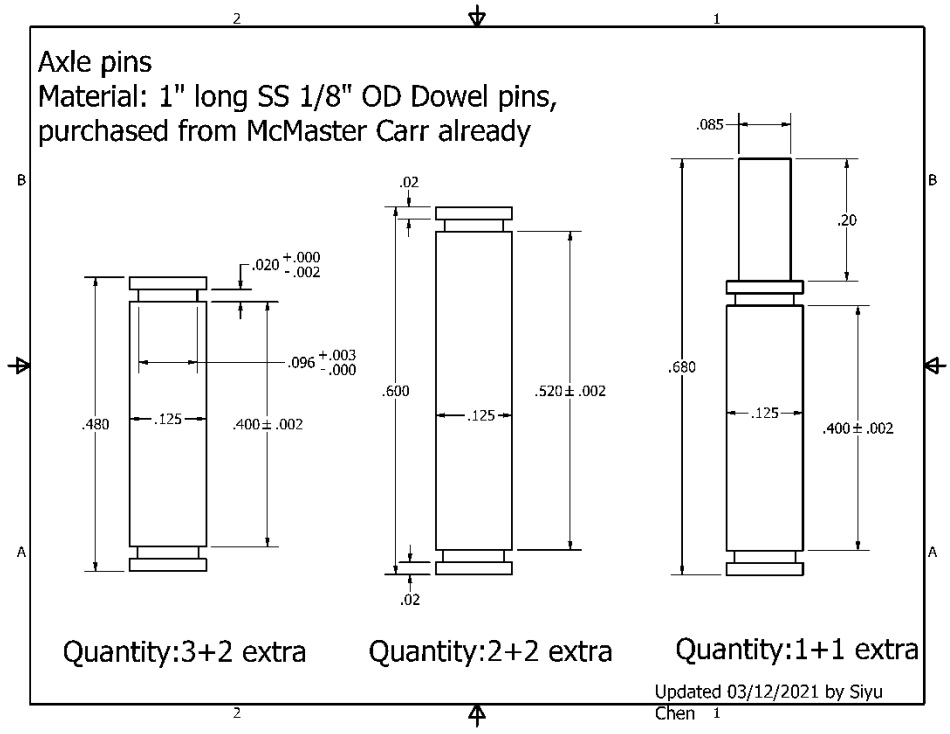

Figure B.15 Wobble stick pincer head – axle pins

Appendix C

Instrumental Challenges, Solutions and Cautions

C.1 Offset in R Spectra Caused by Ground Mixing

The electrical connections of our STM system started with Setup 1 shown in Figure C.1. At 400GHz THz emission, an offset of ~40% (at 1mV SEN) is observed for the THz Rectification signal. The offset gets bigger (~100%, see Figure C.2) when the shield of BNC connector for PCA is shorted to STM table. The offset in Rectification signal is not observed when tip is retracted, which means the signal is leaked in through the tunneling junction. The magenta arrows in the Figure C.1 shows the possible grounding loop that caused the offset signal. When PCA is connected to the PCA chopper receives a square-wave voltage signal, the large oscillating current in the PCA Line induces a corresponding oscillating potential in the ground line as well, this oscillation can be transmitted through the DAC Box to the bias dither input, and therefore affecting the bias and tunneling current output that eventually feeds back to lock-in amplifier. This oscillation shares the same frequency as the chopping frequency, therefore when it's leaked to the lock-in amplifier through the ground loop, first harmonic will give a big offset signal.

To solve the problem, we need to isolate the PCA chopper box and its power supply from the clean ground so that we can cut off any path that can leak the PCA-induced potential oscillation back to clean ground. We now use a finalized setup (Setup 4) as shown in Figure C.3. We combine the power supply for STM with the external DAC box. As there's no large current load from DAC box itself, the ground mixing here doesn't cause any spurious signal for lock-in detection. We then use power supply 2 solely for the PCA chopper to supply the PCA and put it on normal power with an isolated ground (the ground line is not connected to power ground). This entire isolated ground

part is indicated using black boxes in Figure C.3. This isolated ground will still be connected clean ground when TTL is connected to PCA chopper, however, there's no other path for the potential oscillation to be leaked back to clean ground, therefore no offset is observed in rectification signal.

For the actual troubleshooting process, we started with switching to Setup 2 (shown in Figure C.4) by isolating the power supply 2 from clean ground, which turned out to be equivalent to setup 1. As shown in the Setup 2, the dash-boxed part is connected to clean ground when the lock-in TTL output is connected to PCA chopper box. With this setup, we also found that the offset is almost gone when DAC box output is disconnected from STM bias dither input. Therefore, we thought isolating the DAC-to-STM path would block the ground loop. However, we found that, with a ground isolator on the DAC-to-STM path, offset in rectification is even bigger (almost twice as big), while putting the isolator on the TTL line can reduce the offset signal to ~20% (as shown in Figure C.5), but it still does not completely resolve the issue. Based on the discussion with setup 1, it's likely that isolating TTL line can largely reduce the coupling between PCA chopper ground and clean ground, but the DAC-to-STM path still mixes the clean ground with the PCA chopper ground.

We also tested the offset signal using setup 3 (Figure C.6) where DAC box is put on isolated ground while PCA chopper is still on clean ground. The testing results (shown in Table C.1) indicate that no matter DAC is connected to STM bias dither input or not, we will always have offset in rectification signal as along as PCA is connected to the PCA chopper and chopping signal is on. This type of behavior is also consistent with the discussion for Setup 1, except that for setup 3, the signal offset is less strong (~28%,1mVSEN) and leaks through the connection of power supply 2 that's directly on clean ground. Learning the fact that high current load on PCA chopper

is the source of the signal offset, we eventually changed to the setup 4 mention above, which eliminated the signal offset problem.

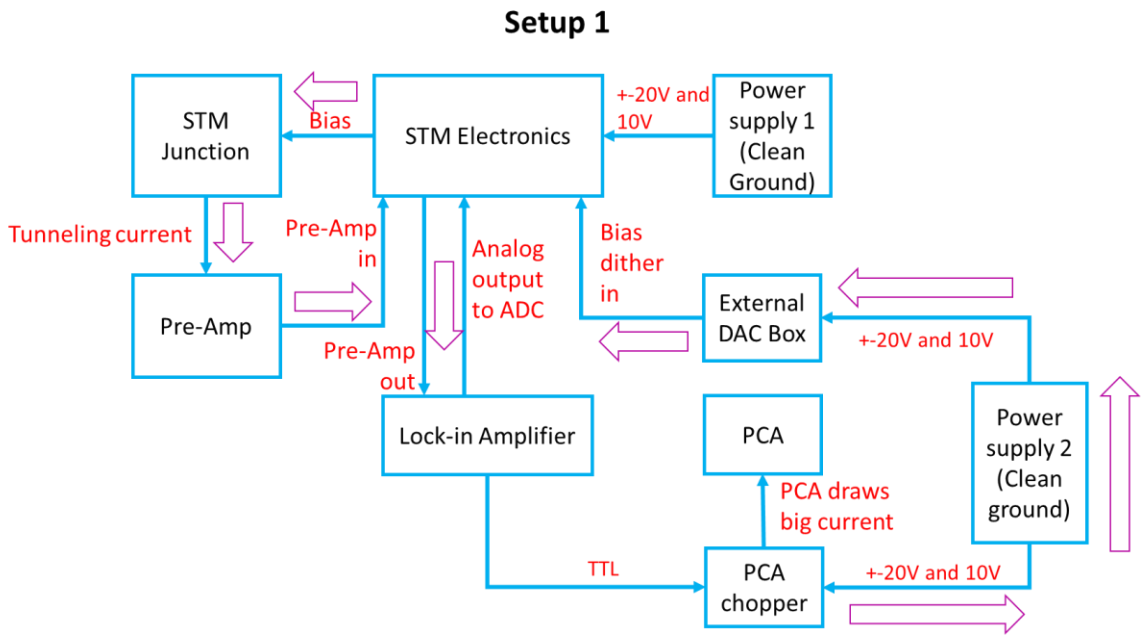

Figure C.1 Schematic of setup 1

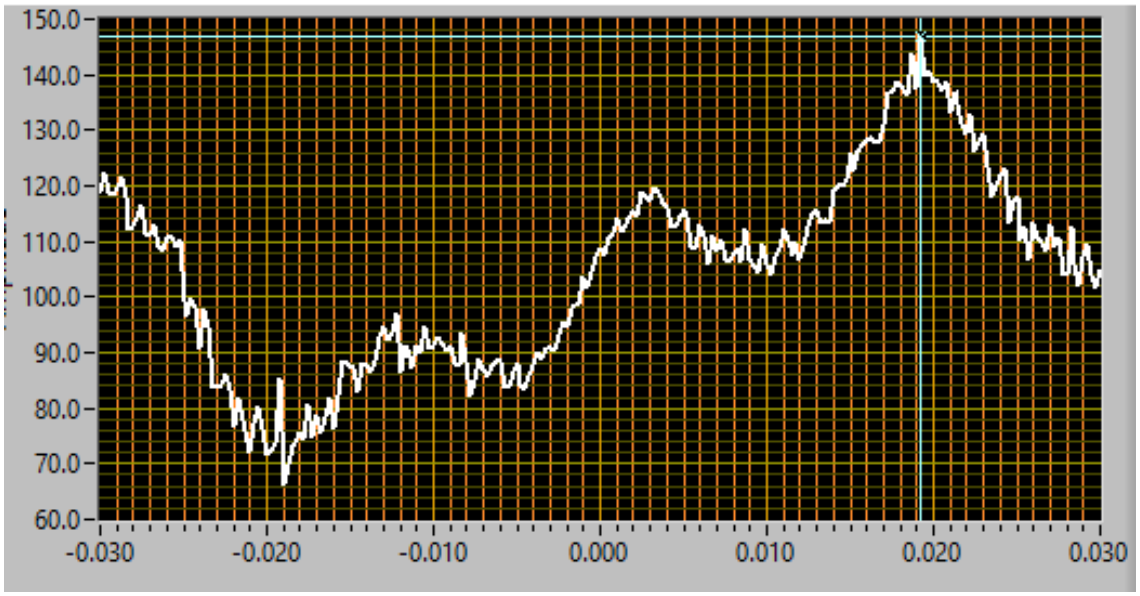

Figure C.2 R spectra of CO with big offset

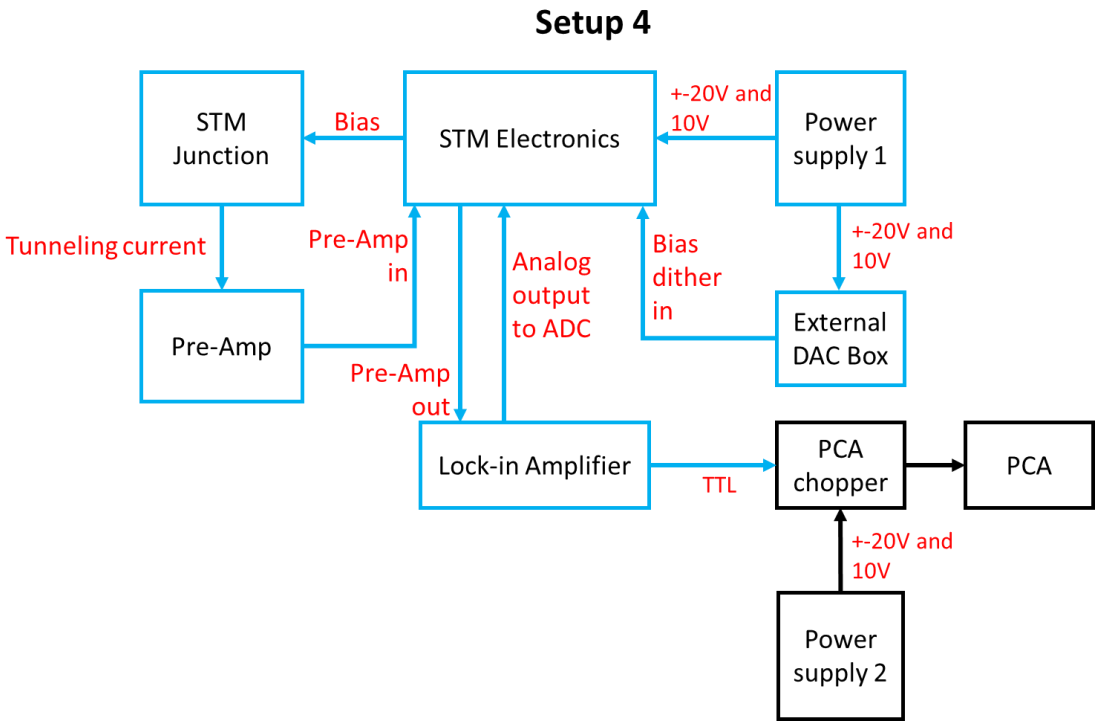

Figure C.3 Finalized schematic for electrical setup

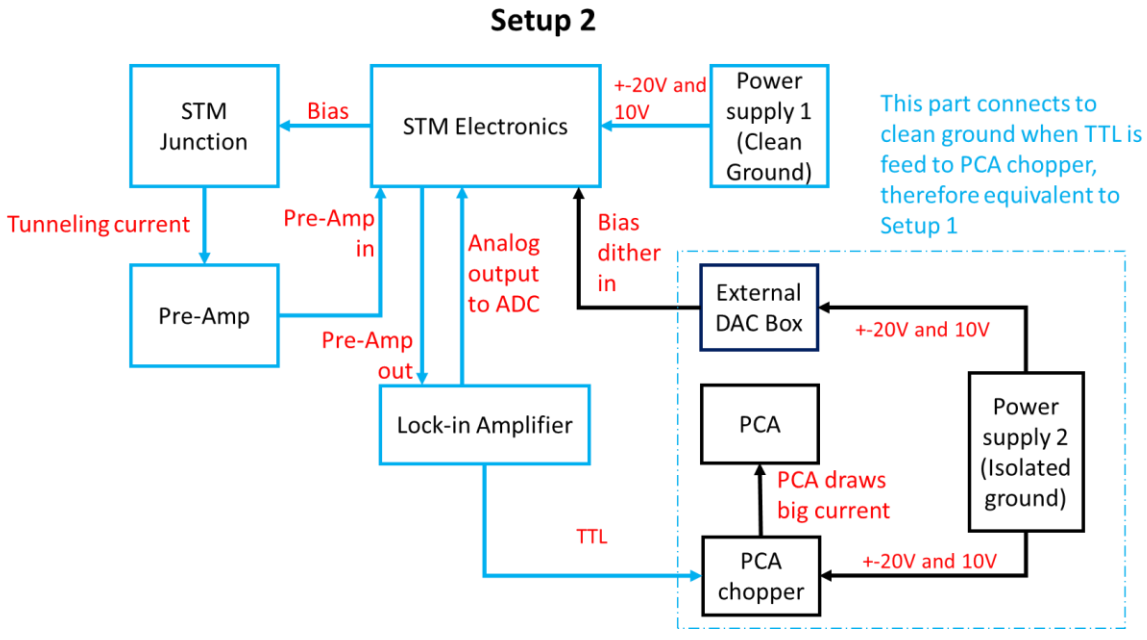

Figure C.4 Electrical connection scheme of setup 2

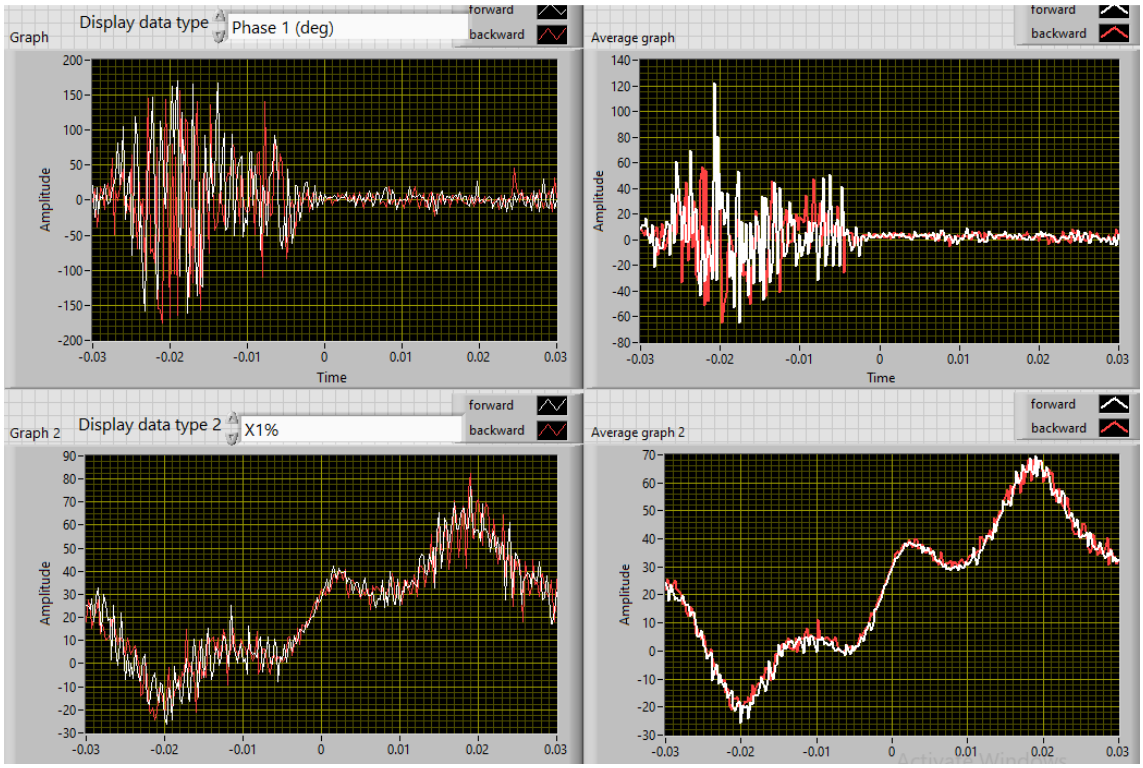

Figure C.5 THz R spectra of CO without offset

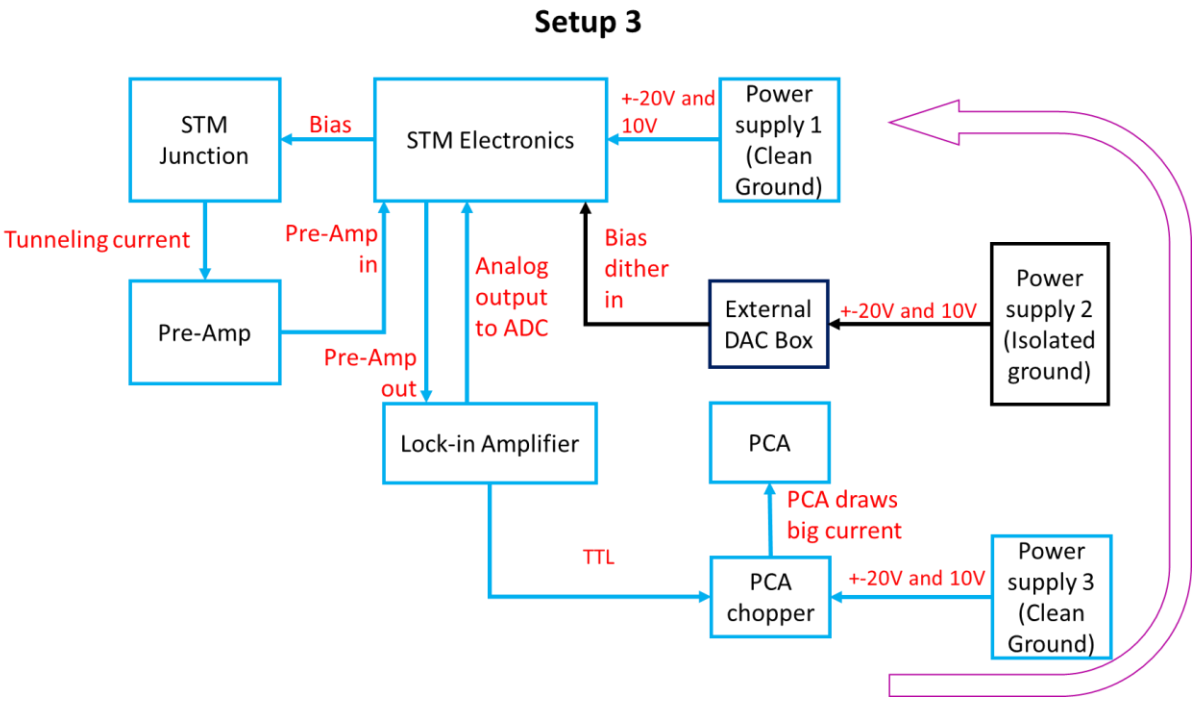

Figure C.6 Electrical connection scheme of setup 3

Table C.1 Testing result with setup 3

PCA connected to PCA chopper	PCA chopper output voltage on	DAC connected to bias dither input	GND isolator on TTL line	X1% with tip over BKG@10mV/0.2nA
Yes	No	Yes	No	2
No	Yes/No	Yes	No	2
Yes	Yes	Yes/No	No	29
Yes	Yes/No	Yes/No	Yes	5
100ohm resistor load to simulate PCA	Yes /No	Yes	Yes	6
	Yes	Yes	No	80
	No	Yes	No	2

C.2 Sample Cleaning Cautions

STM IV has had trouble getting sample clean for years. The surface scans at room temperature often appear junky, rough and noisy. We tried several many things to improve the surface cleaning result, including optimize alignment of ion beam, trying different cleaning condition and checking for chemical contamination in the STM chamber, and we have obtained the following conclusion:

1. Alignment of ion beam is crucial for getting efficient sputtering. Bad alignment may lead to coating of sample holder material (Molybdenum) and eventually roughening of crystal substrates. Instruction of ion gun alignment is described in Appendix C.3.
2. We have found that for STM IV ion gun (RBD 04-165 ig2), higher beam energy sometime yields cleaner surface with less impurities but more surface structural defects. A topography scan at 8K for Cu(100) surface is shown in Figure C.7.

   The recently used cleaning condition for select samples are listed in Table C.2.
3. Although there was no leak or chemical contaminants detected by RGA, we did notice unusually higher H_2 level in STM IV chamber than in other STM systems, which has caused strong hydrogen peaks on cold Ag(110) substrate at a close setpoint. The unstable tunneling current noise observed at room temperature is usually gone when system is cooled down to 8K, which also indicate that room temperature noises could be due to the hydrogen diffusion in and out of tunneling junction, which is observed as small 2-level switching in tunneling signal at room temperature (see in Figure C.8).This hydrogen contamination is potentially caused by depleted ion pump cartridge in the main chamber.

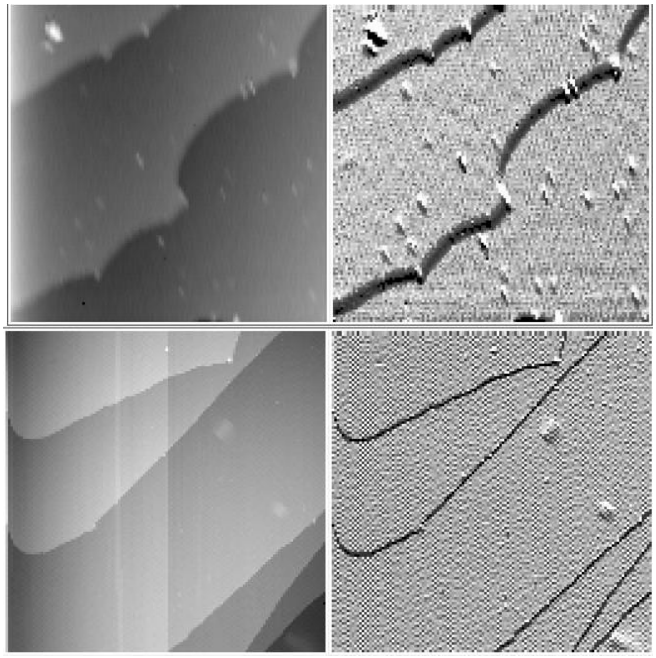

Figure C.7 Comparison of Cu (001) surface scan at room temperature with different sputtering conditions. 1kV beam voltage (top, 128x10 scan) and 1.5kV beam voltage (bottom, 128x16 scan) were used followed by annealing to 600C.

Table C.2 Cleaning conditions for recently used sample

Sample	Sputter conditions	Anneal conditions
Cu(001)/Cu(110)	1.5kV, 2.0A filament current 8E-5 torr Neon, 5min	1.5kV HV Preheat 4.0A, 1min Anneal 600C, 10min
Ag(110)	1kV, 2.0A filament current 8E-5 torr Neon, 5min	1.5kV HV Preheat: 3.7A,1min Anneal: 540C, 10min

Figure C.8 Photo of oscilloscope display showing Hydrogen switching at room temperature. Green: Feedback Z. Yellow: Tunneling current.

C.3 Instruction for Ion Beam Alignment and Focus Optimization.

To align ion beam to sample, we need to be able to visualize the ion beam clearly, which can be achieved by creating a strong beam plasma by increasing the concentration of sputtering gas. In our lab we use Neon as sputtering gas, which gives a magenta ion beam, the step-by-step instruction is as follows:

1. Place a metal dummy sample (can be Molybdenum, Tantalum, or gold) into heater.
2. Turn on ion gun filament at a moderate current setting (e.g., 2.2A), preset beam focus parameter to 4.0 for a 1~2 in working distance, preset beam voltage to 2kV (max option for our model).

3. Fill cold trap and flash TSP to temporarily maintain chamber vacuum, turn the ion gauge gain to 1, then standby main chamber ion pump and close gate valve to main turbo.
4. Slowly leak Neon gas into chamber to 8E-5 torr first, turn on beam voltage. Confirm a normal ion current ~14uA, then continue to slowly fill in Neon, with one person monitoring the chamber pressure and ion current, and another person watching the ion beam from the viewports in the front of chamber. Stop filling once the ion beam color is showing good contrast to background. The ion current will saturate at around 20uA and then decrease as the pressure increases above 1E-4 torr. The beam with 6E-4 torr Neon is shown in Figure C.9 (note: try to keep the pressure lower than 4E-4 to preserve the ion gun lifetime, instead, utilize the contrast and color saturation adjustment of camera to assist beam viewing).
5. Upon finding a bright ion beam, we can then adjust alignment through the 3 arms of the tilt stage that the ion gun is mounted to. At the same time, we can fine tune the focus voltage for ion beam to observe a small colored spot on sample surface. An example of well-focused and well-aligned beam spot on a Au(111) sample is displayed in Figure C.10.

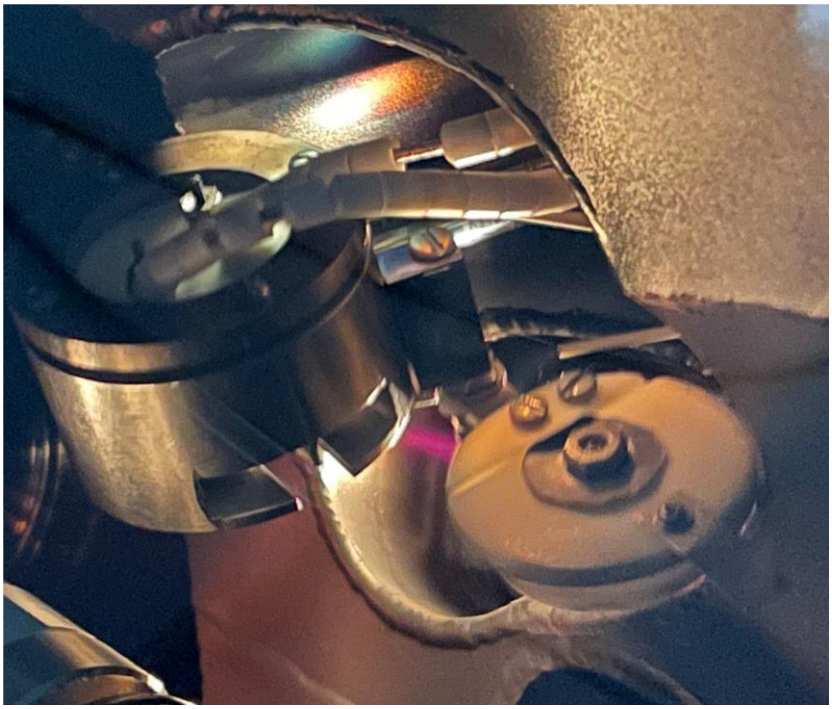

Figure C.9 Ion beam plasma viewed from front top viewport. 2kV beam voltage, 2.2A filament current, and 6E-4 torr Neon pressure was used.

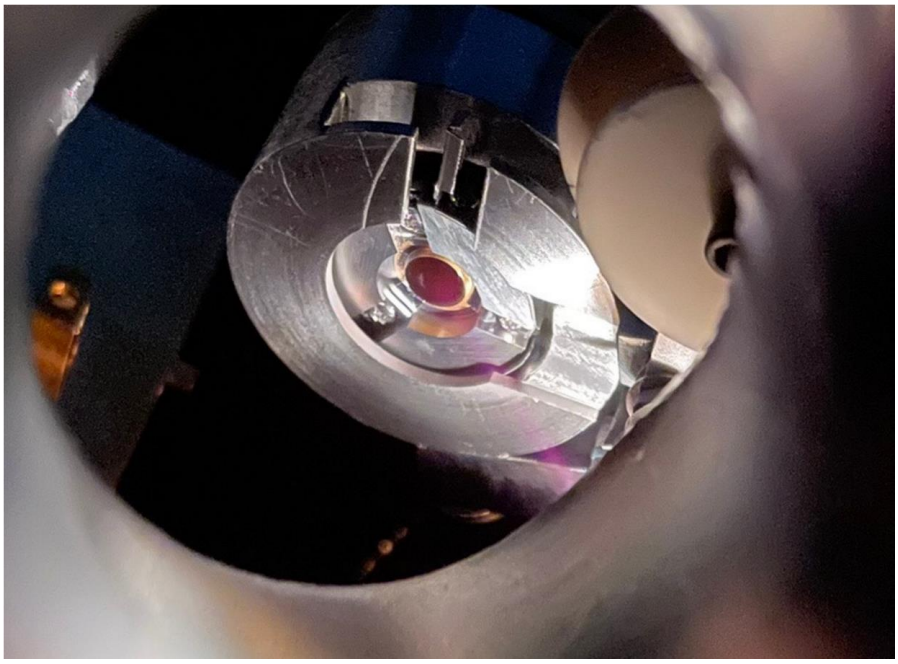

Figure C.10 Photo of a well-aligned ion beam on Au(111) sample

C.4 Back Reflection Interference Issue with Crystal Quartz Window

A flaw with the UHV window design described in Appendix A is that the use of crystal quartz (CQ) window without wedge. This can cause a significant back reflection interference in both THz and optical radiation. An example of frequency scan of THz rectification over Cu_2N is shown in Figure C.11, with an oscillation period of 23.5GHz.

As shown in Figure C.12, assuming beam 1 and 2 are the transmitted beam and back reflected beam respectively. The electric field after window for both beam at frequency f can be written as:

$$E_1 = a_1 \exp(-i\phi_1) \exp(i2\pi ft)$$

$$E_2 = a_2 \exp(-i\phi_2) \exp(i2\pi ft) \qquad (C.1)$$

The amplitude the back reflected beam 2 has a phase lag compared to the transmitted beam 1:

$$\phi_2 - \phi_1 = \Delta\phi = \frac{2\pi f}{c} \cdot 2nL \qquad (C.2)$$

n is the window material refractive index, L is the window thickness. The resulting radiation intensity detected after window can be written as:

$$I = |E_1 + E_2|^2 = |E_1|^2 + |E_2|^2 + E_1E_2^* + E_2E_1^*$$

$$= a_1^2 + a_2^2 + 2a_1a_2\cos(\Delta\phi)$$

$$= a_1^2 + a_2^2 + 2a_1a_2\cos\left(\frac{2\pi f}{c} \cdot 2nL\right) \qquad (C.3)$$

The third term indicates an oscillation in electric field amplitude or optical power will be observed as a function of f, with the period in f written as:

$$\Delta f = \frac{c}{2Ln} \tag{C.4}$$

For a CQ window, refractive index near 0~1THz is $n = 2.115$ according to reference[1], we obtain an estimated THz power oscillation period in frequency domain to be:

$$\Delta f = \frac{(3 \times 10^8)\frac{m}{s}}{2 \times 2.115} \times \frac{1}{L} = 0.709 \times \frac{1}{L(m)} = \frac{70.9}{L(mm)}\ \text{GHz} \tag{C.5}$$

With 3mm CQ window on STM chamber, $\Delta f = 23.63\ \text{GHz}$, which agrees well with the experimentally observed 23.5 GHz oscillation for THz rectification signal.

By measuring THz-induced photocurrent in air with the setup shown in Figure C.13, we also observe various oscillation period of E_{THz} for different CQ window thickness (Figure C.14). As shown in Figure C.15, the fitted slope of oscillation period as a function of $1/L(mm)$ is 66.8, which also agrees with the result in Eq. $(C.5)$.

To summarize, the crystal quartz window has stronger internal reflectance and leads to interference between the back-reflected beam and transmitted beam and cause spurious oscillation of power sensitive measurement in frequency domain. A wedged window should be able to mitigate this problem.

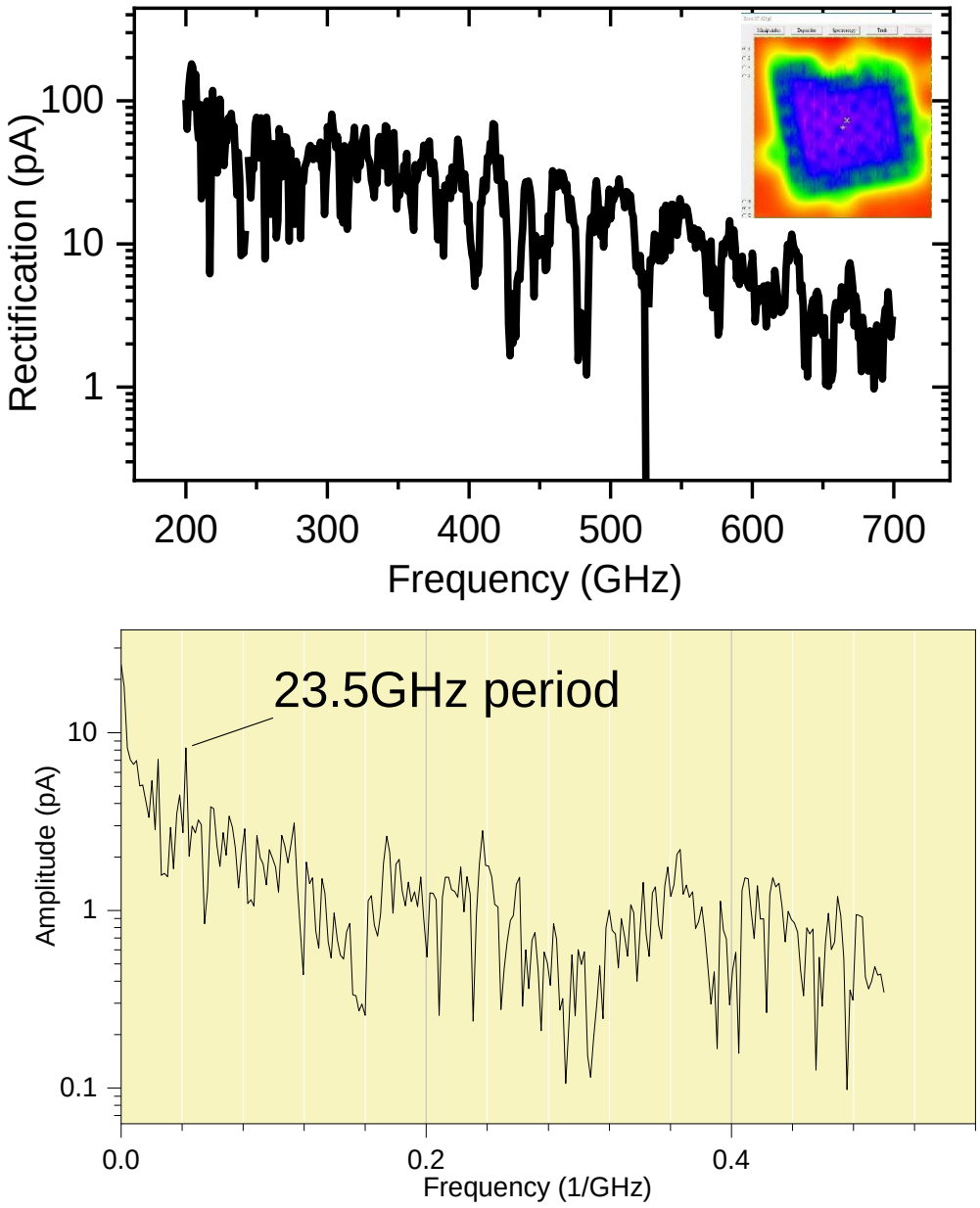

Figure C.11 Interference induced oscillation in THz rectification frequency scan over Cu_2N. Top: the THz rectification frequency scan taken at -41mV with set point 20mV/0.3nA; bottom: The FFT of THz rectification frequency scan showing a peak oscillation period at 23.5 GHz

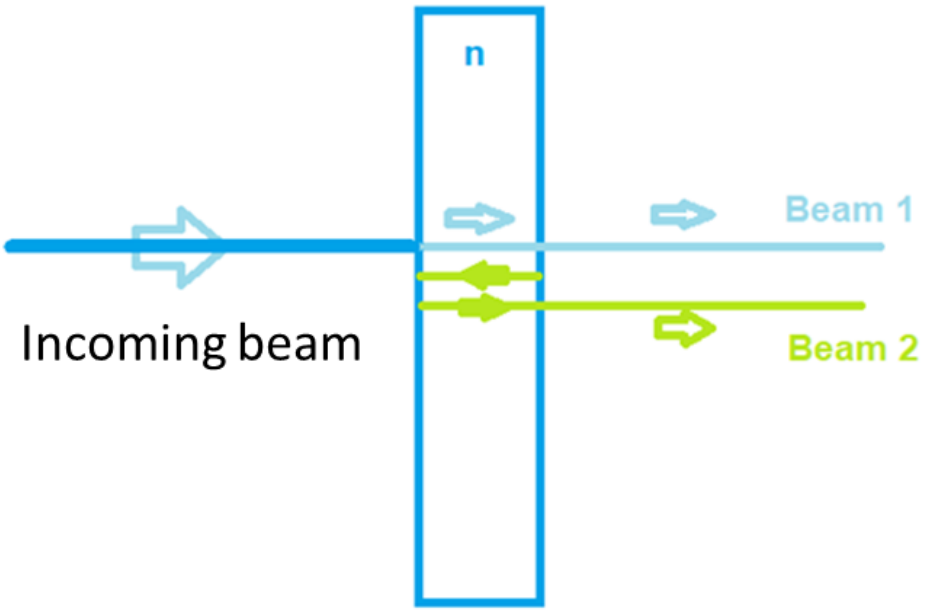

Figure C.12 Schematic of back-reflected THz/optical beam at crystal quartz interface

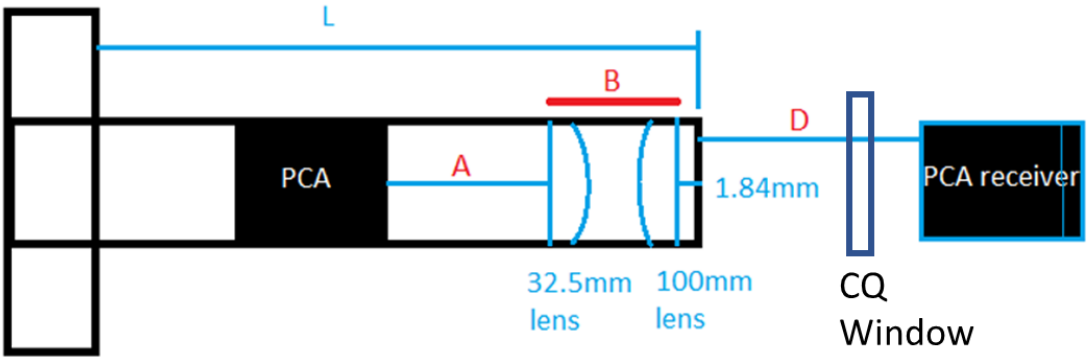

Figure C.13 setup for ambient measurement of THz transmittance using PCA receiver

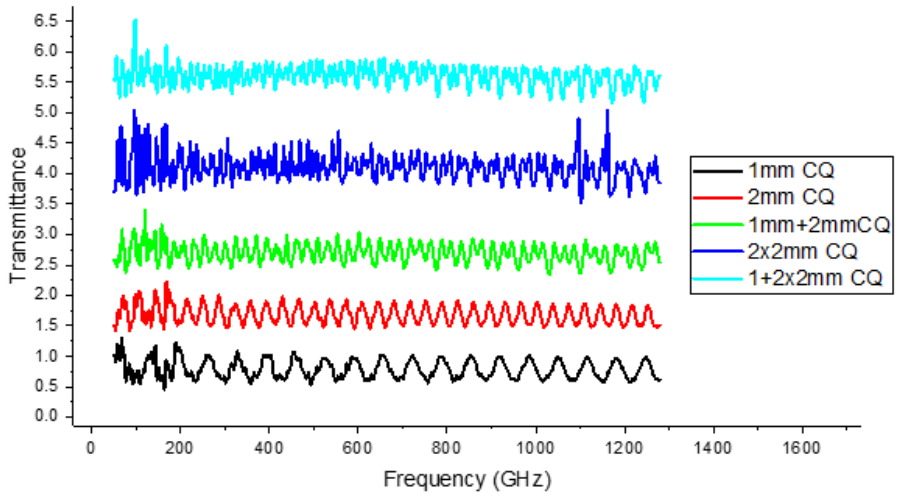

Figure C.14 Transmittance as a function of frequency with different thickness of CQ windows

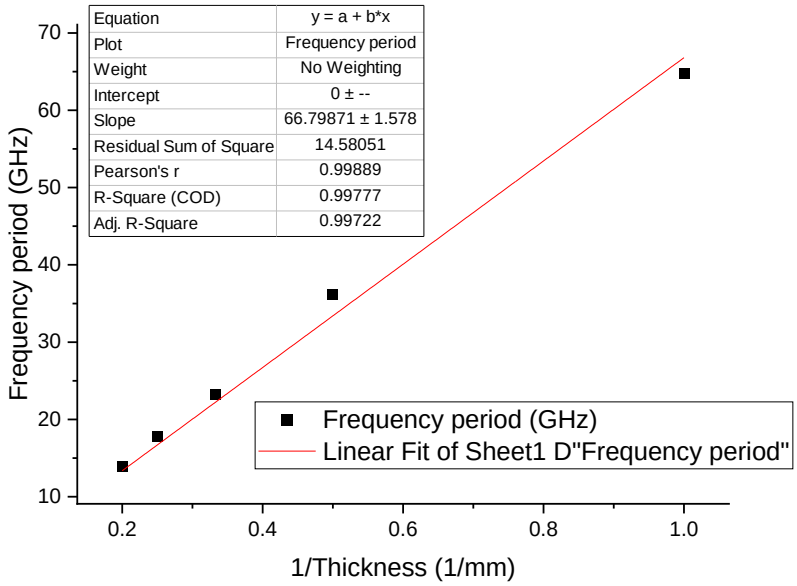

Figure C.15 Extracted Transmittance oscillation period in GHz as a function of 1/thickness (mm), the fitted slope is 66.8.

C.5 Long-Term Power Instability of Fiber Coupled 1550 nm Lasers

For the optical rectification measurement over Pyrrolidine, we have also tried frequency scan with the Terascan 1550 lasers, in hope of finding a resonance feature that corresponds to the N-H first overtone. However, similar to the THz FDS, we encountered a similar problem with the power oscillation in frequency domain, making it hard to distinguish any resonance feature. As shown in Figure C.16, the feedback Z signal has reflected the optical power fluctuations better than the rectification signal. The power fluctuation with shorter period is attributed to the CQ window back-reflection, as discussed in Appendix C.4. However, fluctuations of larger amplitude and irregular period are also observed. These bigger fluctuations have shown to be sensitive to both the fiber shapes and room temperature. A study by Fang et al.[2] used the bending-induced transmission loss to detect Glucose solution concentration, which have shown transmission loss spectra sensitive to both the bending radius and refractive index of the outer core formed by the Glucose solution. We further confirmed the correlation between room temperature and power fluctuation by recording power spectra of laser with a setup shown in Figure C.17 over long time period while monitoring the room temperature. Over the course of 13 hours, we took multiple power spectra and found that even for a room temperature drift smaller than 1℃, there's significant phase shift of the observed fiber-induced power fluctuations (Figure C.18). The phase shift in wavelength axis is also shown to be inversely correlated with room temperature, which indicates that observed power fluctuation is likely mediated by the fiber refractive which is sensitive to environment temperature.

To mitigate the fiber-induced power fluctuation and its long-term phase shift, we can try to arrange the fibers with minimum bending and develop a temperature-stable enclosure for the fiber setup.

However, such effort may not completely get rid of power fluctuation, another solution to consider is to use free space optics setup.

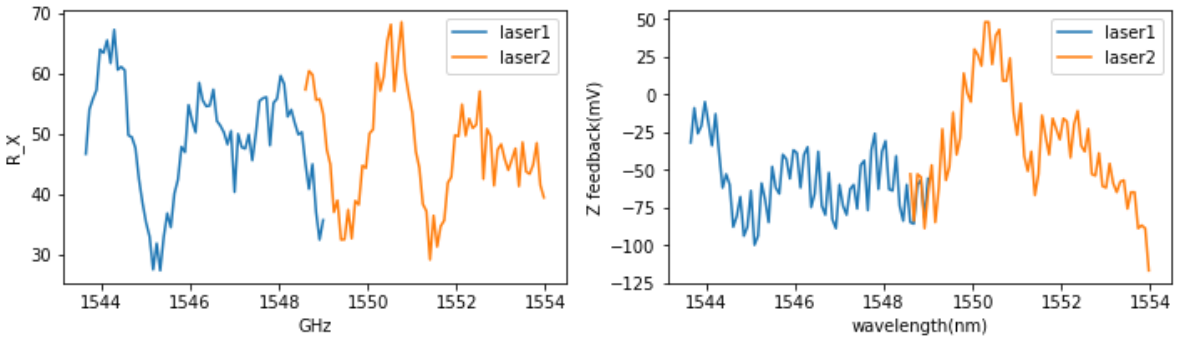

Figure C.16 Frequency scan of optical rectification over pyrrolidine in the range of 1544~1554 nm. Left: the optical rectification signal as a function of wavelength (nm); right: the Z feedback signal as a function of

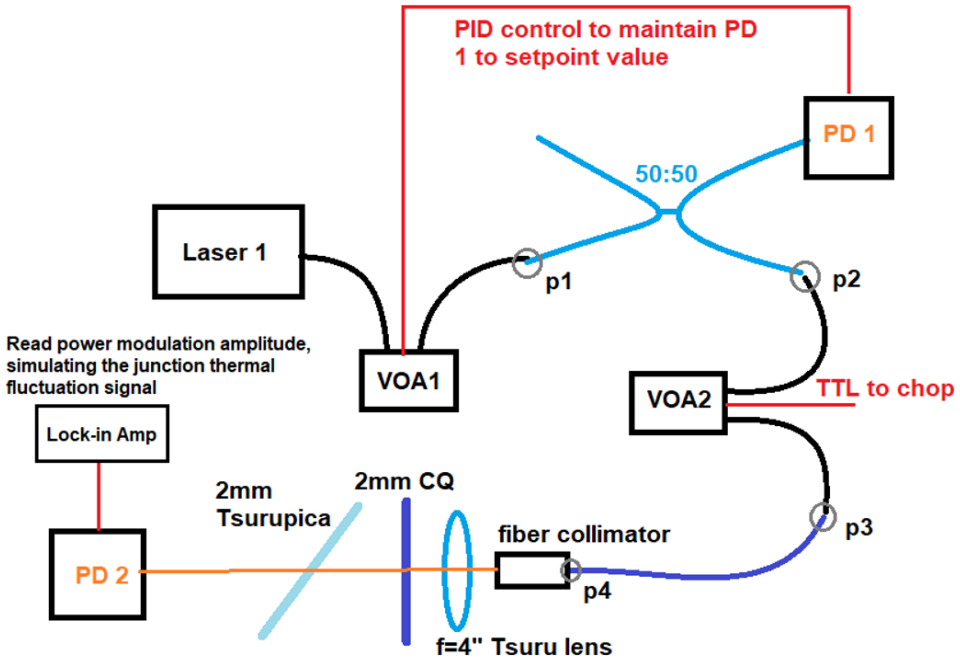

Figure C.17 Experimental setup for testing long-term laser power stability in air. Use Tsurupica and CQ window to simulate the windows in UHV chamber. Photo diode PD2 is used to detected chopped light and then lock-in amplifier extract the first harmonic signal.

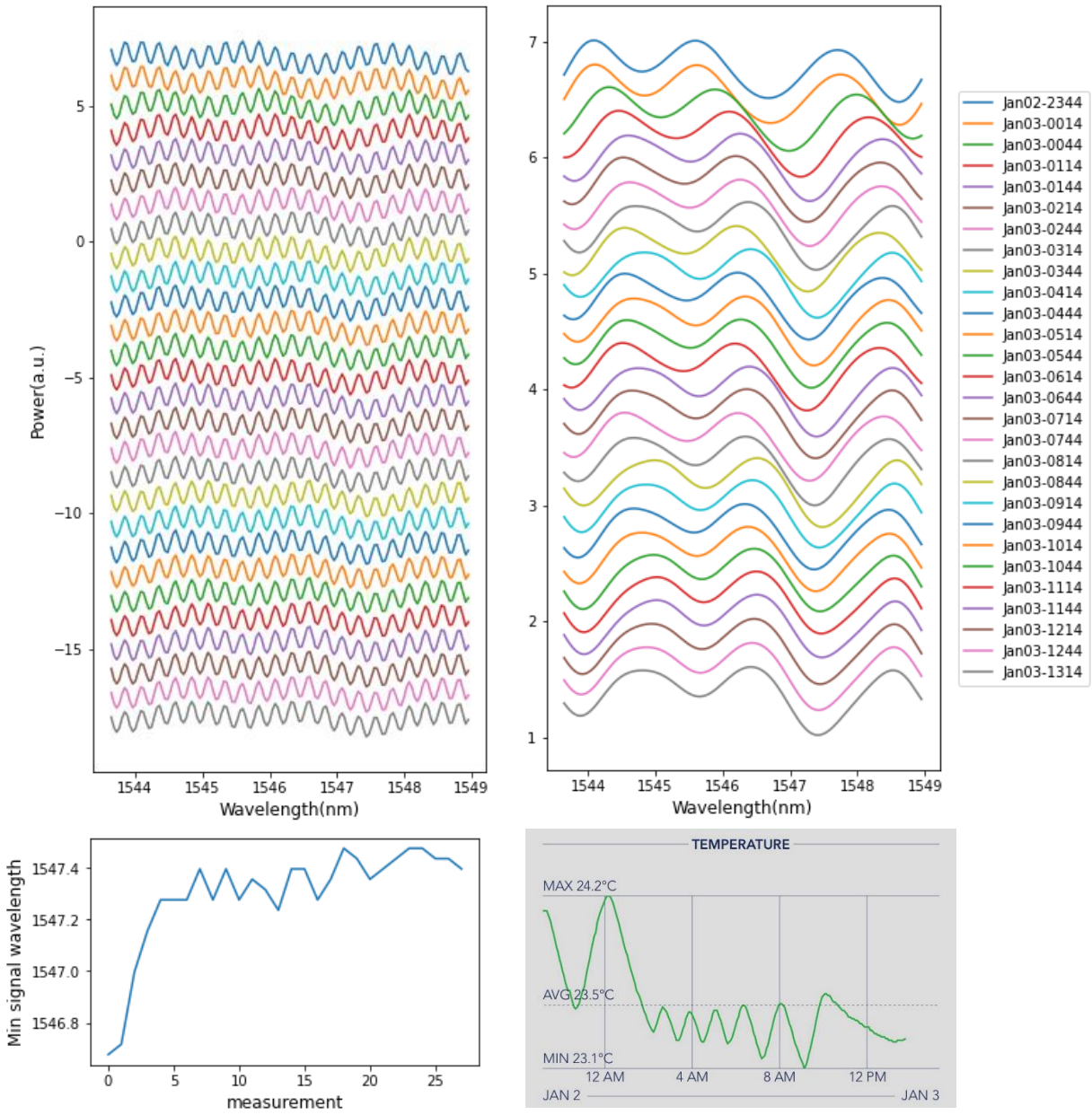

Figure C.18 Correlation between fiber induced power oscillation and room temperature. Upper left: power spectra taken at different times throughout a period of 13 hours. Upper right: FFT-filtered power spectra presenting only the larger fiber-induced power fluctuation. Bottom left: the minimum power wavelength for each measurement extracted from the FFT-filtered data.

Bibliography

[1] E. Castro-Camus, J. Lloyd-Hughes, M.D. Fraser, H.H. Tan, C. Jagadish, and M.B. Johnston, Detecting the full polarization state of terahertz transients, in: Ed. by R.J. Hwu and K.J. Linden, Proc.SPIE, (2006), p. 61200Q.

[2] Y.L. Fang, C.T. Wang, and C.C. Chiang, *Sensors (Switzerland)*, **16**, 1460 (2016).

Appendix D

Gold Plating Instruction Manual

We have two types of immersion electroplating Gold Plating Solution which can be used for different finish of gold plating. The **24 K pure gold plating solution** is a 99.9% purity soft pure gold plating solution which plates to virtually any thickness desired and has a matte effect for thick layer. The **24K Bright Gold Solution** is a hard acid immersion gold plating solution which produces a 99.7% purity hardened gold plate and effectively plates to a thickness of 2.5 microns (100 micro-inches). Table D.1 lists some critical gold plating conditions based on test results, for detailed information please refer to the original data sheet.

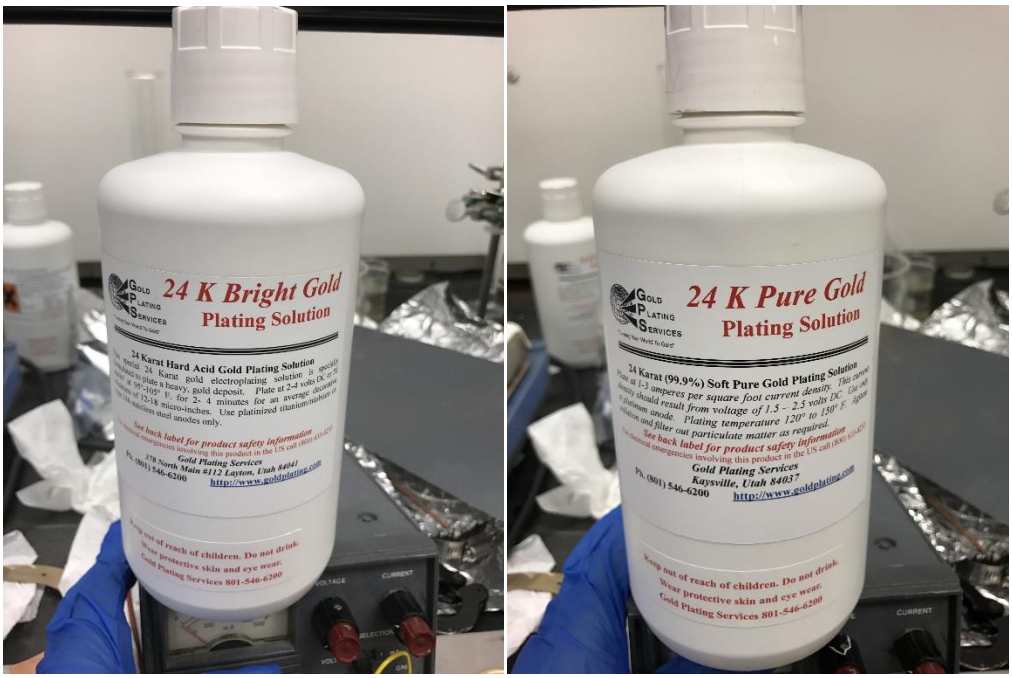

Figure D.1 Two types of gold plating solution from Gold Plating Services

Table D.1 Operating conditions for two types of gold plating solutions

	Pure gold plating solution	Bright Gold plating solution
Operating Temperature	49-65°C	35-40 °C (optimum 37.8 °C)
Voltage	1.5~2 V	1.5~3V[a]
Anode	Platinized Titanium	
Agitation	Moderate relative Cathode to solution movement	Cathode movement or solution pumping

[a] For parts with large surface area, use 50 mA/in^2 current. (e.g., for scanner shield side plates, do the plating half by half to ensure enough current density while total current from power supply is limited) insufficient current density can yield poor coating thickness on plated surface, plated surface could appear dark or just faint yellow.

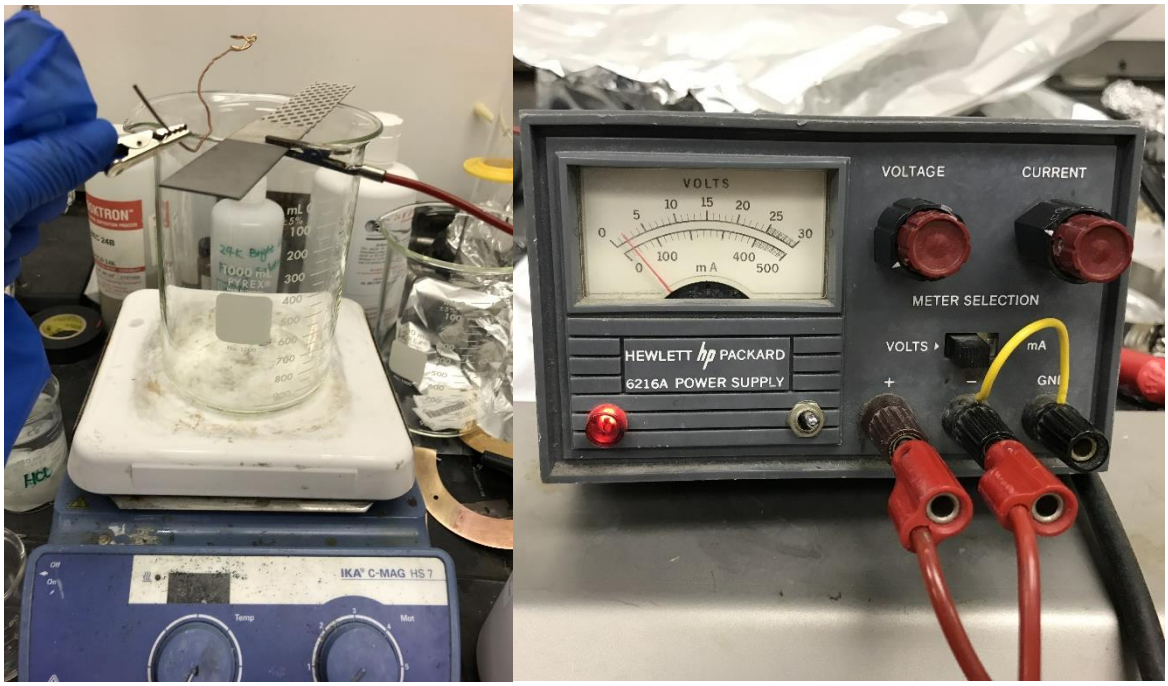

Figure D.2 Setup for immersion gold plating

Setup:

We use the setup shown in Figure D.2 for gold plating. A large beaker is used as the container of the solution. A Platinum-plated Titanium anode (purchased from Gold Plating Services) is specially required for the solution we use and a copper wire hook is used as cathode. The parts to be gold-plated need to be in contact with the cathode during gold plating. Heat plate is used to maintain the temperature condition for gold plating. And a DC power supply is used to provide appropriate current (voltage) for gold plating.

Preparation:

a. Pour the plating solution into the beaker labeled “Gold plating” and start heating it, to speed up the heating process, I use higher temperature (around 80 °C), keep stirring the solution for a while and then tune the temperature down to the operation temperature to keep it warm (the temperature od solution is critical for plating, cold solution can end up blackening the part).

b. Prepare the following solution in corresponding beakers: diluted HCl solution, water for HCl rinse, water for plating solution first rinse, IPA for plating solution second rinse, and IPA for last cleaning.

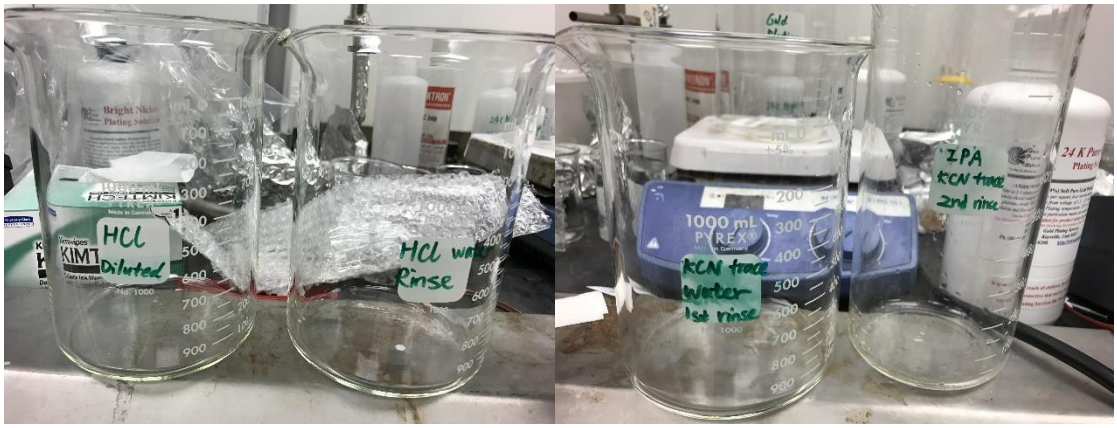

Figure D.3 Labeled beakers for different rinsing solutions.

c. Setup the power supply and both electrodes.

d. Get a Nitrogen gas cylinder ready for blow dry the parts after rinse.

e. Get your parts to be plated ready (polished and cleaned).

Plating procedure:

a. Use a copper wire cathode to hold or hook the part (if it has small holes on it).

b. Dip the part into diluted HCl to etch for a few seconds to remove the oxide on its surface (this step is very critical since you won't be able to get the bright and shiny finish without removing the surface oxide first). Rinse the parts with water and blow dry with N_2.

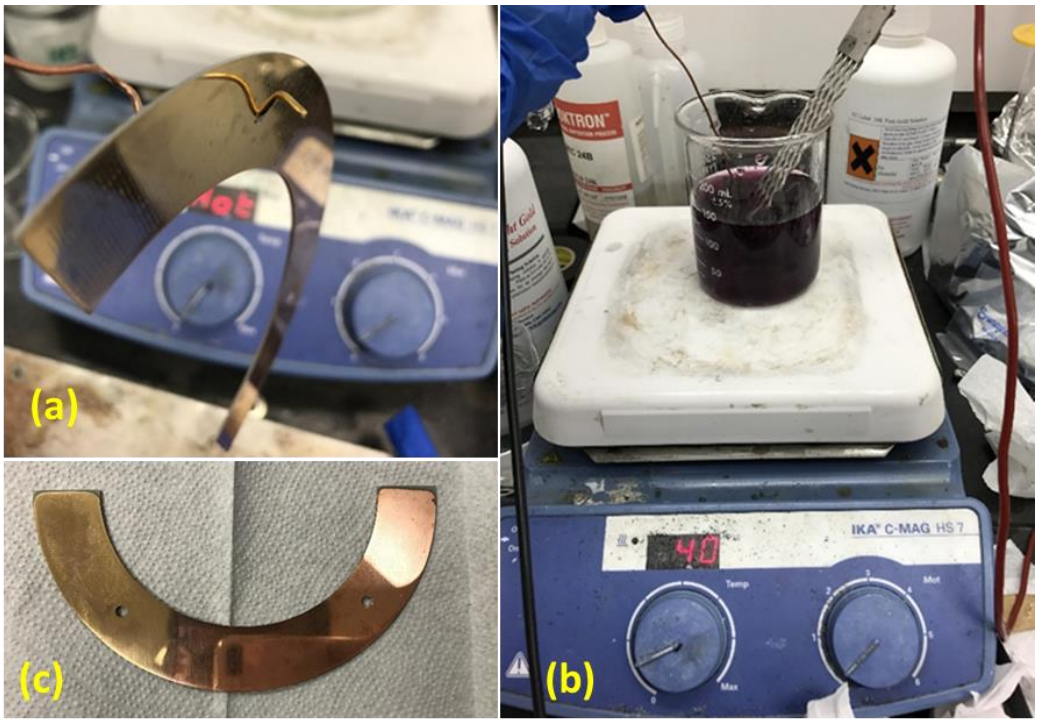

Figure D.4 Gold-plating operation. (a) hook the part with copper wire cathode; (b) dip the parts and anode into solution, connect both electrodes to power supply and turn on the voltage output (around 2.5 Volts); (c) a polished copper baffle with one end gold plated.

c. Use clip to connect the anode and cathode to the power supply, turn on the voltage output and set it to the operating voltage, dip the part and anode into the solution (caution: do not short them!) and check the surface every 5-10 seconds until the plating effect is satisfactory.

For the bright gold solution and small parts, 2.5 volts and 30 seconds is sufficient to give a bright and shiny finish (Figure D.4c) shows a polished copper baffle with its left end gold-plated).

d. After plating, dip and rinse the parts with water first, then with IPA. Both of the rinse waste should be recycled in the labeled bottle which is usually store in the cabinet below the left fume hood in tip-etching room. Put all the rinsed parts together in IPA for final cleaning.

e. Detach both electrodes from power supply and clean up them with same 2-rinse procedure mentioned above.

f. In principle the solution can be reused, but for best effect we recycle used gold plating solution in a labeled bottle (indicating how many times it's recycled) and only reuse it when all the fresher solution is used up.

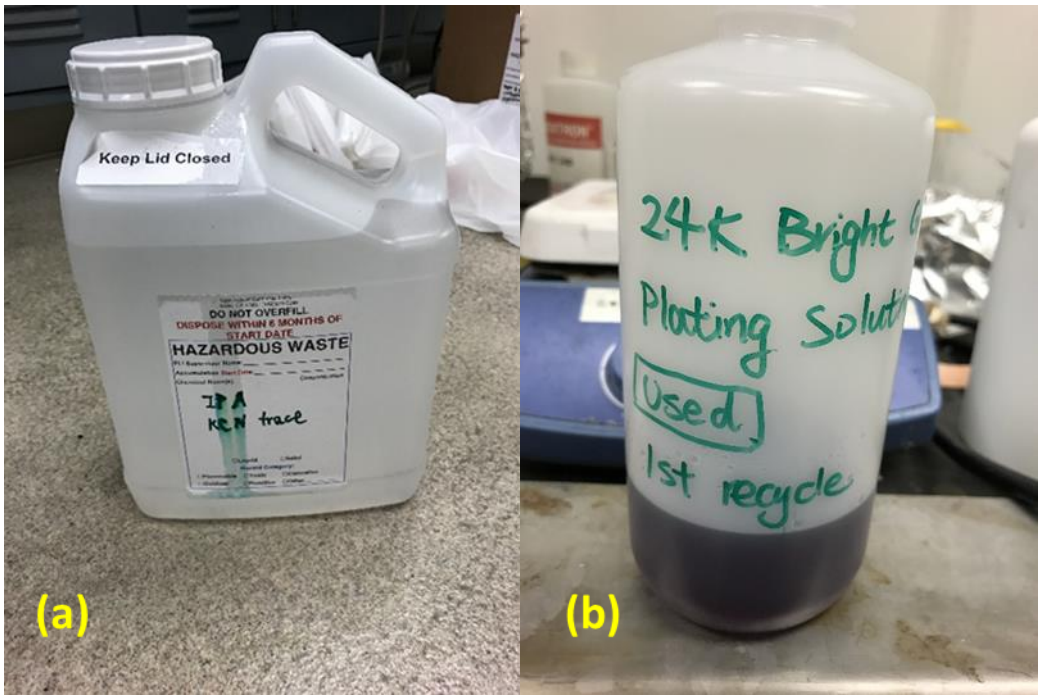

Figure D.5 Waste processing. (a) Recycle the water and IPA that contains trace of plating solution; (b) recycle used plating solution in a separate bottle.

Appendix E

Estimation of THz Beam Size, Far Field and Near Field Enhancement

We use a circular pyroelectric to detect the power of a focused THz beam. As shown in Figure E.1, a THz gaussian beam with FWHM radius a is offset horizontally by distance d from the circular sensor with radius R.

The field intensity of this gaussian beam can be written as a function of r and θ :

$$I(a, r, \theta) = I_0 \exp\left(-\frac{2[(r\sin\theta)^2 + (r\cos\theta - d)^2]}{a^2}\right) \quad (E.1)$$

Here I_0 is the peak intensity of the gaussian beam.

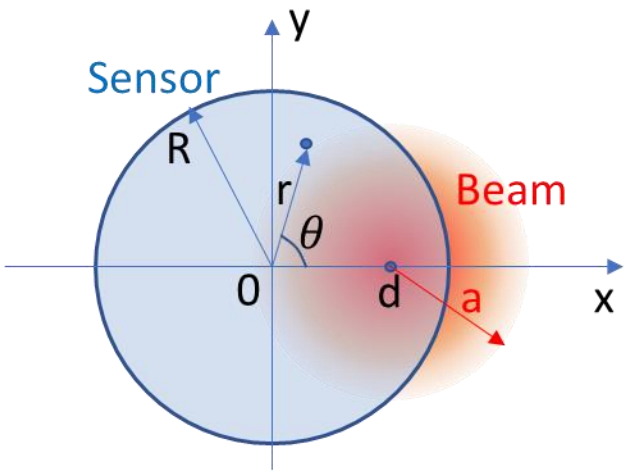

Figure E.1 Schematic of THz beam and sensor positioning in a coordinate

The total power detected by the sensor can be obtained by integrating $I(r, \theta)$ over the sensor area:

$$P(R, d, a) = \int_0^R r dr \int_0^{2\pi} d\theta\, I(a, r, \theta) \quad (E.2)$$

For a measurement with no lateral offset (d=0,) the measured power should be maximized:

$$P_0(R,a) = \frac{\pi}{2} I_0 a^2 \left(1 - \exp\left(-\frac{2R^2}{a^2}\right)\right) = P_{total}\left(1 - \exp\left(-\frac{2R^2}{a^2}\right)\right) \quad (E.3)$$

Here P_{total} is the total power of the THz beam. When $R > a$, we can assume $P_0(R,a) \approx P_{total}$.

With a setup shown in Figure E.2 and THz frequency at 500 GHz, we measured the maximum power P_0 first, then locate d_1 and d_2 where $P(R,d_1,a)$=$P(R,d_2,a) = \frac{P_0}{2}$. Using the averaged value $\overline{|d|} = 2.65\text{mm}$, and with an effective sensor radius R=2.75mm, we obtained **an estimated THz beam FWHM to be $2a = 2.9\text{mm}$** by numerically solving the equation below:

$$\frac{P\left(R,\overline{|d|},a\right)}{P_0(R,a)} = 0.5 \quad (E.4)$$

As an electric-magnetic wave, THz beam peak intensity can be also written as:

$$I_0 = \frac{E_0^2}{2c\mu_0} \quad (E.5)$$

E_0, c, μ_0 are respectively the peak electric field, speed of light, and permeability of free space.

Considering a total power transmission of 0.8 after the two focusing lenses, max THz power measured by the sensor according to Eq. (E.3) is approximated as:

$$P = 0.8P_{total} = \frac{2\pi}{5} I_0 a^2 \quad (E.6)$$

Combing Eq. (E.5) and Eq. (E.6), we have:

$$E_0 = \sqrt{\frac{4c\mu_0}{\pi a^2} P_{total}} \quad (E.7)$$

Use the estimated value of a $= 1.45$ mm and datasheet calibration value of $\mathrm{P_{total}}(500\mathrm{GHz}) = 8.7\mu\mathrm{W}$, we can estimate the electric field intensity at beam center to be:

$$\mathrm{E_0}(500\mathrm{GHz}) = 0.44\ \mathrm{V/cm}$$

The photocurrent measurement using PCA receiver (I_{photo}) with the far field calculation at 500 GHz yields a ratio of ~$426\ nA \cdot cm/V$. By scaling the I_{photo} spectra using this ratio constant, we get a full spectrum range estimation of the far field as shown in Figure E.3.

Using the fitted $V_{THz}(150GHz)$ at junction (40mV/0.8nA set point) as a function of PCA receiver photocurrent (details described in Chapter 2), we can obtain ratio between V_{THz} and electric far field:

$$V_{THz}(mV) = 0.02057 * I_{photo}(nA) = 8.76282 * E_{Far\ field}(V/cm) \qquad (E.8)$$

Using the estimated junction gap of 3.65 Å at 40mV/0.8nA, we can convert the above relation into:

$$E_{Nearfield}(V/cm) = \frac{V_{THz}(mV)}{3.65} * 10^5 = 2.4 * 10^5 E_{Far\ field}(V/cm) \qquad (E.9)$$

This result indicates a rather strong nearfield enhancement factor of 10^5 order of magnitude for THz radiation.

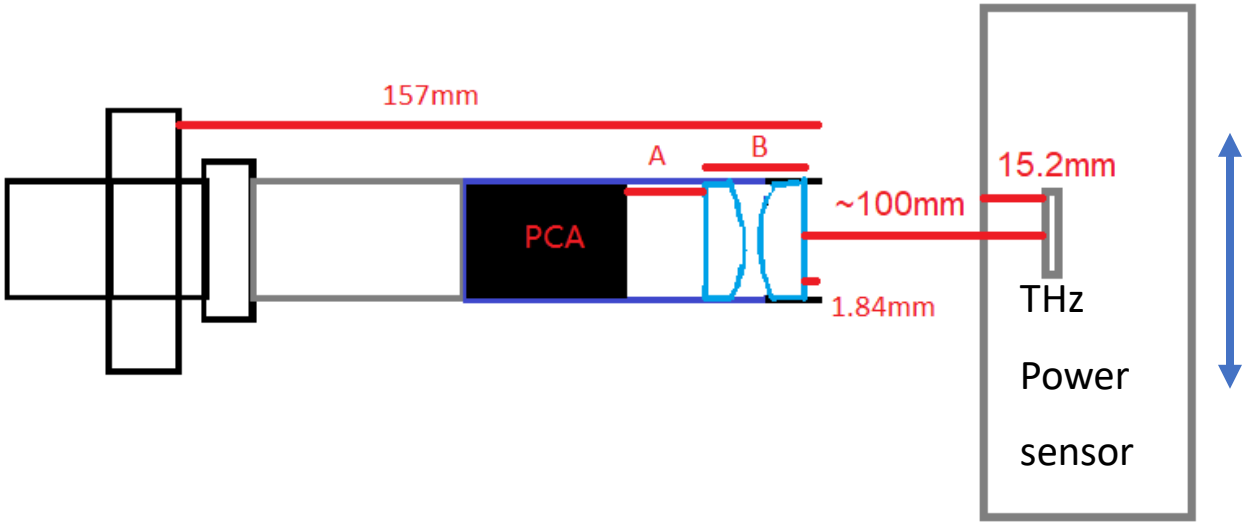

Figure E.2 Schematic of measurement focused THz beam using a pyroelectric sensor

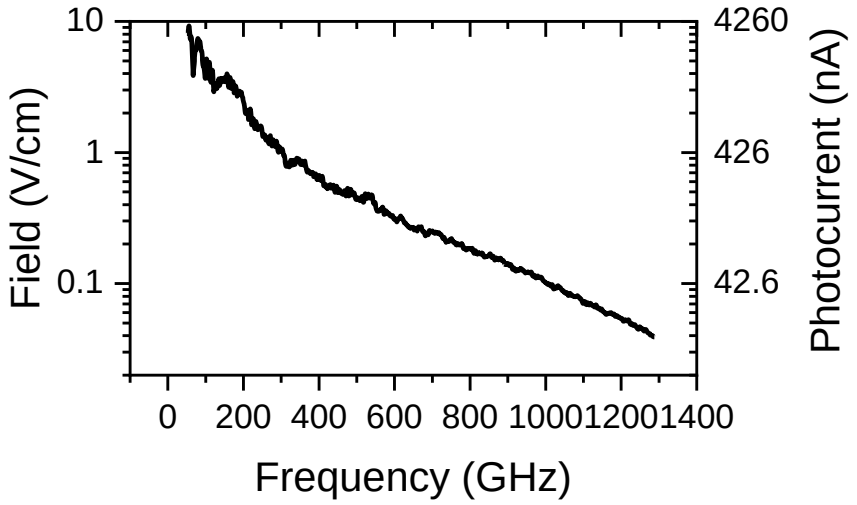

Figure E.3 Estimated THz far field as a function of frequency

Appendix F

MATLAB Codes for Estimation of THz Voltage at STM Junction

This appendix includes the MATLAB codes used for estimating THz voltage (V_{THz}) at STM junction with 2 different methods, as discussed in Chapter 2. Section F.1 is the code for fitting THz R spectra from an IETS spectra with known bias modulation, and section F.2 is the code for fitting and IETS with THz from an IETS taken without THz. For both fittings, V_{THz} is obtained as one of the fitting parameters and each set of spectra used for fitting are obtained over the same molecule with the same set point. Comments of codes are green-colored to assist code reading.

F.1 Fitting THz R spectra from an IETS spectra

```
clear
m1=readmatrix('IETS THz off-3mVMOD.txt');%IETS data, bias unit V
r1=readmatrix('Calibrated data_pA.txt'); );%THz R spectra, bias unit mV
bias=m1(:,1).*1000;% convert to mV, first column of IETS data
d2=m1(:,2); % define ref IETS data array, second column of  IETS data
biasr=r1(:,1).*1000;% convert to mV
scatter(bias,d2,'.','DisplayName',"THz off "); % plotting the IETS data
hold on
%fit IETS with the symmetric function form to obtain peak positions and v_off
ft1=fittype('d2IdV2asym(x,b1,w1,A1,b2,A2,v_off)','coefficients',{'b1','w1','A1','b2','A2','v_off'});
sp1=[19,1.7,10,2.1,6,0.8];% propose a start point based on actual spectra
f1=fit(bias, d2,ft1,'StartPoint', sp1);% fit IETS to obtain 'b1','w1','A1','b2','A2','v_off'
```

```
plot(bias,d2IdV2asym(bias,f1.b1,f1.w1,f1.A1,f1.b2,f1.A2,f1.v_off)); % optional plotting of fitted
IETS curve
 hold on
%fit IETS with the convolution expression to obtain d2I/dV2 term
vm=4.2426; %3mV rms modulation
ft2 = fittype(@(b1,w1,A1,b2,A2,v_off,x)...
    arrayfun(@(vb) integral(@(v)...
    d2IdV2asym(vb+v,b1,w1,A1,b2,A2,v_off).*weight_func(v,vm),-vm,+vm), x));
sp2=[f1.b1,f1.w1*0.5,f1.A1/0.5,f1.b2,f1.A2/0.5,f1.v_off];
f2=fit(bias,d2,ft2,'StartPoint',sp2);
plot(bias,arrayfun(@(vb)...
integral(@(v)...
d2IdV2asym(vb+v,f1.b1,f2.w1,f2.A1,f1.b2,f2.A2,f1.v_off).*weight_func(v,vm),          -
vm,+vm) ,bias));
hold on
plot(bias,  d2IdV2asym(bias,f1.b1,f2.w1,f2.A1,f1.b2,f2.A2,f1.v_off));%plotting  fitted  d2I/dV2
term
hold on
%fit R spectra to the covolution of obtained d2I/dV2 with weight_fuc_R to obtain vthz
ft3 = fittype(@(vthz,A,v_off,b1,b2,x) arrayfun(@(vb) integral(@(v)…
A.*d2IdV2asym(vb+v,b1,f2.w1,f2.A1,b2,f2.A2,v_off).*weight_func_R(v,vthz) ,-vthz,vthz) ,x));
PCA=[0,-0.1,-0.2,-0.3,-0.45,-0.6,-1.3]';
% initialize the parameter array to store fitted parameter for each R spectra
```

```
vthz=zeros(7,1);

Afit=zeros(7,1);

vofffit=zeros(7,1);

b1fit=zeros(7,1);

b2fit=zeros(7,1);

sofffit=zeros(7,1);

ci=zeros(7,10);

fittedresult=zeros(length(biasr),8);

fittedresult(:,1)=biasr;

for n=2:1:8 % fit each R spectra in the data set using a for loop

r=r1(:,n); %unit pA

f3=fit(biasr,r,ft3,'StartPoint',[vm,1, f2.v_off, f2.b1,f2.b2])

ci(n-1,:)=reshape(confint(f3),1,[])

vthz(n-1)=f3.vthz;

Afit(n-1)=f3.A;

vofffit(n-1)=f3.v_off;

b1fit(n-1)=f3.b1;

b2fit(n-1)=f3.b2;

scatterlabel=['PCA ',num2str(PCA(n-1)),'V'];

scatter(biasr,r,10,'filled','DisplayName',scatterlabel);

hold on

fitlabel=['Vthz=',num2str(f3.vthz),'mV'];

fitted=arrayfun(@(vb)...
```

```
    integral(@(v)...
    f3.A.*d2IdV2asym(vb+v,f3.b1,f2.w1,f2.A1,f3.b2,f2.A2,f3.v_off).*weight_func_R(v,f3.vthz)...
    ,-f3.vthz,f3.vthz)...
    ,biasr);
fittedresult(:,n)=fitted;
plot(biasr, fitted, 'DisplayName',fitlabel,'LineWidth',1.5,'Color','k');
hold on
end
% plot formatting
title('R spectra with various PCA voltage')
xlabel('Bias(mV)','FontSize',12)
ylabel('Rectification(pA)','FontSize',12)
legend('Location','eastoutside','FontSize',11)
legend show
set(gca,'XLim',[-50 50],'XTick',[-50:25:50]);
box on
hold off
% saving files for fitting results
writematrix([PCA vthz Afit vofffit b1fit b2fit],'fittedparameter.txt');% save fitted parameter
writematrix([PCA ci],'95_conf_int.txt');% save fitting error
writematrix(fittedresult,'fittedcurves.txt');% save fitted data
% Function definition
function y=d2IdV2asym(v1,b1,w1,A1,b2,A2,v_off)
```

```
%v1: bias
%v_off: bias offset
%b: peak position
%w: line with
%A: strength
v = v1+v_off;
y = A1*(...
  (exp(2*(b1-v)/w1).*(b1-v)+exp((b1-v)/w1).*(b1-v)-2*exp((b1-v)/w1).*(exp((b1-v)/w1)-
1)*w1)...
  ./((exp((b1-v)/w1)-1).^3*w1^2)-...
  (exp(2*(b1+v)/w1).*(b1+v)+exp((b1+v)/w1).*(b1+v)-2*exp((b1+v)/w1).*(exp((b1+v)/w1)-
1)*w1)...
  ./((exp((b1+v)/w1)-1).^3*w1^2)...
   )+ A2*(...
  (exp(2*(b2-v)./w1).*(b2-v)+exp((b2-v)/w1).*(b2-v)-2*exp((b2-v)/w1).*(exp((b2-v)/w1)-
1)*w1)...
  ./((exp((b2-v)/w1)-1).^3*w1^2)-...
  (exp(2*(b2+v)./w1).*(b2+v)+exp((b2+v)/w1).*(b2+v)-2*exp((b2+v)/w1).*(exp((b2+v)/w1)-
1)*w1)...
  ./((exp((b2+v)/w1)-1).^3*w1^2));
end
function y=weight_func(v,vm)
%instrumental function for IETS with sine modulation
```

```
% v is bias variable, vb is bias, vm is modulation amplitude
if v>vm|v<-vm
    y=0;
else
    y=2./(3.*pi.*vm^2).*(vm^2-v.^2).^1.5;
end
end
function y=weight_func_R(v,vm)
%instrumental function for RS with square wave modulation
% v is bias variable, vb is bias, vm is modulation amplitude
if v>vm|v<-vm
    y=0;
else
    y=asin(abs(v)/vm).*abs(v)/pi-abs(v)/2+sqrt(vm^2-v.^2)/pi;
end
end
```

F.2 Fitting and IETS with THz

```
clear;
data=load('IETSdata.mat');%  This is a preprocessed data set, first column is bias, second is reference IETS, the rest of the columns are IETS taken with various THz intensity, all spectra scaled to the same sensitivity
v=data(:,1);%unit mV
y=data(:,2);% IETS without THz (reference data)
ref=griddedInterpolant(v,y,'linear','nearest'); % interpolate the reference data to improve fitting smoothness
scatter(v,y,10,'filled','DisplayName',"THz off "); % plot IETS without THz (reference data)
hold on
%  Define a fittype for fitting IETS with THz
ft1 = fittype(@(vm,A,x)arrayfun(@(vb)A.*integral(@(x)ref(x).*weight_func(x,vb,vm),vb-vm,vb+vm),x));
sp=[10,1]; % propose an initial parameter
% Initialize empty arrays to store fitting results:
fitteddata=zeros(length(v),10);
name=["0V","-0.1V","-0.2V","-0.35V","-0.5V","-0.7V","-0.8V","-0.9V","-1.1V","-1.3V"];
vthz=zeros(1,10);
A_fits=zeros(1,10);
ci=zeros(10,4); % 95 percent confidence interval for fitted parameters
% Use for loop to fit each of the IETS in the data set
for n=1:1:10
```

```
    iet=data(:,n+2);
    scatter(v,iet-n.*70,10,'filled','DisplayName',strcat("PCA ",name(n))) %plot each raw data
    hold on
    f1 = fit(v,iet,ft1);
    vthz(n)=f1.vm;
    A_fits(n)=f1.A;
    cint=reshape(confint(f1),1,[]);
    ci(n,:)=cint
    label=['Fitted V_T_H_z=',num2str(f1.vm),'mV'];
    fitteddata(:,n)=arrayfun(@(vb)f1.A.*integral(@(x)ref(x).*weight_func(x,vb,f1.vm),vb-
f1.vm,vb+f1.vm),v);
    plot(v,fitteddata(:,n)-n*70,'DisplayName',label,'LineWidth',1.5,'Color','k');% plot each fitted
curve
    hold on
end
% plot formatting
xlabel('Bias(mV)','FontSize',11)
ylabel('IETS(nA/V^2)','FontSize',11)
legend show
set(gca,'XLim',[-50 50],'XTick',[-50:25:50]);
legend('Location','eastoutside','FontSize',11)
box on
hold off
```

```
% save fitting results
writematrix([v fitteddata],'fitteddata.txt');
PCA=[0,-0.1,-0.2,-0.35,-0.5,-0.7,-0.8,-0.9,-1.1,-1.3];
writematrix([PCA' vthz' A_fits'],'fitted Vthz.txt');
writematrix([PCA' ci],'95_conf_int.txt');
% Function definition

function y=weight_func(v,vb,vm)
% v is bias variable, vb is bias, vm is modulation amplitude
if v>vb+vm|v<vb-vm
    y=0;
else
    y=1./(pi.*vm.*sqrt(1-((v-vb)./vm).^2));
end
end
```

Appendix G

Python Scripts for Numerical Simulation of Optical Rectification Spectra

The python scripts were developed for computing the static ORS and dynamic ORS based on the two-state model and photon-induced transition rate model discussed in Chapter 4. Section G.1 includes all the function definition needed, and section G.2 demonstrate a few examples of actual implementation of the functions for simulation. The code and parameters used in this Appendix only demonstrates an implementation of ORS simulation under specific experimental conditions and readers are expected to modify the code based on their specific need before use. The comments to codes are green-colored and function names are bold for easy reading.

G.1 Function Definitions

```
#Import packages

from scipy import integrate

import numpy as np

import matplotlib.pyplot as plt

import ipywidgets as widgets

from ipywidgets import interact



def popb(rhl,rlh,power,mhl,mlh):

    '''Input:
```

```
    rhl: dark condition H->L transition rate

    rlh: dark condition L->H transition rate

    power: an unitless power factor

    mhl: rate per unit power for photon-induced H->L transition

    mlh: rate per unit power for photon-induced L->H transition

    Return:

    High state population with light on'''

    return (rlh+mlh*power)/(rhl+rlh+(mhl+mlh)*power)


def rb(rhl,rlh,power,mhl,mlh):

    '''Input:

    rhl: dark condition H->L transition rate

    rlh: dark condition L->H transition rate

    power: an unitless power factor

    mhl: rate per unit power for photon-induced H->L transition

    mlh: rate per unit power for photon-induced L->H transition

    Returns:

    2-D array of transition rates with light on:
```

```
    first row L->H rate, second row H->L rate
    '''
    return rlh+mlh*power,rhl+mhl*power
def cur_d(v,poph,tl=0.672,i=1):
    '''computes the dark condition tunneling current
    Input:
    v: Bias array
    poph: high-state poppulation at dark condition
    tl: Low state conductance, pA/mV. Default as 0.672 for -500mV/1nA setpoint
    i: setpoint current (assuming -500mV setpoint bias), default as 1nA
    '''
    return poph*4*tl*v*i+(1-poph)*tl*v*i
def cur_b(v,poph_b,tl=0.822,i=1):
    '''computes the bright condition tunneling current
    Input:
    v: Bias array
    poph_b: high-state poppulation with light on
    tl: Low state conductance, pA/mV. Default as 0.672 for -500mV/1nA setpoint
```

```
    i: setpoint current (assuming -500mV setpoint bias), default as 1nA
    '''
    return poph_b*4*tl*v*i+(1-poph_b)*tl*v*i
def d_cur(v,tl=0.672,i=1):
    ''' Input:
    tl: low state conductance
    Assuming hight state conductance th=4*tl
    th-tl=3*tl
    Returns difference in H and L state current (unit pA) at bias v
    '''
    return 3*tl*v*i
def w2p(t, wh, wl):
    '''computes the high-state population at time t
    with initial high-state population of 1 and 0 respectively
    Input:
    t: time
    wh: H->L rate
    wl: L->H rate
```

```
    Return:
    n_1: high state population with initial 1
    n_0: high state population with initial 0
    '''
    k = wl+wh
    c = wl/k
    n_1 = np.exp(-k * t + np.log(1 - c)) + c
    n_0 = -np.exp(-k * t + np.log(c)) + c
    return np.array([n_1, n_0])
def eq_pop(hp,b_h_r,d_h_r,b_l_r,d_l_r,n):
    '''assuming system start from pop_H=1, computes the high-state population at end of each
    modulation half cycles for light off(p_d) and light on(p_b)
    Input:
    hp: half modulation period
    b_h_r: laser on, high to low rate
    b_l_r: laser on, low to high rate
    d_h_r: laser off, high to low rate
    d_l_r: laser off, low to high rate
```

```
    n: number of cycles to compute

    '''

    n_b_1, n_b_0 = w2p(hp, b_h_r, b_l_r)

    n_d_1, n_d_0 = w2p(hp, d_h_r, d_l_r)

    p_b = 1

    for j in range(n):

        p_d = p_b * n_b_1 + ((1 - p_b) * n_b_0)

        p_b = p_d * n_d_1 + ((1 - p_d) * n_d_0)

    return p_d,p_b

def eq_process(hp,n0,b_h_r,d_h_r,b_l_r,d_l_r,n):

    '''Computes the time evoution of high-state population for the first n chopping cycles

    hp: half modulation period

    n0: starting high-state population

    b_h_r: laser on, high to low rate

    b_l_r: laser on, low to high rate

    d_h_r: laser off, high to low rate

    d_l_r: laser off, low to high rate

    hp: half period of modulation
```

```
    n: number of cycles to compute
    Return:
    A 2-D numpy array, first row: time, second row: high-state-population
    '''
    tarray=[]
    narray=[]
    n_b_1,n_b_0,n_d_1,n_d_0=[],[],[],[]
    for t in np.linspace(0,hp,15):
        n_b_1=np.append(n_b_1,w2p(t, b_h_r, b_l_r)[0])
        n_b_0=np.append(n_b_0,w2p(t, b_h_r, b_l_r)[1])
        n_d_1=np.append(n_d_1,w2p(t, d_h_r, d_l_r)[0])
        n_d_0=np.append(n_d_0,w2p(t, d_h_r, d_l_r)[1])
    p_b0 = n0
    for j in range(n):
        time=np.linspace(0,2*hp,29)+j*2*hp
#         print('time: ',time)
        p_d = p_b0 * n_b_1 + ((1 - p_b0) * n_b_0)
#         print('p_d: ',p_d)
```

```
        p_d0=p_d[-1]
        p_b = p_d0 * n_d_1 + ((1 - p_d0) * n_d_0)
#         print('p_b: ',p_b)
        p_b0=p_b[-1]
        tarray+=list(time)
        narray+=list(np.append(p_d,p_b[1: ]))
#         print(tarray,narray)
    return np.vstack((tarray,narray))
def int_x(t, hp,theta,v, b_h_r,d_h_r,b_l_r,d_l_r,iset):
    '''Input:
    t: time within half cycle
    v: bias
    b_h_r: laser on, high to low rate
    b_l_r: laser on, low to high rate
    d_h_r: laser off, high to low rate
    d_l_r: laser off, low to high rate
    hp: half period of modulation
    iset: setpoint current
```

```
    Return:

    An integrand function for ORS in-phase component, representing current times sine function at time t within each chopping cycle'"

    ph_d, pl_d = w2p(t, d_h_r, d_l_r)#laser off

    ph_b, pl_b = w2p(t, b_h_r, b_l_r)#laser on

    n=20

    p_d,p_b=eq_pop(hp,b_h_r,d_h_r,b_l_r,d_l_r,n)

    pp_b = (1-p_b)* pl_b + p_b* ph_b #high-state population with modulation at time t in laser-on half cycle

    pp_d = (1-p_d)* pl_d + p_d* ph_d #high-state population with modulation at time t in laser-off half cycle

    c = d_cur(v)*(pp_b-pp_d)*iset #current at time t

    return c * np.sin(t*np.pi/hp+theta) /hp/np.sqrt(2)


def int_y(t,hp,theta,v, b_h_r,d_h_r,b_l_r,d_l_r,iset):
    '''Input:

    t: time within half cycle

    v: bias

    b_h_r: laser on, high to low rate
```

```
    b_l_r: laser on, low to high rate

    d_h_r: laser off, high to low rate

    d_l_r: laser off, low to high rate

    hp: half period of modulation

    iset: setpoint current

    Return:

    An integrand function for ORS out-of-phase component, representing current times cosine function at time t within each chopping cycle'''

    '''

    ph_d, pl_d = w2p(t, d_h_r, d_l_r)#laser off

    ph_b, pl_b = w2p(t, b_h_r, b_l_r)#laser on

    n=20

    p_d,p_b=eq_pop(hp,b_h_r,d_h_r,b_l_r,d_l_r,n)

    pp_b = (1-p_b)* pl_b + p_b* ph_b #high-state population with modulation at time t in laser-on half cycle

    pp_d = (1-p_d)* pl_d + p_d* ph_d #high-state population with modulation at time t in laser-off half cycle

    c = d_cur(v)*(pp_b-pp_d)*iset #current at time t

    return c * np.cos(t*np.pi/hp+theta) /hp/np.sqrt(2)
```

```
def ors(hp,theta,v,b_h_r,b_l_r,d_h_r, d_l_r,iset):
    '''Compute X and Y ORS measurements in lock-in for bias range v
    Inputs:
    hp: half chopping period
    theta: phase angle in degree
    v: 1-D bias array
    b_h_r: laser on, high to low rate
    b_l_r: laser on, low to high rate
    d_h_r: laser off, high to low rate
    d_l_r: laser off, low to high rate
    iset: setpoint current
    Returns:
    3-row array, first bias, second X component, third Y component'''
    x=[]
    y=[]
    for i in zip(v,b_h_r,d_h_r,b_l_r,d_l_r):
        x.append(integrate.quad(int_x, 0, hp, args=(hp,theta, *i,iset))[0])
        y.append(integrate.quad(int_y, 0, hp, args=(hp,theta, *i,iset))[0])
```

```
    return np.array([v,x,y])


def rot(data, dth):
    '''Input:
    data: 3-row array, first bias, second X component, third Y component
    dth: phase rotation angle in degree
    Returns:
    Phase-rotated ORS data:
    3-row array, first bias, second X component, third Y component
    '''
    dth = dth*np.pi/180
    x = data[1]*np.cos(dth) - data[2]*np.sin(dth)
    y = data[1]*np.sin(dth) + data[2]*np.cos(dth)
    return np.array([data[0], x, y])


def phasetune(data,ylim=[]):
    '''Input:
    data: 3-row array, first bias, second X component, third Y component
```

ylim: a 2-element list specififying the display y axis range for ORS plot

Returns:

An interactive plot with phase parameter adjustable between -1 and +1, corresponding to -180 to +180 deg'"

```
phase = widgets.FloatSlider(min = -1, max = 1, step=0.02, value=0)
def plotORS(phase):
    fig, axs = plt.subplots(3,1, figsize = (5, 12))
    for ors in data:
        ORS=rot(ors,180*phase)
        axs[0].plot(ORS[0],ORS[1],label=i_s)
        axs[1].plot(ORS[0],ORS[2],label=i_s)
        axs[2].plot(ORS[0],np.sqrt(ORS[1]**2+ORS[2]**2))
interact(plotORS,phase=phase)
if ylim:
    axs[0].set_ylim(ylim[0],ylim[1])
    axs[1].set_ylim(ylim[0],ylim[1])
```

G.2 Examples of Function Implementation

G.2.1 Loading Reference Transition Rate at -500 mV/ 1nA

```
#load fitted data

datap=np.loadtxt('patched data/fit data')[250:].T # using the positive bias data only

datan=np.flip(np.copy(datap),1) #use positive measurement for negative bias as well for a bias-symmetric transition rate profile

datan[0]=-datan[0]

data=np.append(datan,datap,axis=1)

v,poph,rhl,rlh=data[0],data[1],data[2]*1000,data[3]*1000 # define the bias array, reference high-state population and transition rate H->L and L->H (convert from kHz to Hz by scaling up 1000 times)

plt.plot(v,rhl,v,rlh)

plt.yscale('log')
```

G.2.2 Computing the Time Evolution of Pyrrolidine High-State Population

```
#compute the time evolution of high-state population for selected biases in the positive bias range

for ind in np.arange(240,500,20):

    print('bias:',v[ind])

    power=1
```

```
    mhl=200

    Ks=3

    hp=1/0.1/2

    d_h_r,d_l_r=rhl[ind],rlh[ind]

    b_h_r,b_l_r=d_h_r+mhl*power,d_l_r+mhl*Ks*power

    n=5

    nd0=d_l_r/(d_l_r+d_h_r)

    data=eq_process(hp,nd0,b_h_r,d_h_r,b_l_r,d_l_r,n)

    plt.plot(data[0],data[1])

    # saving data to file

    np.savetxt('ORS simulation/sim data/process/0.1Hz_bias'+('%.2f' %v[ind])+'mV.txt',data.T)
```

G.2.3 Computing Static ORS for Power Dependence Study

```
#Power-dep static optical rectification study at -500 mV/56 pA

i=0.056

mhl=200

Ks=3

tl=0.672

fig , ax = plt.subplots(4, 1, figsize = (6, 15))
```

```
powerl=np.arange(1,30,2) #define list of powers to study

nh,r_hl,r_lh=rdata(i,rhl,rlh) # compute transition rate data at -500 mV/56 pA based on reference data

i_d=cur_d(v,nh,tl,i) # dark condition I-V curve

for power in powerl:

    poph_b=popb(r_hl,r_lh,power,mhl*i,Ks*mhl*i)

    ax[0].plot(v,poph_b, label=power) # plot bright condition high-state population

    ax[1].plot(v,poph_b-nh,label=power) # plot light induced change in high-state population

    i_b=cur_b(v,poph_b,tl,i) # bright condition I-V curve

    ax[2].plot(v,i_b,label=power)

    di=i_b-i_d # I-V subtraction

    ax[3].plot(v,di,label=power) # plot subtracted I-V (static ORS)

    #save data to file for each power

    np.savetxt("ORS simulation/sim data/Powerdep/N500mV56pA_static/Power"+str(power)+".txt",np.array([v,poph_b,poph_b-nh,di]).T)

#plot formatting

for i in ax:

    i.legend(loc="right",bbox_to_anchor=(1.25, 0.5))
```

```
ax[0].set_ylabel('nH')

ax[1].set_ylabel('dif_nH')

ax[2].set_ylabel('current_bright(pA)')

ax[3].set_ylabel('dif_current(pA)')

ax[3].set_xlabel('Bias (mV)')

ax[3].axvline(x=-362,ls=':',color='r')
```

G.2.4 Computing dynamic ORS for setpoint dependence study

```
print("Setpoint Current-dep 2 -0.5V/xnA, mhl scaled with setpoint current")

iset=[0.056,0.075,0.1,0.133,0.178,0.25,0.316,0.421,0.5,1,2] # current ratios to 1nA

fig, axs = plt.subplots(1,3, figsize = (12, 3))

phase=0

Ks=3

power=2

mhl=200

tl=0.672

data=[]

for i_s in iset:

    poph,rh,rl=rdata(i_s,rhl,rlh)
```

```
    rlh_b,rhl_b=rb(rh,rl,power,mhl*i_s,Ks*mhl*i_s)
    poph_b=rlh_b/(rlh_b+rhl_b)
    ORS=ors(1/273/2,np.pi*phase,v,rhl_b,rlh_b,rh,rl,i_s)
    axs[0].plot(v,ORS[1],label=i_s) # plot in-phase component
    axs[0].set_ylabel("R")
    axs[1].plot(v,ORS[2],label=i_s) #plot out-of-phase component
    i_b=cur_b(v,poph_b,tl,i_s)
    axs[2].plot(v,i_b,label=i_s)
    #save data to file for each setpoint current
    np.savetxt("ORS simulation/sim data/setpoint_2/N500mV"+str(i_s)+'nA.txt',ORS.T)
#Plot formatting
axs[2].set_ylabel("current")
axs[0].set_ylabel("R_X")
axs[1].set_ylabel("R_Y")
axs[2].set_xlabel("Bias (mV)")
```